UNIVERSITY OF SÃO PAULO
SCHOOL OF ENGINEERING

FÁBIO PAIVA DA SILVA

Salinity monitoring and seawater intrusion modeling in Cubatão River, São Paulo

São Paulo
2020

FÁBIO PAIVA DA SILVA

Salinity monitoring and seawater intrusion modeling in Cubatão River, São Paulo

Versão Corrigida

Dissertation submitted to the School Of Engineering at University of São Paulo as partial requirement for the Master of Science Degree.

Subject Area: Hydraulics and Environmental Engineering.

Supervisor: Prof. Dr. José Rodolfo Scarati Martins.

São Paulo

2020

Este exemplar foi revisado e corrigido em relação à versão original, sob responsabilidade única do autor e com a anuência de seu orientador.

São Paulo, _____ de _____ de _____

Assinatura do autor: _____

Assinatura do orientador: _____

Catalogação na publicação

da Silva, Fábio
Salinity monitoring and seawater intrusion modeling in Cubatão River, São Paulo / F. da Silva -- versão corr. -- São Paulo, 2020.
130 p.

Dissertação (Mestrado) - Escola Politécnica da Universidade de São Paulo. Departamento de Engenharia de Hidráulica e Ambiental.

1.Sistema Estuarino 2.Monitoramento Ambiental 3.Modelagem de Qualidade da Água 4.Intrusão Salina 5.Aumento do Nível do Mar I.Universidade de São Paulo. Escola Politécnica. Departamento de Engenharia de Hidráulica e Ambiental II.t.

Name: Fábio Paiva da Silva

Title: Salinity monitoring and seawater intrusion modeling in Cubatão River, São Paulo

Dissertation submitted to the School Of Engineering at University of São Paulo as partial requirement for the Master of Science Degree. Subject Area: Hydraulics and Environmental Engineering.

Approved:

Examining Board

Prof. Dr. _____

Institution: _____

Judgment: _____

Prof. Dr. _____

Institution: _____

Judgment: _____

Prof. Dr. _____

Institution: _____

Judgment: _____

À minha mãe, Sônia, com todo amor e
gratidão que cabem em mim.

AGRADECIMENTOS

A Deus, antes de tudo, pela sua luz divina sempre presente em minha vida.

À Universidade de São Paulo, à Escola Politécnica, à FCTH e à CAPES.

Ao meu orientador, José Rodolfo Scarati Martins, por todos os ensinamentos, dedicação e paciência ao longo do mestrado. Sou muito grato por tudo que me foi proporcionado. É motivo de orgulho ser da sua equipe.

Aos professores Podalyro Amaral de Souza e José Carlos de Melo Bernardino pelas colaborações na banca de qualificação e auxílios ao longo do mestrado. Vocês são duas grandes referências na minha vida profissional e acadêmica.

À minha família, em especial minha mãe, Sônia Maria Paiva da Silva, pelo amor incondicional, esforços desmedidos e incentivo constante. Todos os passos do meu caminho são frutos do que construímos juntos. Aos primos Geysa Naiana da Silva Rufino e Marlon Aurélio Tapajós Araújo por todas as conversas e conselhos.

Aos amigos que fiz ao longo do mestrado, Loan Diep, Lais Ferrer Amorim, Barbara Pozzan dos Santos Duarte, Ariel Ali Bento Magalhães e, em especial, Maria Cristina Santana Pereira e Fábio Ferreira Nogueira, meu xará, pois, sem eles, este percurso teria sido muito mais difícil.

Aos amigos Cirlene Alexandrino, Rafael Carli, William Tomio Shinkai, Gabriela Fragoso, Yorran Furtado, Gabriela Lemos, Mariana Takagi e, especialmente, à amiga-irmã Ananda Fróes por toda fidelidade, carinho e preocupação ao longo desse caminho que estamos percorrendo juntos. A Lis Darioli, por vibrarmos juntos em cada etapa e sermos os melhores companheiros possíveis um para o outro.

E a todos que, direta ou indiretamente, contribuíram para minha formação acadêmica e profissional.

Vou levando comigo
Os rios que vou encontrando.
Os rios que eu encontro
Vão seguindo comigo (NETO, 1953, p. 14).

A chuva esmorecia. A enchente tinha subido da medida. Ficava tudo branco de água. [...] O rio cheio passava depressa puxado pelas águas novas da enchente (JURANDIR, 1941, p. 251).

[...] peguem em mim, e me depositem também numa canoinha de nada, nessa água, que não para, de longas beiras: e, eu, rio abaixo, rio a fora, rio a dentro – o rio (ROSA, 1962, p. 72).

RESUMO

Neste trabalho foram estudados processos de estratificação salina em um rio estuarino e foi aplicado um modelo hidrodinâmico e de qualidade da água para simular e explorar cenários de intrusão salina no rio. O estudo foi desenvolvido no trecho estuarino do Rio Cubatão, São Paulo, Brasil. O estudo foi dividido em três etapas: a montagem, calibração e validação de um sensor de salinidade para uso em ambientes estuarinos; duas campanhas de monitoramento de salinidade no Rio Cubatão; e modelagem de intrusão salina usando o modelo unidimensional HEC-RAS 5.0.5, considerando diferentes cenários de vazão fluvial e aumento do nível médio mar. A primeira campanha de monitoramento foi feita entre 03/11/2016 e 04/03/2017 e a salinidade foi monitorada em um ponto de monitoramento (P1) usando três sensores HOBO U24-002-C Water Conductivity Data Logger em três profundidades diferentes. A segunda campanha foi feita entre 14/05/2019 e 30/05/2019 e a salinidade foi monitorada em dois pontos (P1 e P2) em três profundidades cada usando o sensor proposto. Os resultados mostraram que as vazões de Henry Borden e eventos pluviométricos desempenham um papel importante nos padrões de intrusão salina e de estratificação salina; em eventos de enchente, a intrusão salina é totalmente descolada para jusante do Rio Cubatão e a estratificação muda rapidamente do tipo cunha salina para totalmente misturado. Para a modelagem de intrusão salina do Rio Cubatão, foram simulados cenários com vazão baixa (8m³/s), vazão normal (16m³/s) e vazão alta (40m³/s). Os resultados mostraram que sob vazão baixa, independente da maré, a intrusão salina se desloca para montante e alcança o ponto de captação de água para consumo urbano; para vazão normal, isso ocorre apenas durante as marés de sizígia; e para o cenário de vazão alta, a vazão de água doce empurra a água do mar para o estuário e a intrusão salina não ameaça o abastecimento de água. Considerando os cenários de aumento do nível do mar de ΔH=0.25m, 0.50m e 1.0m combinados com vazões de água doce constantes para o Rio Cubatão (16m³/s – vazão média anual e 8m³/s – vazão de período seco), os resultados do modelo mostraram que a intrusão salina se move significativamente para montante do rio em todos os casos e que o comprimento máximo de intrusão salina pode alcançar 10km no cenário mais desfavorável (ΔH=1.0m e vazão de 8m³/s), 70% maior que o nível do mar atual e a vazão média anual. No ponto de captação de água para abastecimento urbano, a salinidade pode atingir 12g/kg, fazendo com que os tratamentos convencionais fiquem impraticáveis. O aumento do nível do mar pode afetar as instalações de abastecimento de água e requerer soluções de gestão de recursos hídricos como, por exemplo, captação de água em períodos específicos, quando a salinidade estiver baixa; maior reserva de água doce; novos pontos de captação de água, mais distantes que os atuais; ou maior descarga da hidrelétrica de Henry Borden, o que pode provocar conflitos de gestão de água.

Palavras-chave: Sistema estuarino. Rio Cubatão. Estratificação salina. Modelagem de qualidade da água. Modelagem de intrusão salina. Aumento do nível do mar.

ABSTRACT

In this work it was studied the saline stratification processes in an estuarine fluvial stream and it was applied a hydrodynamic and water quality model to simulate and explore seawater intrusion scenarios in the river. The study was carried out at the estuarine reach of Cubatão River, in São Paulo, Brazil. It was divided in three steps: the salinity sensor assembling, calibration and validation procedures for estuarine environments; two salinity monitoring in Cubatão River; and a seawater intrusion modeling using the one-dimensional HEC-RAS 5.0.5 model, considering different river flows and mean sea level rise scenarios. The first field survey was conducted from 03/11/2016 to 04/03/2017 and salinity was monitored at one monitoring point P1) using three HOBO U24-002-C Water Conductivity Data Logger in three different depths. The second field survey was conducted from 14/05/2019 to 30/05/2019 at two monitoring points (P1 and P2) with the proposed salinity sensor at three depths in each point. Results showed that Henry Borden discharges and rainfall events play an important role on seawater intrusion and salinity stratification patterns; under flood events the seawater intrusion is totally flushed out Cubatão River and stratification rapidly changes from salt wedge type to fully mixed type. For Cubatão River seawater modeling, it was simulated scenarios with low river discharge (8m³/s), normal discharge (16m³/s) and high discharge (40m³/s). Results showed that under low flow, independently of the tides, seawater intrusion goes further upstream the river and reaches the water abstraction for urban consumption; for normal discharge, it occurs only during spring tides; and for high discharge scenario, freshwater pushes seawater back to the estuary and seawater intrusion is not a threaten to water supply. Considering sea level rise scenarios of ΔH= 0.25m, 0.50m and 1.0m combined with constant freshwater discharge conditions for Cubatão River (16m³/s – mean annual discharge and 8m³/s – dry season discharge), the model results showed that seawater intrusion moves significantly upstream the river in in all cases and the maximum seawater intrusion length may reach 10km in the worst scenario (ΔH=1.0m and 8m³/s freshwater discharge), 70% higher than the current sea level and the mean discharge. At the local water abstraction location for urban supply, salinity concentration may reach 12g/kg, making conventional water treatment unfeasible. Sea level rise may threaten water supply facilities and require water resources management solutions, such as water abstraction restricted times when salinity concentration is low; higher freshwater reservation; new water abstraction locations, farther the present ones; or higher water discharges in Cubatão River from a local hydroelectric power plant, which can cause water resources management conflicts.

Keywords: Estuarine system. Cubatão River. Salinity stratification Water quality modeling. Seawater intrusion modeling. Sea level rise.

LIST OF FIGURES

Figure 1 – Estuarine system delimitation. 20
Figure 2 – Stratified estuary (Type I). 23
Figure 3 – Partially mixed or partially stratified (Type II). 23
Figure 4 – Well mixed (Type III). 24
Figure 5 – Different shapes of salt intrusion curves. 26
Figure 6 – Greenland surface heating. 28
Figure 7 – Globally averaged sea level change. 28
Figure 8 – Arduino Uno and Arduino Mega. 38
Figure 9 – Pull-up and pull-down resistors schematics. 40
Figure 10 – Standard MOSFET pinout. 41
Figure 11 – 555 IC in its 8-pin DIP configuration. 41
Figure 12 – Spatial dimensions of surface water models. 45
Figure 13 – Model boundary conditions 46
Figure 14 – Control volume for continuity and momentum equations. 53
Figure 15 – Application of the momentum principle 57
Figure 16 – Typical finite difference cell in HEC-RAS 66
Figure 17 – Santos estuarine system. 71
Figure 18 – Rivers Cubatão, Perequê and Mogi; and important points at the upstream reach of Cubatão River. 73
Figure 19 – Astronomical sea level time series from the tidal harmonic constituents. (a) Three months. (b) One week during spring tide. 81
Figure 20 – Map location of primary and secondary data. 82
Figure 21 – Monitoring Point P1. 83
Figure 22 – Monitoring station P2. 84
Figure 23 – Open boundary conditions. 86
Figure 24 – Astronomical tides forcing the downstream boundary during the calibration procedure. 87
Figure 25 – LMC555 IC pins configuration for EC measurements. 91
Figure 26 – Sensor circuit (schematic). 92
Figure 27 – Sensor circuit (breadboard). 93
Figure 28 – Sensor housing and metal electrodes prototype. 95
Figure 29 – Tightness tests at Hydraulics Laboratory (USP). 97
Figure 30 – Sensor calibration curve. 98
Figure 31 – Temperature measurements. 99
Figure 32 – Salinity measurements with (a) sensor temperature and (b) reference temperature. 100
Figure 33 – Coefficient of determination between salinity values. 101
Figure 34 – Rating curve of Cubatão River. 102
Figure 35 – Stage at Cubatão River (P1) and COSIPA (First field survey). 103
Figure 36 – Linear regression of Cubatão River and COSIPA stages. 103

Figure 37 – Stage at Cubatão River (P1) and COSIPA (Second field survey). 104
Figure 38 – Precipitation, stage, HB and river discharge and salinity stratification during the first field survey at P1..... 105
Figure 39 – Maintenance of salinity sensors at P1. 108
Figure 40 – Maintenance of salinity sensors at P2. 108
Figure 41 – Precipitation, stage, river discharge and salinity stratification during the second field survey at P1..... 109
Figure 42 – Temperature and salinity at P1. 111
Figure 43 – Temperature and salinity at P2. 112
Figure 44 – Hydrodynamic calibration at P1. 114
Figure 45 – Water quality calibration at P1 and P2. 114
Figure 46 – Salinity spatial variation (calibration). 115
Figure 47 – Hydrodynamic validation at P1. 115
Figure 48 – Water quality validation at P1. 116
Figure 49 – Salinity spatial variation (validation). 116
Figure 50 – Salinity response to high river discharge. 118
Figure 51 – Salinity distribution in Cubatão River during spring tide (ST) and neap tide (NT) for different river discharge scenarios. 119
Figure 52 – Maximum seawater intrusion during (a) spring and (b) neap tides (Q=16m³/s). 120
Figure 53 – Maximum seawater intrusion during (a) spring and (b) neap tides (Q=40m³/s). 121
Figure 54 – Maximum seawater intrusion during (a) spring and (b) neap tides (Q=8m³/s). 122
Figure 55 – Maximum seawater intrusion profile for each SLR scenario (16m³/s). 123
Figure 56 – Maximum seawater intrusion profile for each SLR scenario (8m³/s). 125
Figure 57 – Variation of the seawater intrusion length versus fresh water discharge under SLR scenarios (ΔH=0.00m, 0.25m, 0.50m and 1.00m). 125
Figure 58 – Minimum freshwater discharge to maintain S>0.5g/kg at the water abstraction location. 126

LIST OF TABLES

Table 1 – Estimated global mean SLR for different periods. 29
Table 2 – Salinity Range of different water sources. 31
Table 3 – EC values for typical samples. 33
Table 4 – Coefficients for Eqs. 4-7 to calculate salinity through PSS 1978. 35
Table 5 – Arduino boards and its technical specification. 37
Table 6 – Typical industrial batteries specification. 39
Table 7 – 555 IC pins functions. 42
Table 8 – Electronic components used in the proposed salinity sensor. 77
Table 9 – Acquired data during field surveys. 82
Table 10 – Boundary forcing and initial conditions. 88
Table 11 – Individual and total components costs. 96
Table 12 – Frequency readings for each corresponding EC at 23°C. 98
Table 13 – Skill values (calibration and validation). 117
Table 14 – Maximum seawater intrusion length for each simulated scenario. 122

SUMMARY

1 INTRODUCTION 14
1.1 OBJECTIVES 16
1.2 TEXT STRUCTURE 17
2 LITERATURE REVIEW 18
2.1 ESTUARIES AND ESTUARINE RIVERS 18
2.2 CLIMATE CHANGES, SEA LEVEL RISE AND ESTUARIES 26
2.3 SALINITY AND ELECTRICAL CONDUCTIVITY MEASUREMENTS 30
2.4 MICROELECTRONICS AND WATER QUALITY MONITORING 36
2.5 HYDRODYNAMICS AND WATER QUALITY MODELING 43
2.6 HEC-RAS MODEL 52
2.6.1 Unsteady Flow Simulation 53
2.6.2 Water Quality Simulation 67
3 STUDY AREA 71
4 MATERIALS AND METHODS 75
4.1 SALINITY SENSOR ASSEMBLING, CALIBRATION AND VALIDATION 75
4.1.1 Sensor design, housing and power supply 75
4.1.2 Calibration and Validation methods 77
4.2 ENVIRONMENTAL MONITORING: PRIMARY AND SECONDARY DATA 80
4.2.1 First Field Survey (03/11/2016-04/03/2017) 83
4.2.2 Second Field Survey (14/05/2019-30/05/2019) 84
4.3 MODEL SETUP AND SIMULATED SCENARIOS 85
4.3.1 Boundary forcing conditions 86
4.3.2 Model calibration and validation procedures 87
4.3.3 Simulated Scenarios 89
5 RESULTS AND DISCUSSION 91
5.1 SALINITY SENSOR DESIGN, PROTOTYPE AND TEST 91
5.1.1 Sensor experiments 96
5.2 FIELD SURVEYS 102
5.2.1 First Field Survey 104
5.2.2 Second Field Survey 108
5.3 SEAWATER INTRUSION MODELING 113

5.3.1 Calibration and validation model performance 113
5.3.2 Seawater intrusion response to seasonal river discharge variation . 118
5.3.3 Seawater intrusion response to sea level rise 122
6 CONCLUSIONS 128
REFERENCES 131
APPENDIX A 139

1 INTRODUCTION

Estuarine areas are of major importance for human development and can provide innumerable benefits such as water for agriculture, power supply, industrial plants and urban consumption. These water bodies have some general features, such as the presence of port facilities and essential fishery resources, and they are also the destination of industrial and urban wastewater. Additionally, estuaries are among the most biologically productive systems due to the presence of high nutrient concentrations, which intensify the biological productivity (JEONG et al., 2010; BHUIYAN; DUTTA, 2012; ALFREDINI; ARASAKI, 2013; JI, 2017).

A direct consequence of its significance is the high population concentration in many estuaries; almost 60% of the biggest cities around the world are located along estuarine areas or estuarine river reaches. All those multiple uses of estuarine waters present natural conflicts for its management and that is why a wide knowledge of its water quality dynamics is critical to the water resources decision making processes (MIRANDA; CASTRO; KJERFVE, 2012).

Estuaries are very sensitive and vulnerable to human activities, but the impacts were not considered significant until the half of the nineteenth century. After this, there was an extensive growth of industrial and agricultural activities, fishery and port facilities and dam constructions for hydroelectric purposes, which provoked an increasing concern on estuarine conservation and sustainable development (JEONG et al., 2010; ALFREDINI; ARASAKI, 2013).

One of the most important physical processes in estuarine areas is the seawater intrusion, which can be described as the seawater incursion into the estuary as an effect of the tides. Seawater intrusion in estuaries is a complex phenomenon and depends directly on many environmental conditions, such as the estuary geometry, tidal processes and fresh water inputs. This process may cause high salinity concentration in upstream parts of estuarine rivers, affecting multiple uses of water (MARTIN; MCCUTCHEON, 1999; ETEMAD-SHAHIDI et al., 2015; HADDOUT; IGOUZAL; MASLOUHI, 2016; JI, 2017). Considering that each estuary has specific salinity patterns, it is crucial to develop a better understanding on its local behavior, principally in estuaries with high density population or industrial areas,

where water resources demand is decisive for several activities (MIRANDA; CASTRO; KJERFVE, 2012; ETEMAD-SHAHIDI et al., 2015).

Cubatão, São Paulo, is an emblematic and historical example of an industrial city in Brazil, which has a vast experience with environmental issues. It is located in Santos estuarine system and the Cubatão River crosses the urban area being, at the same time, an indispensable source of water for human and industrial supply. So, water quality is an important aspect of its management and seawater intrusion process is a crucial phenomenon to investigate in order to improve local water management (PINTO, 2005; COUTO, 2012; FCTH, 2017).

The environmental monitoring followed by numerical modeling forms an essential tool not only for understanding the hydrodynamic and water quality processes, but also for developing plans for water resources and environmental management. Numerical models are one of the most important tools that enabled the evolution of the hydrodynamics and water quality comprehension in the past decades. Considering that numerical models are capable to produce fast answers for different scenarios in large study areas, they became essential tools not only for understanding the hydrodynamic and water quality processes but also for developing plans for water resources and environmental management (JAMES, 1993; CHAPRA, 1997; MARTIN; MCCUTCHEON, 1999; JI, 2017).

In this context, this research proposes the salinity monitoring and the application of numerical modeling techniques to investigate seawater intrusion behavior under different fresh water discharge and sea level rise scenarios in Cubatão River.

1.1 OBJECTIVES

The aim of this study is to investigate the salinity stratification processes in an estuarine fluvial stream and apply a numerical model to explore scenarios of seawater intrusion in an estuarine river reach under different scenarios of fluvial and tide regimes. This study uses two complementary approaches to study the seawater intrusion behavior in Cubatão River, combining field measurements with numerical modeling. These goals comprehend the analysis of observed salinity profiles and forcing conditions acting along a estuarine river reach and then set up a one-dimensional numerical model to simulate and predict the behavior of the salinity intrusion along the river. Considering the importance of the high resolution data input necessary to support the above main goal, a contribution to the estuarine salinity monitoring was also included in terms of the development of a low-cost salinity sensor.

The specific objectives of this research are:

a) Design, build and test a low-cost and fully submerged salinity sensor based on a popular microcontroller platform to enable high temporal and spatial resolutions monitoring of salinity and water temperature behavior in estuarine environments;
b) Conduct field surveys to examine the salinity stratification in a estuarine river reach and correlate its behavior with local hydroelectric power plant water discharge and environmental forcing conditions;
c) Setup and calibrate a one-dimensional hydrodynamic and water quality numerical model to investigate the spatial and temporal seawater intrusion patterns in an estuarine river reach. The forcing conditions considered in the simulated scenarios are the tidal activity, river flow and local hydroelectric power plant water discharge;
d) Evaluate the sea level rise impacts caused by human-induced climate change on seawater intrusion pattern in an estuarine river reach by applying a one-dimensional numerical model.

The study was carried out over the estuarine reach of Cubatão River, in São Paulo, Brazil

1.2 TEXT STRUCTURE

This dissertation is structured as follows:

a) Chapter 2 presents the literature review of the most important subjects for the dissertation topic. It describes the principal concepts of estuarine systems; the impacts of climate changes and sea level rising in those environments; the physical concept of salinity and how it is measured; the fundamentals of microelectronics for salinity measurement; and the governing equations of the hydrodynamics and water quality mathematical models, especially the USACE's HEC-RAS model suite.
b) Chapter 3 describes the study area, considering principally the characterization of the main river in the region, but also identifying its urban and industrial activities, the watersheds that contributes to the main rivers discharge and the most important facilities that impacts the rivers and salinity dynamics.
c) Chapter 4 presents the methodological approach used, namely the materials and procedure for the salinity sensor assembling, calibration and validation tests; the monitoring sites and methods for each field survey; the mathematical model description, its boundary and initial conditions and further modeled scenarios.
d) Chapter 5 presents and discusses the results obtained in the different fronts like the sensor assembling, laboratory calibration and fieldwork validation; the salinity stratification patterns in the monitoring sites, considering the influence of precipitation, hydroelectric power plant discharges and tides; and the modeling of salinity intrusion behavior under different environmental conditions.
e) The last Chapter presents the conclusions and recommendations for further investigations and research.

2 LITERATURE REVIEW

2.1 ESTUARIES AND ESTUARINE RIVERS

Estuarine systems are transitional ecosystems between riverine and coastal environments and, even being only a small part of the water systems (about 5%), they are among the most productive ecosystems on Earth, with low primary production but with very high secondary production providing innumerous ecological services and benefits for human development. These systems are extremely recent in geological terms, with less than 5000 years old, and are a result of sea establishment in its current level following the last ice age (RICH; MAIER, 2015; VARGAS; VAZ; DIAS, 2017; WANG et al., 2019; WOLANSKI et al., 2019).

The interaction between freshwater and seawater creates a unique environment, with characteristics that enabled human civilization to settle and develop, such as a very productive environment, adequate for agricultural and fishery purposes; the presence of natural waterways with access to both the ocean and the continental lands; a relatively flat topography, suitable for port facilities; and, evidently, water for urban and industrial supply. In general, the major groups of development activities in estuarine systems are:

a) Fishery resources: aquaculture and protection of spawning habitats;
b) Transportation: navigation channels and ports and harbor facilities;
c) Agriculture: withdrawal of irrigation water;
d) Urban development: urban water supply, leisure, aesthetics;
e) Industries: industrial water supply, wastewater disposal, hydropower development.

However, all those activities may impact the estuarine system dynamics, changing its configuration, reducing the amount of freshwater inputs and increasing pollutants concentration. These ecosystems have been presenting significant alteration due to recent human environmental degradation, especially caused by industrialization, urban development and agricultural expansion (UNESCO, 1991; PRANDLE, 2009; JI, 2017; WOLANSKI et al., 2019).

In order to understand the estuarine dynamics, it is fundamental to know the definitions and classification of estuaries. Since salinity is one of the most important and representative physical constituent in estuarine environments, classifications are commonly related to its concentration behavior (MIRANDA; CASTRO; KJERFVE, 2012; JI, 2017).

The simplest and classic definition of estuary is a transitional semi-closed coastal environment which has a free connection with the open sea, where seawater is measurably diluted with freshwater from rivers (CAMERON; PRITCHARD, 1963). It was added to the original concept the upper reach of the estuary, which is the limit of the tidal influence in the estuarine rivers. It was also added the three explicit estuarine zones (DIONNE, 1963):

a) Inferior or marine zone, with a free connection with the open sea;
b) Medium zone, with strong mixing of the seawater and the fresh water discharge;
c) Upper or fluvial zone, with fresh water influenced by tidal oscillation.

Those definitions are widely accepted, but do not describe accurately the estuary zones limits and its interfaces, being necessary to look at a wider definition. Considering that this environment can present different heads and complex compositions, the estuarine rivers can have properties distribution similar to the estuary itself, working as estuarine subsystem. As a result of this complexity and as an improvement of the classical definition, this environment can also be called by estuarine system. An estuarine system can be divided into four main parts (MIRANDA; CASTRO; KJERFVE, 2012):

a) Fluvial zone (FZ);
b) Tidal river or fluvial-tidal transition zone (TRZ);
c) Tidal or mixing zone (MZ);
d) Coastal zone (CZ).

The fluvial zone (FZ) presents a unidirectional flow, there is no tidal influence and the salinity concentration is negligible (below 0.1g/kg). The tidal river zone (TRZ)

is affected by the tidal influence, in which the flow direction depends on the interaction between the river discharge and the tidal activity. In this zone, the salinity concentration can vary from 0.1g/kg to 1.0g/kg and the length can reach hundreds of kilometers. The limit of the tidal influence is called estuary head. The tidal or mixing zone (MZ) refers to the classical definition of estuary and it extends from the limit of the fluvial-tidal zone, in which salinity is 1.0g/kg, until the estuary mouth, which can also reach hundreds of kilometers. So, the salinity of estuarine system can vary from small values of 0.1g/kg to 35.0g/kg, the average seawater salinity. It is important to notice that those limits are not static; they may change depending on the wind, river discharge and tidal activity (MIRANDA; CASTRO; KJERFVE, 2012; ALFREDINI; ARASAKI, 2013). Figure 1 illustrates the estuarine system delimitation.

Figure 1 – Estuarine system delimitation.

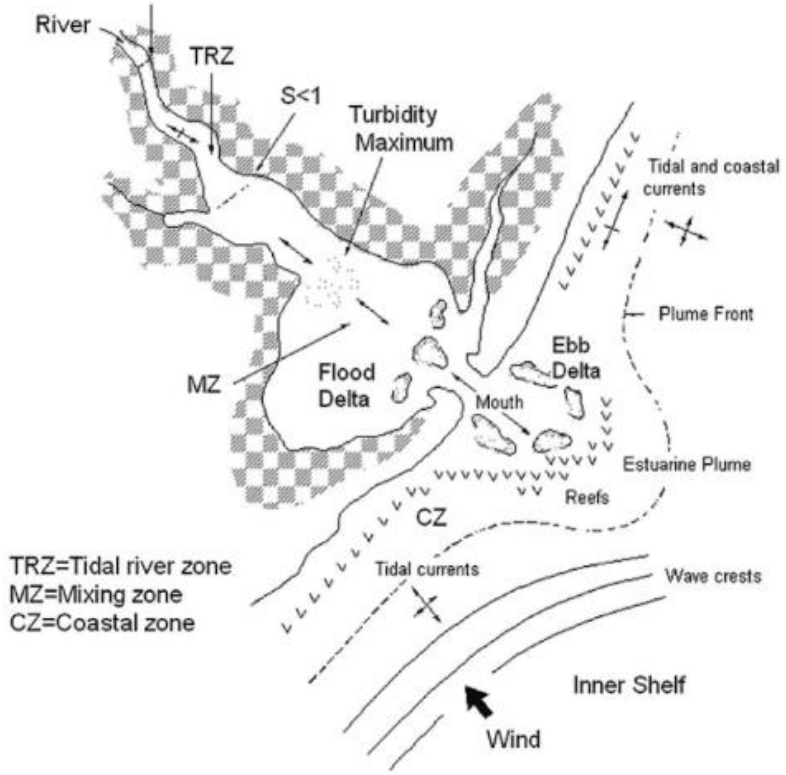

Source: Miranda; Castro; Kjerfve (2012).

The river is located at the upper boundary, where the tidal activity is negligible. Next is the tidal river, where the tides begin to affect transport, but the presence of salt is low, in that case the water is almost fresh. This is followed by the estuary itself, which is marked by full tidal reversals and brackish water (a mixture of salt and fresh

water). Finally, the estuarine system ends at the ocean (CHAPRA, 1997; JEONG et al., 2010).

The salinity distribution of each estuarine system is a result of a complex interaction between different forcing mechanisms on its geomorphologic boundaries, e.g. the freshwater discharge, the tidal currents, the pressure gradient, advection and dispersion processes. It is extremely important for the estuarine dynamics and, consequently, for its mixture processes (NELSON, 2008; PRANDLE, 2009; YOON; WOO, 2015).

As a result of the interaction between the forcing conditions, there are two main physical processes related to the movement of salt in estuarine systems: seawater intrusion and saline stratification. Saline water tends to propagate into the estuarine system reaching its fluvial zone (seawater intrusion) and the seawater may present different mixing degrees with the above freshwater (saline stratification). Under extreme conditions, for example, the reach affected by the seawater intrusion may extend over more than 300 km (UNESCO, 1991; PRANDLE, 2009; MIRANDA; CASTRO; KJERFVE, 2012; SAVENIJE, 2012; JI, 2017; VARGAS; VAZ; DIAS, 2017).

The seawater incursion into the estuarine system is a result of different forcing conditions (governing factors) that creates a specific mixing mechanism for each estuarine system. They can significantly vary with time:

a) Seawater inputs;
b) Freshwater inputs;
c) Tidal activity;
d) Estuarine configuration (which is strongly related to the sediment movement);
e) Meteorological factors (wind, precipitation, evaporation);
f) Developed works.

Seawater intrusion processes are extremely important because they may impact and limit some water uses such as agricultural, urban and industrial uses, as it reduces the water quality in the estuary, leading to unfeasible water treatment requirements. So the salinity intrusion pattern in the estuarine system is of major importance for water management. During dry periods, for example, when the necessity of freshwater is higher, seawater intrusion can impact water quality due to

higher salinity concentration, which can reduce freshwater availability; heavy precipitation may increase significantly the upstream discharge and pushes the seawater back to the ocean, but reducing freshwater inputs would increase the seawater intrusion; seawater intrusion patterns can also be affected by human activities, such as hydroelectric power plants discharges, excessive water abstraction and damming on rivers (PINHO; VIEIRA, 2007; BHUIYAN; DUTTA, 2012; LIU; LIU, 2014; YANG et al., 2015; CHEN et al., 2016; VARGAS; VAZ; DIAS, 2017; WANG et al., 2019).

Hence, seawater intrusion length moves upstream and downstream the estuarine river during a tidal cycle as a result of the local governing factors. The maximum length of penetration of seawater intrusion in the estuarine river (L_S) increases rapidly with the decreasing river discharge. It varies from few kilometers, like 5km, up to 300km, depending of the governing factors (UNESCO, 1991; SAVENIJE, 2012; YANG et al., 2015; LIU et al., 2019).

Saline stratification is a vertical density gradient caused by different salinity concentrations in the water column, since salt diluted in seawater makes it heavier than freshwater. Generally, seawater flows in the upstream direction, at the bottom of the river, while less dense freshwater tends to flow in the downstream direction above the seawater. This difference of density has a significant effect on estuarine flow and creates a salinity gradient in the water column. The duration and thickness of this vertical stratification depend on mixing inputs as rainfall, freshwater discharge, tides and winds (TALLEY et al., 2011; JI, 2017; MIRANDA et al., 2017; VARGAS; VAZ; DIAS, 2017; WANG et al., 2019).

There are generally three different types of stratification patterns in estuarine systems and it is mainly related to the interaction between the freshwater discharge and the tidal flow (MIRANDA; CASTRO; KJERFVE, 2012; SAVENIJE, 2012; ALFREDINI; ARASAKI, 2013).

a) Stratified or salt wedge type (Type I);
b) Partially mixed or partially stratified type (Type II);
c) Well mixed type (Type III).

The stratified or salt wedge type (Type I) commonly occurs when the fresh water is large compared to tidal flow (low tidal energy), which means a high river discharges and low tides, causing a distinct layer between the freshwater and the seawater. There is a marked vertical stratification, with two distinct layers. In the upper layer, the salinity concentration is considerably low and it is fundamentally an effect of the vertical mixing (entrainment) from the high salinity layer (Figure 2) (HARALAMBIDOU; SYLAIOS; TSIHRINTZIS, 2010; PERALES-VALDIVIA; SANAY-GONZÁLEZ; VALLE-LEVINSON, 2018).

Figure 2 – Stratified estuary (Type I).

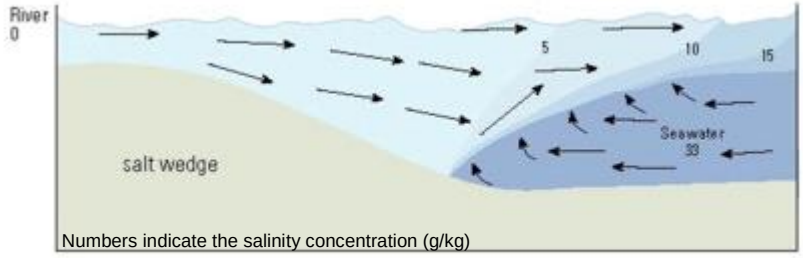

Source: Adapted from Cochran (2014).

In partially mixed or partially stratified type (Type II), the saline stratification is moderate and the vertical mixing is softer than the type I. There is a more intense mass interchange between the layers and the difference between the surface and bottom salinity concentration is of few units (Figure 3).

Figure 3 – Partially mixed or partially stratified (Type II).

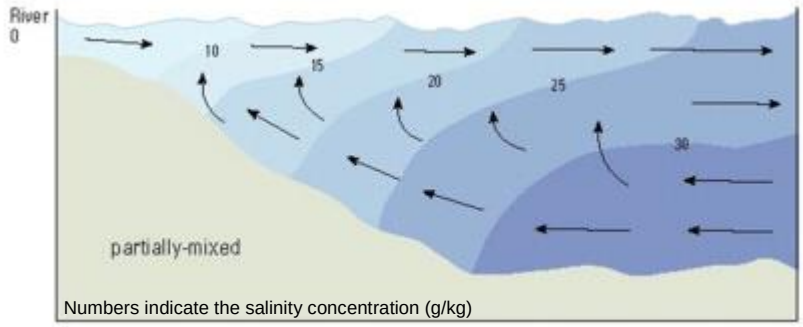

Source: Adapted from Cochran (2014).

In well mixed type (Type III), the freshwater discharge is small compared to the tidal flow (high tidal energy), which generally occurs in low river discharges and large

tides. In this type, there is practically no difference between the surface and bottom salinity concentration, which means that the estuary is vertically mixed (Figure 4).

Figure 4 – Well mixed (Type III).

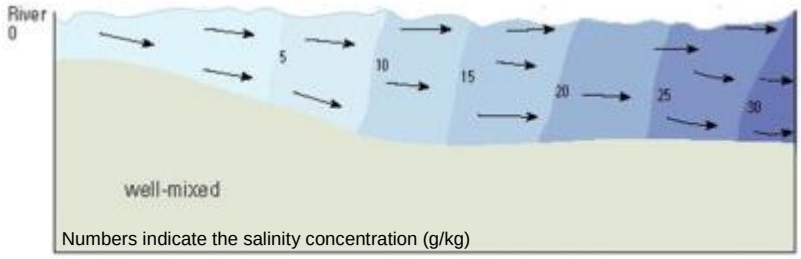

Source: Adapted from Cochran (2014).

The type of vertical mixing and salinity stratification of water can be determined by calculating the stratification parameter n_S, defined as:

$$n_S = \frac{S_{bott} - S_{surf}}{0.5\ (S_{bott} + S_{surf})} \quad (1)$$

In which

n_S: stratification parameter;

S_{bott}: salinity at the bottom (g/kg);

S_{surf}: salinity at the surface (g/kg).

If $n_S < 0.1$, the water column is fully mixed. For $0.1 < n_S < 1.0$, water column is considered partially mixed, and when $n_S > 1.0$ water column is very stratified, with the presence of salt wedge (UNESCO, 1991; HARALAMBIDOU; SYLAIOS; TSIHRINTZIS, 2010).

It is important to notice that the estuarine classification based on salinity stratification is not fixed; in other words, it varies along the estuary and over time. In the upper part of the estuary, where the freshwater discharge is usually dominant, the entrainment is the most relevant process to transport the salt from the lower layer to the upper layer. Downstream the estuary, closer to the ocean, the tidal amplitude is higher and the prevalent mixing process is the turbulent diffusion, which can cause a partially mixed estuary condition. Considering a temporal scale, the seasonal freshwater discharge and the tidal amplitude variation can provoke a different type

classification for a given part of the estuary (PINHO; VIEIRA, 2007; PRANDLE, 2009; ALFREDINI; ARASAKI, 2013; JI, 2017).

In well mixed estuaries, it is possible to classify the estuary according to its saline profile along the estuary. In Positive Estuaries, the salinity decreases gradually in the upstream direction, because the river discharge pushes seawater back to the ocean and dilutes it along the estuarine system. On the other hand, in Negative or Hypersaline Estuaries, the salinity increases in the upstream direction. It occurs in shallow estuaries in which evaporation exceeds precipitation and the freshwater discharge is not sufficient to compensate the difference. Thus, the salt intrusion curves can be (SAVENIJE, 2012):

a) Recession Shape (Type I). It occurs in riverine estuaries, with narrow geometry and high river discharge;
b) Bell Shape (Type II). It occurs in estuaries with a trumpet shape; long conveyance length in the upstream part and short conveyance length in the downstream part;
c) Dome shape (Type III). It occurs in estuaries with a tunnel shape; short conveyance length in the upstream part and long conveyance length in the downstream part;
d) Humpback shape (Type IV). It occurs in Negative or Hypersaline Estuaries, which have large water bodies compared to the amount of freshwater input.

The shapes are strongly determined by the combination of the forcing factors in the estuary. Figure 5 illustrates the different shapes

Figure 5 – Different shapes of salt intrusion curves.

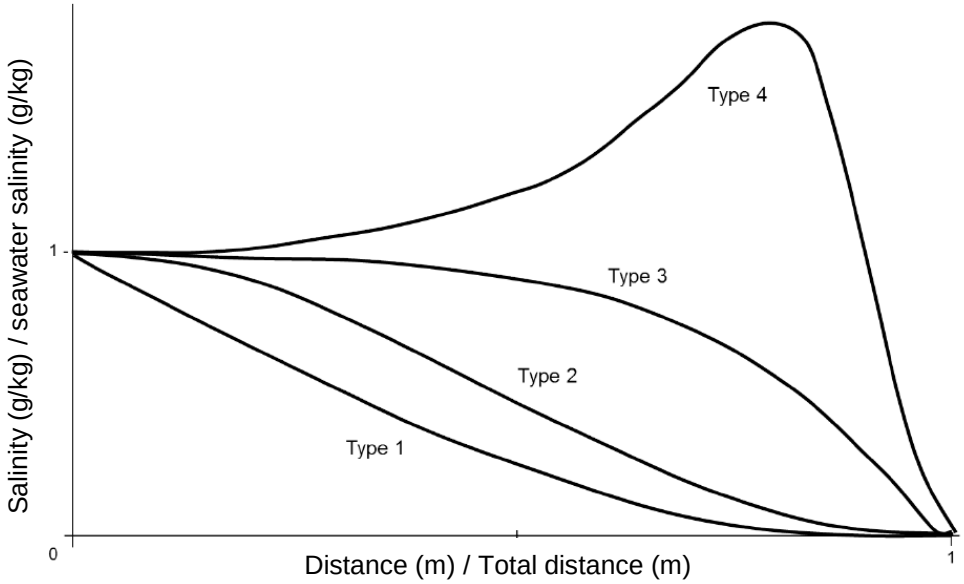

Source: Adapted from Savenije (2012).

This classification is also not fixed. The salt intrusion curves are based on steady-state conditions, which do not represent the temporal scale variation. During precipitation events or tidal variation, the hydrodynamic can change salt intrusion curve. Seawater intrusion is also affected by alterations on governing factors, mainly the river discharge regime and the seawater flow from the sea (PINHO; VIEIRA, 2007; MIRANDA; CASTRO; KJERFVE, 2012; SAVENIJE, 2012; VARGAS; VAZ; DIAS, 2017).

2.2 CLIMATE CHANGES, SEA LEVEL RISE AND ESTUARIES

Climate changes have been one of the main issues discussed by the scientific community and the media in recent decades, and have been related to major changes in environmental conditions around the globe. Studies about climate changes have been done since the beginning of the nineteenth century, but it was only in 1960 decade, with the identification of the greenhouse gases accumulation in the atmosphere, that there was an intensification of studies in this area (TITUS et al., 2004; NICHOLLS et al., 2008; ROBINS et al., 2016; WOLANSKI et al., 2019).

It is extremely likely that human activities are the main cause of current climate change in the world, especially since the second half of the 20th century, with the growth of industrial production and the burning of fossil fuels such as coal and oil.

Consequently, there is an increase of greenhouse gases concentration in the atmosphere, such as carbon dioxide (CO_2), methane (CH_4) and nitrous oxide (N_2O). Although there is a minor trend of thought contrary to the idea that climate change have been intensified by human activities, it is undeniable that there is an accumulation of those gases in the atmosphere and that there is strong evidence that the current climate changes are unprecedented in spatial distribution when compared to evidences from the last 2000 years (SIMAS; NUNES; FERREIRA, 2001; NICHOLLS et al., 2008; ESTEVES, 2014; IPCC, 2014; NEUKOM et al., 2019).

Some of the main effects of climate change are: the oceans and atmosphere heating; the reduction of snow and ice volumes; sea level rise (SLR); and more frequent and intense extreme weather events. Each of the last three decades has successively been the hottest on the Earth's surface since 1850. Independent surveys have shown a long-term trend in increasing the temperature in both the atmosphere and the oceans. Ocean heating accounts for more than 90 percent of the energy accumulated in the global climate system between 1971 and 2010, occurring mostly near the surface at about 0.11°C per decade at depths of 0-70m (IPCC, 2014; ROBINS et al., 2016; WOLANSKI et al., 2019).

The mean SLR is a notable observed consequence of the climate changes. The mean sea level remained nearly constant in the last 3000 years, but since the 20th century it has been rising as a direct cause of global climate change. This increase is caused basically by two factors: the melting of the glaciers and the thermal expansion of the oceans. Globally, thermal expansion is the principal factor of SLR within the range 2.6 ± 0.4mm/year. Glaciers melting is the second factor on SLR, with a contribution of 0.66mm/year, approximately (TITUS et al., 2004; IPCC, 2014; YANG et al., 2015; CHEN et al., 2016; KUANG et al., 2017; PALMER; WATSON; FISCHER, 2019).

At the beginning of the 21st century, between 2002 and 2011, it was observed an even faster melting of the glaciers in Greenland and Antarctica and the amount of ice in the Arctic has been decreasing decade after decade since 1979, with decreasing rates between 3.5% and 4.1% per decade. Figure 6 compares the surface temperature of Greenland from April 2016 to the average of 2001-2010 for the same month. In certain areas, the temperature variation reached 20ºC (BHUIYAN; DUTTA, 2012; CHUA; XU, 2014; IPCC, 2014; CHEN et al., 2016).

Figure 6 – Greenland surface heating.

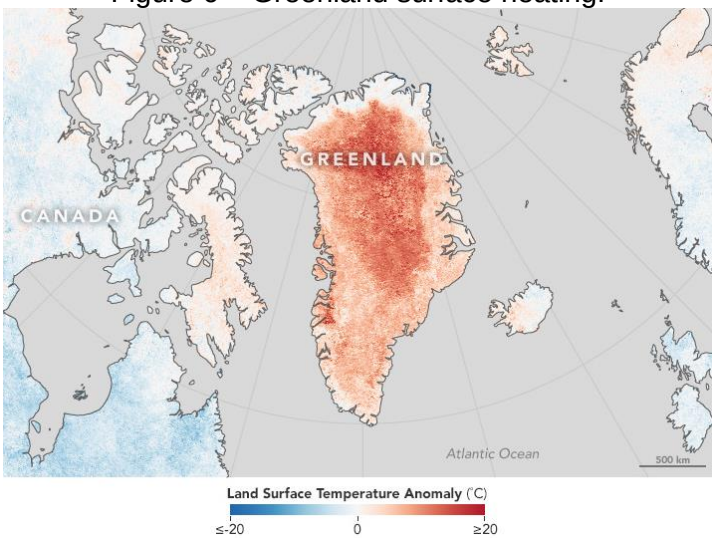

Source: NASA (2017).

The thermal expansion of the oceans refers to the increase in the volume (decrease in density) of the water caused by the increase in temperature, mainly at the surface, contributing to SLR. Changes in ocean temperatures can affect marine ecosystems, species migration and breeding patterns, threatening corals, causing harmful proliferation of algae, and even declining populations of fish species (TALLEY et al., 2011; RICH; MAIER, 2015; WOLANSKI et al., 2019).

It was identified an increase of 0.19m between the years 1901 and 2010, with the increasing rate from the mid-nineteenth century onwards being higher than the observed rate in the last two thousand years. Forecasts predict that average sea levels will continue to rise throughout the 21st century and that by the end of the century, approximately 70% of coastal regions will be affected by sea level change (IPCC, 2014). Figure 7 shows the overall mean SLR from 1901 to 2010 and each color represents a different source of research.

Figure 7 – Globally averaged sea level change.

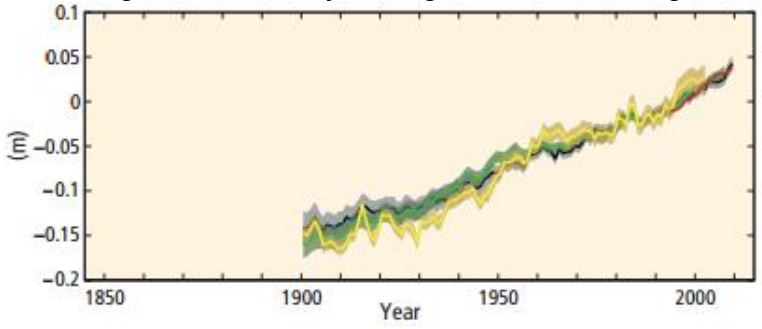

Source: IPCC (2014).

SLR and extreme weather events are the major consequences of climate changes in coastal environments, which strongly impact the coastal shape and its dynamics. Estuarine systems are particularly sensitive to SLR and are among the most exposed environments to the climate changes consequences, as it affects not only the sea level but also the hydrological cycles and the river flows. Seawater intrusion resulting from SLR is of great concern for estuarine environments as a consequence of climate change. As the combination of tidal activity and freshwater inputs are the predominant forcing conditions for seawater intrusion patterns, a major effect of SLR in estuarine system is the increase in salinity concentration due to higher seawater intrusion length, which can affect upstream freshwater that was not previously affected or increase salinity to intolerable values for industrial or urban purposes (PRANDLE, 2009; CHUA; XU, 2014; LIU; LIU, 2014; YANG et al., 2015; KUANG et al., 2017; PALMER; WATSON; FISCHER, 2019; WANG et al., 2019).

The global mean rate of SLR from 1993 to 2010 is estimated between 2.8 - 3.6 mm/year, which is higher than the previous estimation of 1.5 - 2.0mm/year from 1971 to 2010. It indicates that the rate of SLR is increasing with time and predictions must attempt to this behavior (IPCC, 2014; CHEN et al., 2016; KUANG et al., 2017; PALMER; WATSON; FISCHER, 2019). Table 1 indicates the estimated mean SLR in different periods.

Table 1 – Estimated global mean SLR for different periods.

Period	SLR estimation (mm/year)
1901-2010	1.5 - 1.9
1971-2010	1.5 - 2.0
1993-2010	2.8 - 3.6

Source: Adapted from IPCC (2014); Alfredini; Arasaki (2019).

As sea level rise is not geographically uniform, regional or local historical data are necessary to determine sea level trends. In São Paulo state coast, more specifically in Santos, SLR presents different patterns over time. From 1944 to 1989 the SLR in Santos was estimated at 0.1132cm/year, but considering the period from 1940 to 2014, the SLR pattern was about 0.33cm/year, which follows the global trend of aggravation of SLR scenarios in the next decades. So, by 2100, the mean SLR rise from 1940 to 2100 will be 1.1m, but during the next decades this estimative can

be higher. Considering the current sea level, a recommended SLR scenario considers by the yeah 2100 the range of 0.5 - 1.0m, but this scenario may be 50% higher and it is also necessary to consider that the sea level will keep rising after 2100 (HARARI; CAMARGO, 1995; ALFREDINI; ARASAKI, 2019).

2.3 SALINITY AND ELECTRICAL CONDUCTIVITY MEASUREMENTS

Salinity is one of the most important physical constituents in estuarine environments, so a better comprehension of its concepts, seawater composition and measurement procedures are fundamental. A salt can be defined as a neutral ionic compound composed of positive ions (cations) and negative ions (anions) and salinity is the total concentration of soluble salts dissolved in water. More precisely, salinity is defined as the mass in grams of dissolved inorganic matter in 1.0kg of seawater (TALLEY et al., 2011; RICH; MAIER, 2015).

Seawater is a complex solution which contains nearly all known elements. However, the principal components, as percentage of total mass of dissolved material are: chlorine ion (55.0%), sulfate ion (7.7%), sodium ion (30.7%), magnesium ion (3.6%), calcium ion (1.2%), and potassium ion (1.1%). This amount of dissolved inorganic matter in water is called salinity, which was originally defined as the mass in grams of solid material in a kilogram of seawater (g/kg) after evaporating the water away (Absolute salinity). The average salinity in ocean is about 35.0g/kg, also written as $S = 35.0‰$ or $S = 35\mathrm{ppt}$ (parts per thousand) (PRANDLE, 2009; IOC; SCOR; IAPSO, 2010; TALLEY et al., 2011).

In 1980, there was a significant improvement in salinity measurements with the adoption of an indirect and accurate measurement based on the water electrical conductivity (EC) and temperature. The Practical Salinity Scale 1978 (PSS-78) is an algorithm part of the International Equation of State of Seawater – 1980, which was used in oceanography and other research areas from 1980 to 2009. Assuming that the relative chemical composition of seawater is constant, a solution containing a specified concentration of dissolved matter will have a given EC, which will vary with temperature. In this case, salinity is measured indirectly, as a ratio of the EC of the water to a potassium chloride standard. This definition is a ratio – so dimensionless – defined as Practical Salinity - S_P and written as $S = 35.0$ or $S = 35.0psu$ (practical

salinity unity) (LEWIS; PERKIN, 1981; PAWLOWICZ, 2008; MCDOUGALL; FEISTEL; PAWLOWICZ, 2013; LI; LIU, 2019).

The current definition of salinity is an improvement of the last one, with updated thermodynamic properties of seawater, as part of The International Thermodynamic Equation of Seawater – 2010 (TEOS-10). It is a return to the original definition (Absolute Salinity - S_A), that is, the ratio of mass of all dissolved substances in seawater to the mass of the seawater, expressed in g/kg or kg/kg, i.e. a true mass fraction. S_A is preferred over S_P because the thermodynamic properties of seawater are directly influenced by the mass of dissolved constituents and S_P depends only on EC, which means that S_A is affected by non-ionic components, while S_P (EC based) is affected only by ionic components. However, the correction factor to convert S_P to S_A is small and negligible for engineering purposes on coastal regions. It is only required to be aware of the current units (PAWLOWICZ, 2008; IOC; SCOR; IAPSO, 2010; TALLEY et al., 2011; MCDOUGALL; FEISTEL; PAWLOWICZ, 2013).

There are many classifications of water environments based on salinity concentrations which are not specifically related to estuarine environments, since salinity in water is not only a consequence of seawater intrusion but also can be present at different concentrations in other water systems, as rivers, lakes, aquifers, seas and oceans. The most common water classification based on salinity in shown in Table 2.

Table 2 – Salinity Range of different water sources.

Class	Salinity range (g/kg)
Freshwater	<0.5
Brackish water	0.5-30
Seawater	33-37
Saline water	30-50
Brine	>50

Source: Li; Liu (2019).

Freshwater presents low concentration of salinity (<0.5g/kg) and is common in ponds, lakes, stream, river and aquifers that are not affected by seawater intrusion, although the impacts of anthropogenic-induced changes on lakes are already pointed as responsible for changes in salinity (JEPPESEN et al., 2015). Brackish waters

(0.5g/kg – 30.0g/kg) are highly present in estuarine systems due to the mixing processes of freshwater and seawater, but this salinity range also occurs in brackish seas and some lakes, where evaporation rates are high, increasing the salinity concentration. Saline water (30.0g/kg to 50.0g/kg) is a general classification that includes seas and the ocean, in which seawater presents a variable salinity (33.0g/kg – 37.0g/kg), with an average salinity of 35.0g/kg. Finally, brine is a type of water with high concentration of dissolved salts, which can occur in salt lakes and on the ocean bottom (TALLEY et al., 2011; ALFREDINI; ARASAKI, 2013; JI, 2017; LI; LIU, 2019).

As salinity in measured indirectly based on EC, salinity sensors actually measures the water EC and temperature for further salinity calculation. EC is the ability of a substance to carry electric current and it can vary from very conductive materials, such as metals, to very nonconductive ones, as plastics. The SI unit for EC, or specific conductance, is Siemens per meter (S/m), but for water quality purposes, it is commonly used mS/cm or µS/cm. The simplest way to measure EC in water is the two-electrode cell arrangement by applying an alternate current wave form between them. Considering that the electrodes of the EC meter have a constant distance and a constant contact area with the external environment, a water sample at a specific temperature will always present the same EC. (LOCKRIDGE et al., 2016; CARMINATI; LUZZATTO-FEGIZ, 2017; RODRÍGUEZ RODRIGUEZ et al., 2018; LI; LIU, 2019).

In water environments, EC strongly depends on charged ions, which in most natural waters is a result of the concentration of dissolved salts. However, different elements will be more or less difficult to ionize in water solutions and, depending on the element, EC may not present a linear relation with salt concentration (Table 3). It is also affected by temperature, as an increasing temperature makes the water less viscous and ions can move easier.

Table 3 – EC values for typical samples.

Water sample at 25°C	EC (µS/cm)
Ultrapure water	0.055
Drinking water	50
Ocean water	53,000
5% $NaOH$	223,000
50% $NaOH$	150,000
10% HCl	700,000
32%HCl	700,000
31% HNO_3	865,000

Source: Li; Liu (2019).

Generally, EC in water samples varies from 1% to 3% per °C, depending on which salts are dissolved in water. The temperature variation effects in EC measurement in water environments are nonlinear, however, for general environmental water temperatures (0-30°C), a linear equation (eq 2.) is acceptable for its statistical admission and simple application (HAYASHI, 2014).

$$\sigma_0 = \frac{\sigma_t}{1 + A(T - T_0)} \quad (2)$$

In which

σ_0 :calibrated conductivity (mS/cm);

σ_t : conductivity at temperature T (mS/cm);

T : standardized temperature during sensor calibration (°C);

T_0 :measured temperature (°C);

A : temperature compensation factor (1/°C).

Salinity equation is a complex algorithm which also depends on EC, temperature and pressure, but this last plays negligible role in common estuarine systems, in which the water depth is of just few meters. Salinity is calculated using the dimensionless Practical Salinity Scale 1978 (PSS-78) (IOC; SCOR; IAPSO, 2010).

The conductivity ratio (R) can be defined as the ratio between the measured EC at a given environmental conditions (temperature and pressure) against the EC of a standard seawater of practical salinity 35 at 15°C and atmospheric pressure (0 dbar) (Eq. 3).

$$R = \frac{C(S_p, t, p)}{C(35, t = 15°C, 0)} \tag{3}$$

In which

R : conductivity ratio;

$C(S_p, t, p)$: measured EC (mS/cm);

$C(35, t = 15°C, 0)$:EC of the standard seawater, which is 42.914 mS/cm.

Salinity equations need temperature and pressure coefficient from standard seawater, which can be obtained from Eq. 4 and Eq. 5 that model the temperature and pressure variation of the EC of seawater.

$$r_t = \sum_{i=0}^{4} c_i t^i \tag{4}$$

In which

r_t : temperature coefficient.

$$R_p = 1 + \frac{\sum_{i=1}^{3} e_i p^i}{1 + d_1 t + d_2 t^2 + R(d_3 + d_4 t)} \tag{5}$$

In which

R_p : pressure coefficient.

It is important to notice that seawater conductivity increases by around 1% for a 1,000dbar pressure change, which means that for salinity measurements in estuarine rivers environment, the effect of pressure is negligible. The relation between R, r_t and R_p is a conductivity ratio (R_t), calculated as pointed in Eq. 6.

$$R_t = \frac{R}{R_p r_t} \tag{6}$$

In which

R_t: EC ratio.

Finally, practical salinity can be calculated through Eq. 7.

$$S_p = \sum_{i=0}^{5} a_i \left(R_t\right)^{\frac{i}{2}} + \frac{(t-15)}{\left[1+k(t-15)\right]} \sum_{i=0}^{5} b_i \left(R_t\right)^{\frac{i}{2}} \tag{7}$$

In which

S_p: practical salinity (psu);

k: constant equal to 0.0162.

The numerical values for the polynomial coefficients previous equation, which result from experimental measurements, are illustrated in Table 4:

Table 4 – Coefficients for Eqs. 4-7 to calculate salinity through PSS 1978.

i	a_i	b_i	c_i	d_i	e_i
0	0.0080	0.0005	6.766097×10^{-1}		
1	−0.1692	−0.0056	2.00564×10^{-2}	3.426×10^{-2}	2.070×10^{-5}
2	25.3851	−0.0066	1.104259×10^{-4}	4.464×10^{-4}	-6.370×10^{-10}
3	14.0941	−0.0375	-6.969800×10^{-7}	4.215×10^{-1}	3.989×10^{-15}
4	−7.0261	0.0636	1.003100×10^{-9}	-3.107×10^{-3}	
5	2.7081	−0.0144			

Source: IOC; SCOR; IAPSO (2010).

2.4 MICROELECTRONICS AND WATER QUALITY MONITORING

The conventional way of water quality monitoring is water sampling in different points and periods followed by laboratory analyses. Although this approach can very accurate, it is expensive, time-consuming and present low time and spatial resolution. Continued data acquisition in water monitoring systems through electronic sensors, with high spatial coverage and low time acquisition interval is more adequate for decision making processes in water resources management, reducing costs, equipment and in situ workload (ZHU et al., 2010; FAUSTINE et al., 2014; LAMBROU et al., 2014; BODDULA; RAMASWAMY; MISHRA, 2017; RANJBAR; ABDALLA, 2017).

On the other hand, the use of commercial water quality sensors with high temporal and spatial resolution is expensive and could be an obstacle for monitoring studies and researches. The cost of in situ water quality sensors is still the major limitation of their application and commercial sensors are generally patented technology, making it difficult to integrate data loggers and sensors across manufacturers (FAUSTINE et al., 2014; LOCKRIDGE et al., 2016; HORSBURGH et al., 2019).

Alternatively, the use of low-cost and self-made water monitoring sensors is an option that can make data collection feasible for long and extensive field surveys with moderate and low budgets. Since it is not a specific skill anymore, researchers with different backgrounds are able to design and build low-cost sensors due to its easy learning tools and accessible electronic components. Low-cost sensors can mean more monitoring stations and, consequently, more environmental data. In past years, Integrated Circuit Microcontrollers (ICM) has been an alternative as low-cost water quality data loggers (MARGOLIS, 2011; LOCKRIDGE et al., 2016; HORSBURGH et al., 2019).

One of the most applicable ICM is the free and open source Arduino microcontroller platform, based on a simple board and an Integrated Development Environment (IDE), which means, hardware and software interactions. The Arduino board executes the written code and interacts with the physical world through sensors or actuators. The Arduino IDE has a user-friendly interface, which includes a code editor, capable of compiling and uploading programs to the board, based on the

C/C++ language. The main benefits of using Arduino are (MARGOLIS, 2011; GERTZ; JUSTO, 2012; LOCKRIDGE et al., 2016; RODRÍGUEZ RODRIGUEZ et al., 2018):

a) Low-cost devices;
b) User-friendly software and hardware assembling;
c) Multiplatform environment, compatible with Windows, OS and Linux platforms;
d) Free and open source software and hardware design;
e) Active and supportive worldwide community through forums and sites.

There are many Arduino board types with different sizes, prices and applicability. The main differences between Arduino boards are the number of input/output pins, clock speed, operating voltage and the board design, but all of them are programmed through the Arduino IDE (Table 5).

Table 5 – Arduino boards and its technical specification.

Arduino Board	Microcontroller	Operating V	Clock speed	Digital I/O	Analog Inputs
Arduino Uno	ATMEGA328	5V	16MHz	14	6
Arduino Pro mini	ATMEGA328P	3.3V/5V	8MHz/16MHz	8	6
Arduino Nano	ATMEGA328	5V	16MHz	14	8
Arduino Leonardo	ATMEGA32u4	5V	16MHz	20	12
LilyPad Arduino	ATMEGA32u4	3.3V	8MHz	14	6
Arduino Mega	ATMEGA2560	5V	16MHz	54	16

Source: Margolis (2011); Jughes (2016).

The most popular Arduino board is the Arduino Uno, based on the ATmega328, which is an 8-bit microcontroller operated between 1.8-5.5V. This board has 14 digital input/output pins, 6 analog inputs and a USB connection. The Arduino Mega, based on the ATMEGA2560 microcontroller, which has 54 digital input/output pins and 16 analog inputs, is commonly applied to projects that requires more processing capabilities and pin connections (JUGHES, 2016). Figure 8 illustrated both Arduino boards.

Figure 8 – Arduino Uno and Arduino Mega.

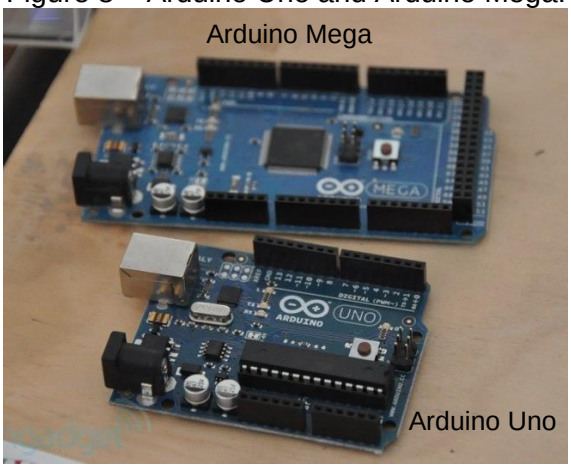

Source: Adapted from Margolis (2011).

The Arduino board executes the written C-language code and interacts with the physical world. It can occur through sensors, which convert an attribute from the physical world to electricity (e.g. switches, temperature sensors, ultrasound distance sensors); or through actuator, which get electricity from the board and convert it to affect some aspect of the physical world (e.g. LEDs, motors, displays).

The interface between the Arduino board and another circuit occurs through the digital Input/Output pins (I/O pins) and the analog pins. Digital I/O pins have only two logic states: HIGH or logic “1” state and LOW or logic “0” state. If the pin is configured as an Output pin, it will provide 5V (HIGH state - 1) or 0V (LOW state - 0) to whatever is connected to it; if the pin is configured as an Input pin, it will sense the presence or absence of voltage on it by reading the voltage as a voltmeter and return to the software HIGH state - 1 if V is close to 5V or LOW – 0 if it is close to 0V.

Analog pins are generally used as Input pins, but differently from the digital pins, that have only two logic states, the Arduino converts the value of the analog voltage into a digital value (A/D converter), returning integers from 0 to 1023, which is generally used to read analog sensors.

As the Arduino board interacts with the physical world, the electronic circuit may depend on electronic components such as batteries, resistors, capacitors, transistors and other integrated circuits in order to work adequately, which will be briefly described.

The Arduino Board can be powered from an external power source, in which the voltage and current range are limited by each board specification. Batteries can be arranged in a serial arrangement to increase the voltage or in a parallel arrangement

to increase current. Four batteries in series, for example, will generate the current of one cell, but the voltage will be four times that of a single cell. In general, Arduino boards have an upper voltage limit of 12V; higher values may overheat its voltage regulator, affecting its operation. Battery current is rated in milliampere-hour (mAh), which is the amount of milliamperes it can supply in one hour. Table 6 shows typical batteries used in Arduino projects and its voltage and current.

Table 6 – Typical industrial batteries specification.

Battery type	Nominal voltage	Mean mAh capacity
AAA (Alkaline)	1.5V	1200 mAh
AA (Alkaline)	1.5V	2700 mAh
C (Alkaline)	1.5V	8000 mAh
D (Alkaline)	1.5V	12000 mAh
9V	9V	600 mAh
Button Cell (Lithium) – CR2032	3V	240 mAh

Resistors are used to limit the flow of the electrical current by being made of materials that conduct electricity badly, i.e. they reduce the intensity of the electrical current. This current regulation is extremely important in microelectronic circuits because electronic components present different operational currents and they can be easily damaged if a current higher than allowed passes through them, so resistors protect those components by reducing the electricity that reaches them.

Additionally, resistors can be used to pull-up or pull-down electrical signals. Input pins can only have HIGH or LOW logic states, but when the pin is connected to a switch and it is in the open state, the input pin can be “floating” (unknown voltage), resulting in unpredictable results. In order to prevent this undesirable voltage, floating inputs, it is necessary to impose a default state to the input pin as HIGH or LOW logic state. In other words, pull-down or pull-up resistors are used to “pull” the input pin to a known state when the switch is open. For example, when a switch that connects an input pin to the ground (GND) is closed, voltage would be 0V, which is expected, but if the switch is open, it is not possible to confirm what its voltage is. So, a resistor is used to impose a default state of the pin, even if the switch is open, closed or there is nothing connected to it. Figure 9 illustrates simple schematics of pull-up and pull-down resistors.

Figure 9 – Pull-up and pull-down resistors schematics.

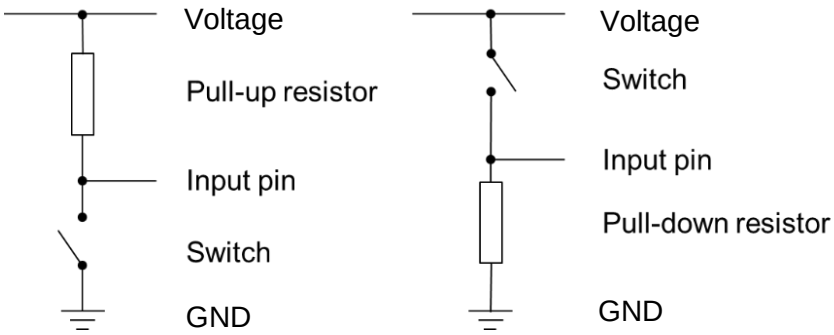

Summarily, pull-up resistors connect the input pin to V; if a pull-up resistor is used, the input pin will be HIGH when the switch is open and LOW when the switch is closed. Pull-down resistors connect the input pin to the GND; if a pull-down resistor is used, the input pin will be LOW when the switch is open and HIGH when the switch is closed.

Capacitors are used to store electrical charge for a short period and are frequently used in electronic circuits as coupling capacitors or decoupling capacitor. Coupling capacitors are applied in series to the signal path to filter out the DC component of electrical signals, in which AC signals are desired and DC are just used for providing power, but should not appear in the output. Decoupling capacitors are essentially the opposite: they are connected in parallel to the signal path to filter out voltage spikes and pass through only the DC component of the signal, making it as smooth as possible. In circuits in which signals are switched on and off rapidly, this fluctuation can affect the signal and the impact the circuit operation. Nonpolarized ceramic type works as decoupling capacitor in electronic circuits to filter these fluctuations and protect the circuit; and electrolytic capacitor, usually polarized, are used for higher current circuits for the same purpose.

Transistors are semiconductors that can be used to amplify or switch on high currents or high voltages in digital circuits; and amplify signals in digital circuits. One of the most common types of transistor is the Metal Oxide Semiconductor Field Effect Transistor (MOSFET), which in electronic circuits can be used to shut down the system and reduce energy consumption by controlling the current flow by voltage variation. In other words, the MOSFET works as a switch that cuts the power from the circuit. Figure 10 illustrates a standard MOSFET pinout.

Figure 10 – Standard MOSFET pinout.

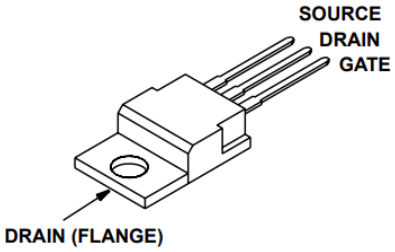

Source: VISHAY, 2011

MOSFETs commonly have three pins, called Source, Gate and Drain. In the Source pin, the current flows out through it, thus, it is connected to the electronic components that need power supply. The Gate pin controls the biasing of the transistor, turning on or off the load at the Drain, working as a switch. In the Drain pin, the current flows in through it, thus, it is connected to GND. It works in a simple way: when voltage is applied between the Gate and the Source, current is allowed to flow between the Drain and the Source. With a low voltage at the Gate, the resistance from the Drain to Source is very high; as the voltage increases at the Gate, the threshold voltage is exceeded and the resistance from the Drain to Source decreases quickly. Even electrostatic voltages can turn the loads, so it is adequate to put a pull-down resistor between Gate and Source in order to avoid it.

General integrated circuits have many practical applications in microelectronics and are present in virtually all electronic equipment and timers are an IC type widely used in Arduino circuits. The standard 555 series general-purpose chips are the most common timers in the world and can be used as timer, pulse generator or oscillator due to its stability, simplicity and cost-benefit ratio. Figure 11 illustrates the a 555 Timer Integrated Circuit (IC) in its 8-pin Dual in-line package (DIP) configuration and Table 7 describes each pin function.

Figure 11 – 555 IC in its 8-pin DIP configuration.

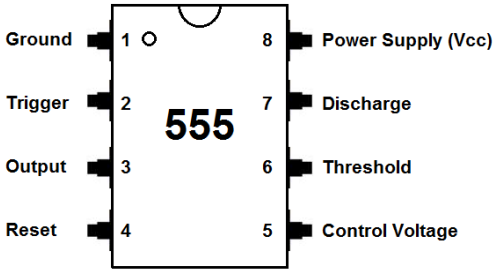

Source: Adapted from Texas Instruments, 2019.

Table 7 – 555 IC pins functions.

Pin	Function
Pin 1 – Ground (GND)	It connects the 555 IC to the ground voltage (0V).
Pin 2 – Trigger	An Input pin that when its voltage falls below $1/3$ Vcc, the 555 IC is triggered and the Output pin (Pin 3) switches from LOW to HIGH state.
Pin 3 – Output	It is capable of sourcing up to 200mA of current at HIGH state (positive supply at Pin 8 – approximately 1.5V Vcc). At LOW state it is capable of sinking (ground supply at Pin 1 – GND). Small speakers, LEDs or motors can be connected directly to the output.
Pin 4 – Reset	It is an Input pin used to reset the internal controlling state of the Pin 3 (Output). In most applications this pin is not used, thus it should be connected to Vcc to prevent electrical noise causing a reset.
Pin 5 – Control Voltage	It is an Input pin that provides access to the internal voltage divider ($1/3$ Vcc). In most applications this pin is also not used.
Pin 6 – Threshold	It is an Input pin that detects when V on the timing capacitor rises above $2/3$ Vcc and Pin 3 (Output) switches from HIGH to LOW state.
Pin 7 – Discharge	It is an Output pin that is used to “discharge” the timing capacitor to GND when pin 3 (Output) switches to LOW state pin.
Pin 8 – Vcc	This is the power supply pin. In general, it can vary from 4.5V to 15V.

Source: Adapted from Texas Instruments, 2019.

The 555 IC has three different operating modes, which means, three different multivibrator schemes:

a) Astable mode. Also known as free-running mode, the 555 can work as square wave oscillations generator (pulses), for example. The use of

microcontrollers can then convert the pulses to different variables, such as temperature;

b) Monostable mode. As the name suggests, the 555 functions as a “single shot” pulse generator. It can be used as frequency dividers, capacitance measurement, pulse-width modulation (PWM), etc.;
c) Bistable mode. The 555 operates as a flip-flop, with two different trigger inputs. They are applied to change the state from HIGH to LOW and LOW to HIGH. It is used in automatic switching applications, to generate pulse of variable time, etc.

2.5 HYDRODYNAMICS AND WATER QUALITY MODELING

The management of estuarine systems requires monitoring of quantitative and qualitative information for a complete understanding of its processes, since water management should be founded in adequate understanding of water availability and movement. The prediction of the estuarine system behavior through modeling tools gives background information and is crucial to assess the estuarine response to current or future impacts from human activities or its own natural performance as a result of different environmental forcing conditions, as channel configuration, upstream discharge, water abstraction, low flow scenarios, high precipitation events and flow diversion (UNESCO, 1991; RICH; MAIER, 2015; VARGAS; VAZ; DIAS, 2017).

A mathematical model represents the water dynamics and the water quality processes using mathematical equations, which generally needs to be solved numerically by a computer. In other words, a mathematical model is a prediction method, described as an idealized formulation with a set of coupled, nonlinear partial differential equations to represent the response of a water body to a specific set of forcing conditions. This set of equation is then converted into a computer code, i.e. a computer model. A computer simulation, in its turn, is a representation of the surface water system using a computer model. With adequate data, the execution of the computer model gives a close solution to the mathematical model (JAMES, 1993; CHAPRA, 1997; YOON; WOO, 2015; JI, 2017).

The main reasons to perform a hydrodynamic and water quality modeling is to better understand the physical, chemical and biological processes in a water body; and predict different scenarios in order to support water resources management and decision making processes (MARTIN; MCCUTCHEON, 1999; PINHO; VIEIRA, 2007; HADDOUT; IGOUZAL; MASLOUHI, 2017).

Even though a real water body is obviously always three dimensional, it will not necessarily be modeled as a three dimensional body. If the property variation in a dimension can be considered insignificant or can be represented by averaged values, this spatial dimension can be excluded from the modeling analysis. The spatial characteristics of numerical models include the number of dimensions simulated and the spatial resolution, which can be (MARTIN; MCCUTCHEON, 1999):

a) Zero-dimensional model (0D);
b) One-dimensional model (1D);
c) Two-dimensional model (2D);
d) Three-dimensional model (3D).

A zero-dimensional model (0D) is the result of averaging the equations over the entire volume of water. In this kind of models, there is no equation for momentum, which means that there are only the volume-averaged equations for continuity and constituent transport. Considering the current computer capacity, zero-dimensional models are no longer interesting to use.

In the one-dimensional model (1D), the averaging is over the cross-section, resulting in a longitudinal model. Shallow and small rivers and streams can be adequately represented in 1D horizontal (1DH) models, while lakes and reservoir can be modeled in 1D vertical models (1DV). Generally, in one-dimensional models, the hydrodynamics and water quality processes are analyzed in the direction of the flow (MARTIN; MCCUTCHEON, 1999; HADDOUT; IGOUZAL; MASLOUHI, 2017; JI, 2017).

Two-dimensional models can be depth-averaged (2DH) or laterally averaged (2DV). The first one solves differences along the width and length of the water body, while the second solves differences along the length and the depth of the water body. Estuaries with shallow waters and large surface areas can be modeled in 2DH

models, while 2DV models are commonly used in long, narrow and deep waters (CHAPRA, 1997; MARTIN; MCCUTCHEON, 1999; JEONG et al., 2010).

The three-dimensional models (3D) are the most complete and complex models, because they provide the closest approximation to reality by simulating gradients along all three of the spatial dimensions. They represent both vertical and horizontal hydrodynamics and water quality processes and are adequate to simulate all types of water bodies (CHAPRA, 1997; JI, 2017). Figure 12 illustrates the spatial dimensions of water models.

Figure 12 – Spatial dimensions of surface water models.

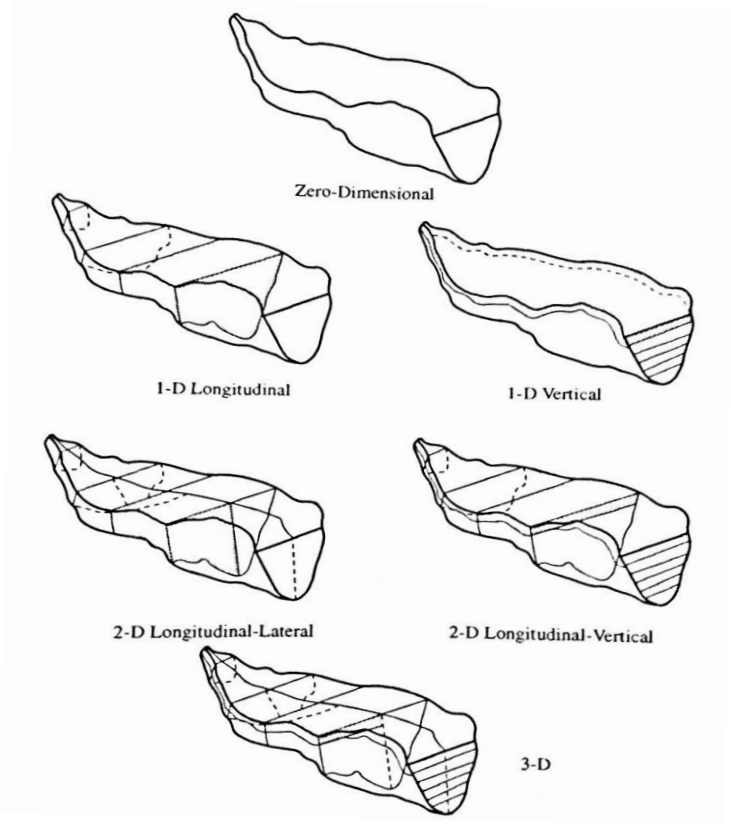

Source: Martin and Mccutcheon (1999).

In general, 2D and 3D models are more time-consuming and require more input data than 1D models, so 1D models can be a reliable tool for hydrodynamics and water quality modeling, presenting satisfactory results, when the considered problem can be simplified to a profile-averaged approach. Even considering that 2D and 3D models present more representative results, their implementation can face practical issues due to difficulties in field data acquisition for model inputs. So, for engineering

purposes, 1D hydrodynamic and water quality models can be a more feasible prediction method, as these models require less observed data and, consequently, less fieldwork.

In order to solve the hydrodynamic and water quality equations numerically and perform a computer simulation, it is necessary to set boundary conditions and initial conditions. Considering that the water system to model is confined in a determined area, it is mandatory to specify the driving forces that cause flow and water quality changes at the limit of the model domain. In other words, a model does not calculate the boundary conditions for itself, but it is affected by them (ETEMAD-SHAHIDI et al., 2015; JI, 2017).

Typical hydrodynamic boundary conditions are inflows, outflows and water surface elevations. In a river, for example, it is possible to classify the boundary conditions as upstream, lateral and downstream boundaries (Figure 13):

a) Upstream boundary. It provides inflows to the river and is often described as a flow rate or water surface level (1);
b) Lateral boundary. It specifies lateral inflows that can come from gauged and ungagged areas along the river (2);
c) Downstream boundary. It describes the hydraulic condition at the downstream limit of the model. Water surface elevations or a rating curve are often specified at the downstream boundary. In tidal rivers, the usual downstream boundary condition is a tidal stage level, which can cause reversing flows (3 and 4).

Figure 13 – Model boundary conditions

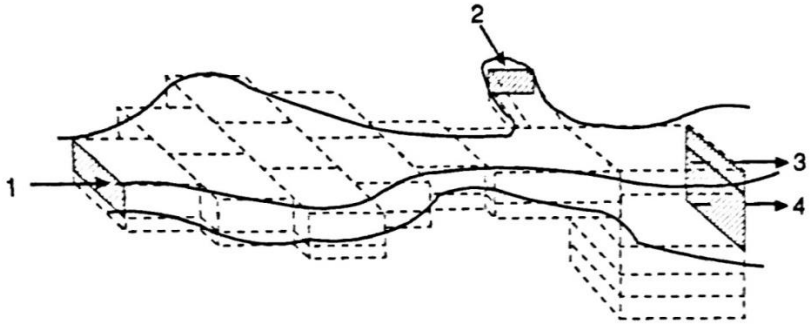

Source: Martin and Mccutcheon (1999).

Initial conditions represent the environmental values at the beginning of the simulation. The water system simulation will start from these initial conditions at each grid point of the model domain. They are required only when a time dependent simulation is conducted, i.e. for a non-steady-state model. Generally, initial conditions are more significant when the simulation period is shorter than the time required for these conditions to be expelled. The impact of initial conditions on model results is to perform an adequate spin-up time, which is the time taken for a numerical model to reach a state of statistical equilibrium under the applied forcings (JAMES, 1993; CHAPRA, 1997; JI, 2017).

Adequate boundary conditions can also be useful to reduce the impacts of initial conditions inconsistencies by “flushing out” the initial conditions quickly. However, the effects of these conditions are significant in the initial period of about one to five times the residence time. Hence, in systems with short retention times, such as a flowing river, the initial conditions will cause a minimal effect on the model results, because the initial values are rapidly eliminated and the model skips the initial conditions in a short period (JI, 2017).

Mathematical models use parameters in their equations, which must be adjusted in order to represent adequately a specific characteristic of a particular water body. In the development and application of a mathematical model, there are commonly three stages (MALONE et al., 2015):

a) Calibration;
b) Validation (verification);
c) Application for predictive purposes.

Model calibration is the process by which one finds the geometric, discharge and mixing parameters which best describe the hydrodynamic and water quality behavior through comparison with field observation. The mathematical model may satisfactorily reproduce the governing factors, such as river discharge and tidal activity.

Validation or verification is the testing of calibrated models under different forcing conditions. Validation is designed to confirm that the calibrated model is applicable over a limited range of conditions; it compares the model results with

numerical data independently derived from experiments or observations of the environment (DAGGUPATI et al., 2015).

Finally, after the calibration and validation steps, the model can be used to make extrapolations and be applied for predictive purposes under a wider range of forcing conditions than the used for calibration and validation purposes.

Observation is the only way to know the real aspects of the water system and to provide the basis for numerical modeling. The majority of water processes cannot be properly described in numerical models before they are measured in real water bodies. If a model can adequately simulate the measured data from the water body, the model can be used for future applications with confidence (MALONE et al., 2015; MATTE; SECRETAN; MORIN, 2017).

Statistical analyses are applied to evaluate the model performance and there is a vast number of statistical tools for it. The most common coefficients or indexes used in hydrodynamic and water quality modeling are:

a) Root mean square error (RMSE);
b) Coefficient of determination (R^2);
c) Nash-Sutcliffe efficiency index (EF);
d) Predictive skill (skill).

The RMSE is a quantitative comparison between the observed and the simulated data. It gives and absolute value of observation-simulation discrepancies and measures the size of error in percentage terms (eq. 8).

$$RMSE = \sqrt{\frac{1}{n}\sum (O - S)^2} \tag{8}$$

In which

n: number of observation-simulation pairs;

O: observed value;

S: simulated value.

The coefficient of determination (R^2) illustrates how many data points fall within the results of the line formed by the regression equation (eq. 9).

$$R = \frac{n\left(\sum OS\right) - \left(\sum O\right)\left(\sum S\right)}{\sqrt{\left[n\sum O^2 - \left(\sum O\right)^2\right]\left[n\sum S^2 - \left(\sum S\right)^2\right]}} \quad (9)$$

In which

R: correlation coefficient.

Another statistical indicator used for evaluate model performance is the Nash-Sutcliffe efficiency index (EF) (eq. 10)

$$EF = 1 - \left[\frac{\sum_{i=1}^{n}(O-S)^2}{\sum_{i=1}^{n}\left(O-\overline{O}\right)^2}\right] \quad (10)$$

In which

$\overline{O}$: mean observed value.

The EF can vary from $-\infty$ to 1 (inclusive). The closer the EF efficiency to 1, the more accurate is the performance. Values ≥0.75 are considered good levels of performance; between 0.36 and 0.75 are considered acceptable, while values ≤0.36 indicate an unacceptable performance (HADDOUT; IGOUZAL; MASLOUHI, 2016; JI, 2017).

The predictive skill (skill) provides an index of observed and simulated data agreement and is being strongly used in recent studies (eq. 11):

$$skill = 1 - \frac{\sum_{i=1}^{n}|S-O|^2}{\sum_{i=1}^{n}\left(\left|S-\overline{O}\right| + \left|O-\overline{O}\right|\right)^2} \quad (11)$$

A skill value of 1.0 indicates a perfect performance of the model, excellent for skill between 0.65 and 1.0, very good for skill in a range of 0.5 to 0.65, good for skill in the range of 0.2 to 0.5 and poor for skill less than 0.2 (CHEN et al., 2016; JI, 2017; VARGAS; VAZ; DIAS, 2017; WANG et al., 2019).

There are a significant number of applications of hydrodynamic and water quality models to study salinity behavior in estuarine systems. In the past few years, several studies have been conducted to investigate estuarine responses to climate change effects, such as alteration of freshwater discharge and SLR, and their relation with seawater intrusion.

Haddout, Igouzal and Maslouhi (2016) applied the 1D HEC-RAS model to study the seawater dynamics in the Sebou River estuary (Morroco) under different tide and freshwater discharge forcing conditions. The seawater intrusion dynamics were analyzed considering high tide and low tide for high flow and low flow conditions. The results showed a good agreement between computed and observed salinity concentration; and that high river flow prevents strong seawater intrusion for both low and high tide. On the other hand, seawater intrusion is much more intense during high tides combined with low river discharge. Even 1D hydrodynamics and water quality models can be useful for seawater intrusion studies.

Saran, Rahman and Yunus (2018) carried out a study on salinity intrusion dynamics using the 1D HEC-RAS model of Rupsha-Passur river system, connected to the Bay of Bengal, in Bangladesh. The model performed simulations under different flow scenarios, with 15% and 40% increase and 15% and 40% decrease flow condition at the upstream boundary condition. The results showed that during the dry season the salinity concentration increases significantly in the study area, which may be exacerbated under decreased flow conditions. Higher seawater intrusion in Rupsha-Passur river system may impact the agriculture and the local mangrove forest.

Etemad-Shahidi et al. (2015) also applied a 1D hydrodynamics and water quality model (Mike11) to investigate the SLR impact on salinity intrusion in Bahmanshir estuary, on the Iranian-Iraqi border, connected to the Persian Gulf. The 1D model simulated SLR scenarios varying from 30 to 90cm by 2100 and flow ranging from 20m³/s to 700m³/s, based on historical records. The results showed that the seawater intrusion length is inversely correlated with the discharge and directly

related with SLR. In the most severe scenario, the seawater intrusion length may reach 32 km and significantly affect the water uses.

Vargas, Vaz and Dias (2017) investigated the SLR impacts for both wet and dry season on salinity patterns in Ria de Aveiro, Portugal, using the 3D MOHID water modeling system, developed at Lisbon University. Salinity patterns were evaluated under a reference scenario, considering the current mean sea level, and under future scenarios, considering a SLR of 0.42cm. The freshwater flow reduction was 22% for the wet season and 87% for the dry season. Main results showed an upstream displacement of saline fronts under all future scenarios and that the SLR had a more important impact on seawater intrusion than the river flow reduction.

Wang et al. (2019) studied the seawater intrusion behavior under different forcing conditions in Indus River Estuary, in Pakistan, by applying the 3D FVCOM numerical model. The model run hydrodynamic and water quality simulations considering a dry season, with 0m³/s and only the tides as downstream forcing conditions; a low river discharge (30m³/s); a normal river discharge (300m³/s); and a flood event (3000m³/s). Results showed seawater intrusion was extremely dependent on the seasonally of fluvial discharge, in which during the seawater intrusion length varies from 65km in the dry season to 8km in the wet season. When there is a flood river discharge, the seawater is flushed out downstream the river in ebb and flood tide.

Chua and Xu (2014) investigated the impacts of SLR on seawater intrusion in San Francisco Bay (USA) using the 3D SUNTANS hydrodynamic model. Firstly, they investigated the salinity dynamics on an idealized estuary for approximation on the effects of SLR and freshwater inflows on salinity dynamics. Secondly, simulations were performed for San Francisco Bay considering inflows discharges of 300, 800 and 2000m³/s and SLR ranging from 0 to 1.39m. Results showed the required discharge to maintain seawater intrusion length standards for future SLR scenarios, indicating that higher discharges will be required to flush seawater out San Francisco Bay considering future SLR scenarios.

Chen et al. (2016) analyzed the impacts of SLR on seawater intrusion in Yangtze River estuary, China, using the MIKE3 hydrodynamic and water quality model. The simulated sea level scenarios were the present sea level and SLR of 0.5, 1 and 2m. All SLR scenarios were simulated considering low river discharge to

represent the dry season. In all cases, seawater intrusion moves upstream, but in the 2m SLR scenario, the salinity concentration exceeds the Chinese standard for drinking water intake during the dry season at four reservoirs that are used for water supply. Additionally, under SLR of 1m, even the operation of three gorges reservoir is not sufficient to flush the salinity out the lower reach of the North branch of the estuary.

2.6 HEC-RAS MODEL

The U.S. Army Corps of Engineers River Analysis System (HEC-RAS) is a free software developed by the Hydrologic Engineering Center that allows the user to perform one-dimensional steady flow, one and two-dimensional unsteady flow and water quality modeling. All those components are linked and the software uses a unique geometric data and hydraulic routine. The unsteady flow simulation is adequate to simulate one-dimensional unsteady flow in a network of channel and floodplains; perform subcritical, supercritical or mixed flow regimes calculations (BRUNNER, 2016a).

In addition to the flow routing capability, HEC-RAS incorporates a water quality module, which can perform water quality analysis of negative flows that are observed within an estuary during an incoming tide. In order to run the water quality model, a working unsteady or steady flow model must be already done. In contrast to 3D models, HEC-RAS is a 1D hydraulic model does not account multi-directional flows or variations in fluid density. However, considering the geometry of an estuarine river, HEC-RAS was expected to reasonably represent the hydraulic and the depth averaged salinity behavior (BRUNNER, 2016a).

HEC-RAS has some strong points, such as the support of the USACE; the progresses that constantly made; and its acceptance by many government agencies and research centers. It is also in the public domain and peer-reviewed (ANDREI, et al., 2017). This model has been strongly applied in recent hydraulic and water quality researches. Hanks (2011) applied the 1D and water quality capabilities of HEC-RAS to evaluate the salinity distribution in the Caloosahatchee Estuary (USA). The model was able to simulate scenarios of changing sea level boundary conditions due to climate change and delivered consistent results. Rahman; Zobeyer (2015) used the

1D model to study the dry period flow and salinity characteristics of the Passur River (Bangladesh). This study was conducted to evaluate the salinity intrusion in sea level rise scenarios and its possible impacts on crop production and aquaculture near the river. Haddout; Igouzal; Maslouhi (2016) analyzed the impact of the combination of a supermoon and a total lunar eclipse on the salinity intrusion in the Sebou River estuary (Morroco). The HEC-RAS presented good fit between the computed salinity and the field measurements, indicating that the model is adequate to perform 1D models and deliver consistent results.

2.6.1 Unsteady Flow Simulation

For one-dimensional unsteady flow hydrodynamics, the physical laws that describe the flow of water in a river are the principle of conservation of mass (continuity equation) and the principle of conservation of momentum (momentum equation) (BRUNNER, 2016a, 2016b). Figure 14 illustrates the control volume for those equations.

Figure 14 – Control volume for continuity and momentum equations.

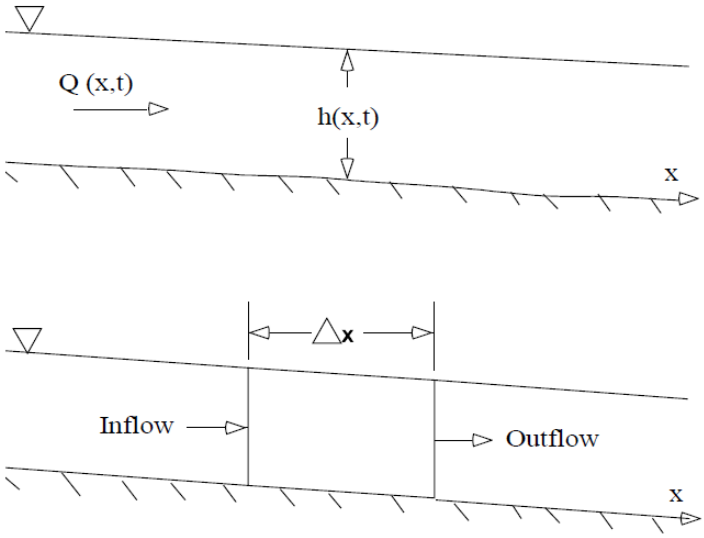

Source: Brunner (2016b).

The channel capacity can be determined using the continuity equation:

$$Q = UA \tag{12}$$

In which

Q: channel discharge (m^3/s);

U: mean velocity (m/s);

A: channel cross-section area (m^2).

As indicated, the average velocity in a channel cross-section (V) is the total discharge divided by the cross-sectional area of flow perpendicular to the cross-section. It is only a general indicator and does not reflect the horizontal and vertical variation in velocity. However, for one-dimensional analysis, the vertical velocity is neglected and the horizontal velocity distribution is estimated by subdividing the channel cross section and computing average velocities for each subsection. The resulting velocities represent a velocity distribution. The mean velocity can be determined using the Manning equation:

$$U = \frac{Rh^{\frac{2}{3}} S_f^{\frac{1}{2}}}{n} \tag{13}$$

In which

Rh: hydraulic radius (m);

S_f: slope of energy grade line (m/m);

n: Manning's roughness coefficient ($s/m^{\frac{1}{3}}$).

Selection of adequate value for Manning's coefficient is very important to the accuracy of the computed water surface elevations. It is strongly variable and depends on the surface roughness, vegetation, channel irregularities, obstructions, size and shape of the channel, discharge, temperature, etc. Generally, n is calibrated with observed water surface elevation data.

The hydraulic radius is a geometric relation between the cross-section area and the wetted perimeter (the length of the channel boundary in direct contact with the water):

$$Rh = \frac{A}{P} \tag{14}$$

In which

P: wetted perimeter (m).

Combining Eq. 12 with Eq. 14, it is possible to determine the channel uniform flow capacity:

$$Q = \frac{ARh^{\frac{2}{3}}S_f^{\frac{1}{2}}}{n} \tag{15}$$

In channel analysis, it is often convenient to group the channel cross-sectional properties in a single term called the channel conveyance (K). It combines the roughness and geometric characteristics of the channel:

$$K = \frac{ARh^{\frac{2}{3}}}{n} \tag{16}$$

Substituting Eq. 16 in Eq. 15:

$$Q = K\sqrt{S_f} \tag{17}$$

Thus, rearranging the Eq. 17, the friction slope (slope of the energy grade line) at each cross section is:

$$S_f = \left(\frac{Q}{K}\right)^2 \tag{18}$$

Conservation of mass for a control volume states that the net rate of flow into the volume is equal to the rate of change of storage inside the volume. In other words, inflow minus outflow equals the change in storage over time. The rate of inflow to the control volume is:

$$Q - \frac{\partial Q}{\partial x}\frac{\Delta x}{2} \tag{19}$$

The outflow rate is:

$$Q + \frac{\partial Q}{\partial x}\frac{\Delta x}{2} \tag{20}$$

And the rate of change in storage volume is:

$$\frac{\partial A_T}{\partial t}\Delta x \tag{21}$$

In which

A_T: total flow area cross section (m²).

Thus, the change of mass in the control volume is:

$$\rho\frac{\partial A_T}{\partial t}\Delta x = \rho\left[\left(Q - \frac{\partial Q}{\partial x}\frac{\Delta x}{2}\right) - \left(Q + \frac{\partial Q}{\partial x}\frac{\Delta x}{2}\right) + Q_f\right] \tag{22}$$

In which

ρ: fluid density (kg/m³);

$\frac{\partial A_T}{\partial t}\Delta x$: change in storage over time;

$Q - \frac{\partial Q}{\partial x}\frac{\Delta x}{2}$: rate of inflow to the control volume;

$Q + \frac{\partial Q}{\partial x}\frac{\Delta x}{2}$: rate of outflow to the control volume;

Q_f: lateral flow entering the control volume (m³/s).

Considering that the fluid is incompressible and the Δx is constant, the final form of the continuity equation is:

$$\frac{\partial A_T}{\partial t} + \frac{\partial Q}{\partial x} - q_l = 0 \tag{23}$$

In which:

q_l: lateral inflow per unit length ((m³/s)/m).

In HEC-RAS, the momentum equation is applied when the water surface passes through critical depth, when occur the transition from subcritical to supercritical or from supercritical to subcritical flow. It can take place, for example, in great channel slopes, stream junctions, the occurrence of hydraulic jumps and low flow at bridges (BRUNNER, 2016b). The momentum equation can be derived from the Newton's second law:

$$\sum F_x = ma \tag{24}$$

In which:

F_x: resulting force in x-direction (N);

ma: change in momentum (kgm/s²).

Considering the Eq. 24 in a control volume (Figure 15), the resulting forces and the change in momentum can be expressed as:

Figure 15 – Application of the momentum principle

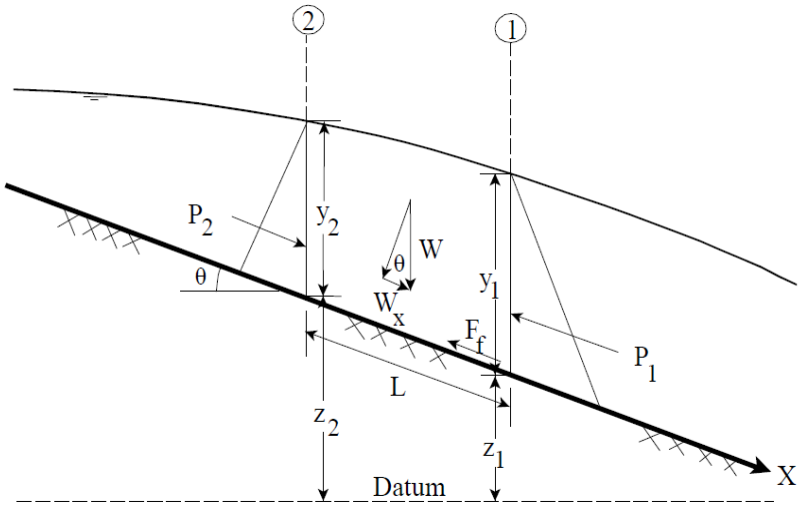

Source: Brunner (2016b).

$$P_2 - P_1 + W_x - F_f = \rho Q \Delta U_x \tag{25}$$

In which

P: hydrostatic pressure force at points 1 and 2 (Pa);

W_x: weight force in the x-direction (N);

F_f: friction force (N);

ΔU_x: change in velocity in the x-direction (m/s).

The conservation of momentum for a control volume is the net rate of momentum entering the volume (momentum flux) plus the sum of all external forces acting on the volume is equal to the rate of accumulation of momentum.

$$M_f + \sum F_x = \frac{d\vec{M}}{dt} \tag{26}$$

In which

M_f: net rate of momentum entering the volume (momentum flux) ;

$\sum F_x$: sum of all external forces;

$\frac{d\vec{M}}{dt}$: rate of accumulation of momentum.

The sum of all forces acting on a control volume in the x-direction at a particular instant “n” time can be described as the body forces that act on the entire body of the control volume and the surface forces that act on the control surface:

$$\sum F_x = \sum \vec{F}_{body} + \sum \vec{F}_{surface} \tag{27}$$

The external forces considered are:

a) Gravity force (Body force);

b) Pressure force (Surface force);

c) Friction or viscous force (Surface force).

Thus, the Eq. 27 can also be expressed as:

$$\sum F_x = \vec{F}_g + \vec{F}_P + \vec{F}_f \tag{28}$$

Gravity Force ($\vec{F}_g$): The gravity force in a control volume in the x-direction is:

$$F_g = \rho g A \sin\theta \, \Delta x \tag{29}$$

In which

θ: the angle that the channel's bed makes with the horizontal;

For natural rivers, the angle θ is generally small and the following approximation is possible:

$$\sin\theta \approx \tan\theta = -\frac{\partial z_0}{\partial x} \tag{30}$$

In which

z_0: channel's bed elevation (m).

Thus, the Eq. 30 can be written:

$$F_g = -\rho g A \frac{\partial z_0}{\partial x} \Delta x \tag{31}$$

Pressure Force: Assuming that the pressure distribution is hydrostatic (it varies linearly with depth) and considering that F_p is the pressure force in the x-direction at the midpoint of the control volume, the pressure force at the upstream section of the control volume is:

$$F_p - \frac{\partial F_p}{\partial x} \frac{\Delta x}{2} \tag{32}$$

At the downstream section of the control volume:

$$F_p + \frac{\partial F_p}{\partial x} \frac{\Delta x}{2} \tag{33}$$

The sum of the total pressure forces for a control volume is:

$$F_P = \left|F_p - \frac{\partial F_p}{\partial x}\frac{\Delta x}{2}\right| - \left|F_p + \frac{\partial F_p}{\partial x}\frac{\Delta x}{2}\right| + F_B \quad (34)$$

In which

F_P: net pressure force for the control volume;

F_B: force exerted by the bank in the x-direction on the fluid.

The Eq. 34 can be simplified to:

$$F_P = -\frac{\partial F_p}{\partial x}\Delta x + F_B \quad (35)$$

Assuming that the pressure force exerted by the fluid on the banks is equal in magnitude to F_B(Eq. 34) the net pressure force for a control volume is:

$$F_P = -\rho g A \frac{\partial h}{\partial x}\Delta x \quad (36)$$

Viscous Force: Viscous forces between the channel and the fluid is:

$$F_f = -\tau_0 P m \Delta x \quad (37)$$

In which

τ_0: average boundary shear stress on the fluid boundaries (Pa).

The relation between magnitude of the bed shear-stress (τ_0) and the depth-averaged velocity is:

$$\tau_0 = \rho C_d U^2 \quad (38)$$

In which

C_d: drag coefficient.

Instead of drag coefficient C_d the Chézy coefficient can be used. They are related by:

$$C_d = \frac{g}{C^2} \tag{39}$$

In which

C: Chézy coefficient ($m^{\frac{1}{2}}/s$).

Further, the Chézy formula describes the mean flow velocity:

$$U = C\sqrt{RhS_f} \tag{40}$$

Substituting Equation 38, Equation 39 and Equation 40 in Equation 37:

$$F_f = -\rho g A S_f \Delta x \tag{41}$$

Momentum flux: the flux entering the control volume is described as:

$$\rho\left(QU - \frac{\partial(QU)}{\partial x}\frac{\Delta x}{2}\right) \tag{42}$$

And the flux leaving is:

$$\rho\left(QU + \frac{\partial(QU)}{\partial x}\frac{\Delta x}{2}\right) \tag{43}$$

Thus, the momentum flux entering the control volume is:

$$-\rho\frac{\partial(QU)}{\partial x}\Delta x \tag{44}$$

Considering that the momentum in a control volume is $\rho Q \Delta x$ (modifying Eq. 25), the rate of accumulation of momentum is:

$$\frac{\partial}{\partial t}(\rho Q \Delta x) = \rho \Delta x \frac{\partial Q}{\partial t} \tag{45}$$

Substituting Eq. 44, Eq. 31, Eq. 36, and Eq. 41 in Eq. 26:

$$-\rho \frac{\partial (QU)}{\partial x} \Delta x - \rho g A \frac{\partial z_0}{\partial x} \Delta x - \rho g A \frac{\partial h}{\partial x} \Delta x - \rho g A S_f \Delta x = \rho \Delta x \frac{\partial Q}{\partial t} \tag{46}$$

Rearranging Eq. 46:

$$(\rho \Delta x) \frac{\partial Q}{\partial t} = (\rho \Delta x) \left(-\frac{\partial (QU)}{\partial x} - g A \frac{\partial z_0}{\partial x} - g A \frac{\partial h}{\partial x} - g A S_f \right) \tag{47}$$

Dividing through by $\rho \Delta x$ and then considering gA a common factor:

$$\frac{\partial Q}{\partial t} = -\frac{\partial (QU)}{\partial x} - g A \left(\frac{\partial z_0}{\partial x} + \frac{\partial h}{\partial x} + S_f \right) \tag{48}$$

The elevation of water surface (z) is equal to $z_0 + h$, so:

$$\frac{\partial z}{\partial x} = \frac{\partial z_0}{\partial x} + \frac{\partial h}{\partial x} \tag{49}$$

Substituting Eq. 49 in Eq. 48:

$$\frac{\partial Q}{\partial t} = -\frac{\partial (QU)}{\partial x} - g A \left(\frac{\partial z}{\partial x} + S_f \right) \tag{50}$$

The final form of the momentum equation is:

$$\frac{\partial Q}{\partial t} + \frac{\partial (QU)}{\partial x} + g A \left(\frac{\partial z}{\partial x} + S_f \right) = 0 \tag{51}$$

When the continuity equation (Eq. 23) and the momentum equation (Eq. 51) are applied to one-dimensional unsteady flow in HEC-RAS, there is an interaction between the main channel and the floodplain flows. One possible approximation in

one-dimensional modeling is to represent the floodplain flow as a distinct channel. In other words, the system is divided into two different channels and the continuity and momentum equations are applied to each channel separately. Hence, the discharge is distributed according to conveyance:

$$Q_c = \phi Q \tag{52}$$

In which

Q_c: flow in channel (m³/s);

Q: total flow (channel and floodplain) (m³/s).

The term ϕ describes how the flow is divided between the channel and the floodplain and it is related to the conveyance:

$$\phi = \frac{K_c}{K_c + K_f} \tag{53}$$

In which

ϕ: conveyance relation;

K_c: conveyance in channel;

K_f: conveyance in floodplain.

Thus, the Eq. 23 and Eq. 51 can be modified to the system of partial differential equations:

$$\frac{\partial A}{\partial t} + \frac{\partial \phi Q}{\partial x_c} + \frac{\partial [(1-\phi)Q]}{\partial x_f} = 0 \tag{54}$$

$$\frac{\partial Q}{\partial t} + \frac{\partial}{\partial x_c}\left(\frac{\phi^2 Q^2}{A_c}\right) + \frac{\partial}{\partial x_f}\left(\frac{(1-\phi)^2 Q^2}{A_f}\right) + gA_c\left(\frac{\partial z}{\partial x_c} + S_{fc}\right) + gA_f\left(\frac{\partial z}{\partial x_f} + S_{ff}\right) = 0 \tag{55}$$

The Eq. 54 and the Eq. 55 are known as the Saint-Venant equations, with discharge (Q) as a dependent variable. For unsteady flows, where the flow changes temporally, the St. Venant equations are used to describe dynamic water movement

for rivers and streams. These equations are a result of taking mass and momentum balances on a one-dimensional channel (CHAPRA, 1997; BRUNNER, 2016b).

Its principal aspect is the adequate representation of the longitudinal flow closer to reality. It is important to notice that the HEC-RAS unsteady flow module combines the left and right overbank into a single flow called floodplain. The mass conservation equation represents the hydrographs damping effects, which occur due to variation of storage capacity. The expression for momentum conservation, in turn, considers the balance of forces acting on the mass of water, which includes gravity, friction, pressure and inertia of the flow. It is common to apply the Saint-Venant equations to represent one-dimensional problems in channels, such as discharge routing, flood prediction, dam ruptures, and surface and subsurface runoff (BRUNNER, 2016b; FERREIRA; FERNANDES; GOMES, 2017)

The partial differential equations can be solved numerically by approximating each with a finite-difference algebraic equation, then the system of algebraic equations is solved in conformance with the initial and boundary conditions. Finite difference methods, explicit or implicit, are the most common procedures for one-dimensional problems. In general, they are simple for computational implementation and generate results quickly. The explicit method and implicit method are numerical analysis methods used to solve a time-dependent differential equation (CHAPRA, 1997; BRUNNER, 2016b; FERREIRA; FERNANDES; GOMES, 2017; JI, 2017).

The explicit method calculates the system status at a future time from the current known system status. The implicit method calculates the system status at a future time from the system statuses at present and future times. In a generic equation $y = f(x, t)$, the explicit method solves it as:

$$y_{n+1} = y_n + hf(y_n, t_n) \tag{56}$$

An explicit solution results from a method that is independent of other values (for the same level). A single equation is used to evaluate new nodal variables for a single time step. If you know the state at "n", you can calculate the state at "$n + 1$".

The implicit method has the state at "$n + 1$" on the right-hand side as in:

$$y_{n+1} = y_n + hf(y_{n+1}, t_{n+1}) \tag{57}$$

In both cases, h (θ) is the time step.

An implicit solution contains information obtained from solving simultaneous equations for the full grid for each time step. This is computationally more demanding, but allows for larger time steps and better stability.

The explicit method is easier to program and can be calculated within a shorter time, but its stability is so low that you need to use a step size small enough to prevent divergence. On the contrary, the implicit method has high stability and converges if you set proper parameters, but, as you need to solve an equation at every step, it takes a long time to calculate. As the implicit method can use a sufficiently large step size, it is suitable for solving equations that involve a long time. Explicit method requires impractically small time steps.

Basically, in an explicit scheme, there is a simple updating procedure that does not depend upon other values at the current level while an implicit one contains information at the current level which requires the solving of simultaneous equations.

The main pros and cons of these two methods are that explicit schemes are easy to program with only simple calculations performed at each time step while implicit schemes are more difficult and can involve many iterations per time step. Explicit schemes, however, have a tendency to be unstable and require small time steps while implicit schemes are more stable and can have larger time steps.

In HEC-RAS, the one-dimensional unsteady flow Saint Venant equations are solved using the four-point implicit scheme, also known as the box scheme or Preissmman Scheme. Figure 16 illustrates a typical finite difference cell in HEC-RAS. The simultaneous solution is an important aspect of this scheme because it allows data from the entire reach to influence the solution at any one point.

Figure 16 – Typical finite difference cell in HEC-RAS

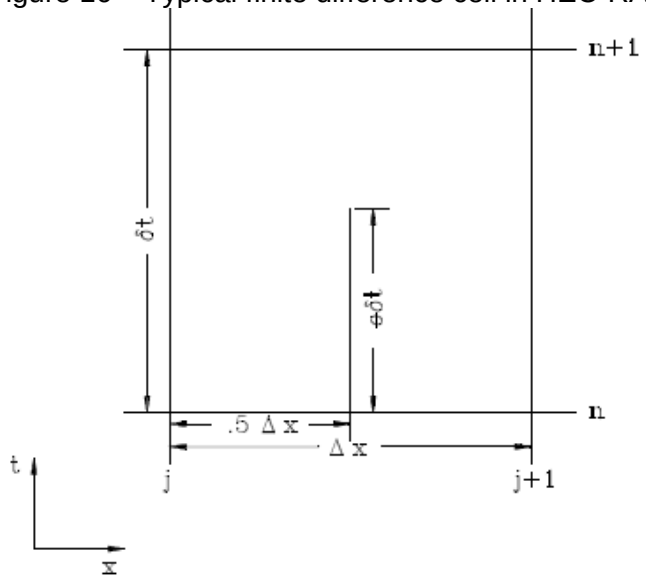

Source: Brunner (2016b).

In HEC-RAS, the general implicit finite difference forms are the time derivate (Eq. 58) and the space derivate (Eq. 59):

$$\frac{\partial f}{\partial t} \approx \frac{\Delta f}{\Delta t} = \frac{0{,}5\left(\Delta f_{j+1} - \Delta f_j\right)}{\Delta t} \tag{58}$$

$$\frac{\partial f}{\partial x} \approx \frac{\Delta f}{\Delta x} = \frac{\left(f_{j+1} - f_j\right) + \theta\left(\Delta f_{j+1} - \Delta f_j\right)}{\Delta x} \tag{59}$$

Theoretically, θ can vary from 0.5 to 1.0. However a practical limit is from 0.6 to 1.0. Adjusting the θ weighting factor can improve model stability or increase the accuracy of the output. Increasing this value towards 1.0 will increase model stability, decreasing this value towards 0.6 will increase model accuracy.

Considering the continuity equation (Eq. 23) with the addition of a storage term (S), it can be approximated using implicit differences method applying Eq. 58 and Eq. 59:

$$\Delta Q + \frac{\Delta A_c}{\Delta t}\Delta x_c + \frac{\Delta A_f}{\Delta t}\Delta x_f + \frac{\Delta S}{\Delta t}\Delta x_f - \overline{Q_l} = 0 \tag{60}$$

In which

$\overline{Q_l}$: average lateral inflow (m³/s);

S: storage from non-conveying portions of cross section (m³);

Δx_c: length of the main channel between two cross sections (m);

Δx_f: length of the floodplain between two cross sections (m).

Considering the momentum equation (Eq. 51), it can be approximated using implicit differences method applying Eq. 58 and Eq. 59:

$$\frac{\Delta(Q_c \Delta x_c + Q_f \Delta x_f)}{\Delta t \Delta x_e} + \frac{\Delta(\beta U Q)}{\Delta x_e} + g\bar{A}\left(\frac{\Delta z}{\Delta x_e} + \bar{S_f}\right) = 0 \quad (61)$$

In which

Δx_e: equivalent flow path (m);

β: velocity distribution factor.

In HEC-RAS, Upstream boundary conditions are required at the upstream end of all reaches that are not linked with other reaches or storage areas. In that case, an upstream boundary condition is necessarily as a flow hydrograph, stage hydrograph or flow-stage rating curve. Downstream boundary conditions are required at the downstream ends of all reaches that are not connected to other reaches or storage areas. It can be a Stage Hydrograph, a Flow Hydrograph, a Rating Curve or a Normal Depth. Boundary conditions can also be applied to internal location in the water system, such as Lateral Inflow Hydrographs and Uniform Lateral Inflow Hydrographs. Those hydraulic controls are frequently used to force the model to perform all regular natural conditions for an estuary as floods and tides.

2.6.2 Water Quality Simulation

Advection and dispersion are the most significant processes in which a dissolved material is transported in a river or estuary. Longitudinal transport of a constituent is the combination of the advective component and the dispersive component.

Advection is related to the horizontal transport by flow, in which the material is moved, but it is not significantly distorted or diluted. In rivers and estuaries, it is commonly the principal transport process of constituents in the longitudinal direction. The velocity profiles indicate that the maximum advection occurs in the middle of the channel, and the minimum advection occurs on its banks.

Dispersion, on its turn, is the horizontal mixing process mainly provoked by turbulent mixing in rivers and estuaries. It is not only related to exchange of water masses, but also of dissolved substances, such as salts and dissolved pollutants. In mathematical modeling, the most common type of dispersion model is based on the concept of diffusion, in which dispersion is related to all forcing conditions, simplifying the process of problem solving.

Dispersion in the direction of the flow is called longitudinal dispersion, which is one of the most important processes in rivers and estuaries, where the larger the longitudinal dispersion, the slower salinity decreases in upstream direction. Longitudinal dispersion depends on the longitudinal dispersion coefficient (D_x) and the simplest approach is to consider a totally well mixed and uniform flow river to accept D as a constant. However, just in few estuarine rivers this approach would be applied. The values of D_x are generally between 10m²/s and 5000m²/s, depending on the forcing conditions of the water body and can be calculated as (UNESCO, 1991; SAVENIJE, 2012; JI, 2017):

$$D_x = 0{,}011 \frac{U^2 B^2}{H U_*} \tag{62}$$

In which

D_x: longitudinal dispersion coefficient (m²/s);

B: average channel width (m);

H: average channel depth (m);

U_*: shear velocity (m/s).

Shear velocity can be calculated as:

$$U_* = \sqrt{gHS_f} \tag{63}$$

Based on the principle of conservation of mass, the HEC-RAS Water Quality Module solves for each water quality constituent the one-dimensional advection-dispersion equation, which indicates the net changes of constituents in water:

$$\frac{\partial(VC)}{\partial t} = \underbrace{-\frac{\partial(QC)}{\partial x}\Delta x}_{advective\ term} \underbrace{+\frac{\partial}{\partial x}\left(AD_x\frac{\partial C}{\partial x}\right)\Delta x}_{dispersion\ term} \pm S \tag{64}$$

In which

V: volume of the water quality cell (m³);

C: constituent concentration (g/m³);

Q: flow (m³/s);

S: sources and sinks.

The first term in the right side of Eq. 63 is the advective term. It accounts for the mass inputs and outputs by water current and specifies the movement of the constituent with water as it flows downstream or upstream. The second term is the dispersion term. It describes the spreading of the constituent that occurs due to turbulent mixing. The third term is the source and sink term, which is related to the particle settling, biochemical reactions and external loads (CHAPRA, 1997; ZHANG; JOHNSON, 2014; JI, 2017).

HEC-RAS solves the Eq. 63 for each water quality cell and for each constituent using the QUICKEST-ULTIMATE explicit numerical scheme. The resultant finite-difference solution is (LEONARD, 1991; ZHANG; JOHNSON, 2014):

$$V^{n+1}C^{n+1} = V^nC^n + \Delta t\left(Q_{up}C^*_{up} - Q_{dn}C^*_{up} + D_{dn}A_{dn}\frac{\partial C^*}{\partial x_{dn}} - D_{up}A_{up}\frac{\partial C^*}{\partial x_{up}}\right) + \Delta tSS \tag{65}$$

In which

C^{n+1}: concentration at present time step (g/m³);

C^n: concentration at previous time step (g/m³);

C_{up}^{*}: QUICKEST concentration at upstream face (g/m³);

$\frac{\partial C^{*}}{\partial x_{up}}$: QUICKEST derivative at upstream face (g/m^4);

D_{up}: upstream face dispersion coefficient (m²/s);

V^{n+1}: volume of the water quality cell at present time step (m³);

V^{n}: volume of the water quality cell at previous time step (m³);

Q_{up}: upstream face flow (m³/s);

A_{up}: upstream face cross section area (m²);

SS: total source and sink terms (g/m³/s).

The subscript dn indicates the downstream face.

The Eq. 65 demands two boundary conditions, at upstream and downstream sections. It is usual to extend the simulation reach to upstream in order to feed the model with known values of lower constant salinity, for example 0.5 g/kg up to 1.0 g/kg. For downstream boundary condition, an observed concentration time series can be used or a relationship between freshwater flow and tide movement.

3 STUDY AREA

Cubatão is a city in the State of São Paulo, Brazil, 12 kilometers away from Santos. It is part of the Metropolitan Region of Baixada Santista. The population is estimated at 128,749 (2017) in an area of 142.88 km² (IBGE, 2017). Cubatão River is part of the Santos estuarine system and it divides the Cubatão into two different environments; its urban reach has approximately 11.4 km. On its left bank, there is a great amount of industries such as oil refinery, petrochemical industry and processing industry; and on its right bank, there is a consolidated urban area (FCTH, 2017). Figure 17 illustrates the Santos estuarine system and Cubatão.

Figure 17 – Santos estuarine system.

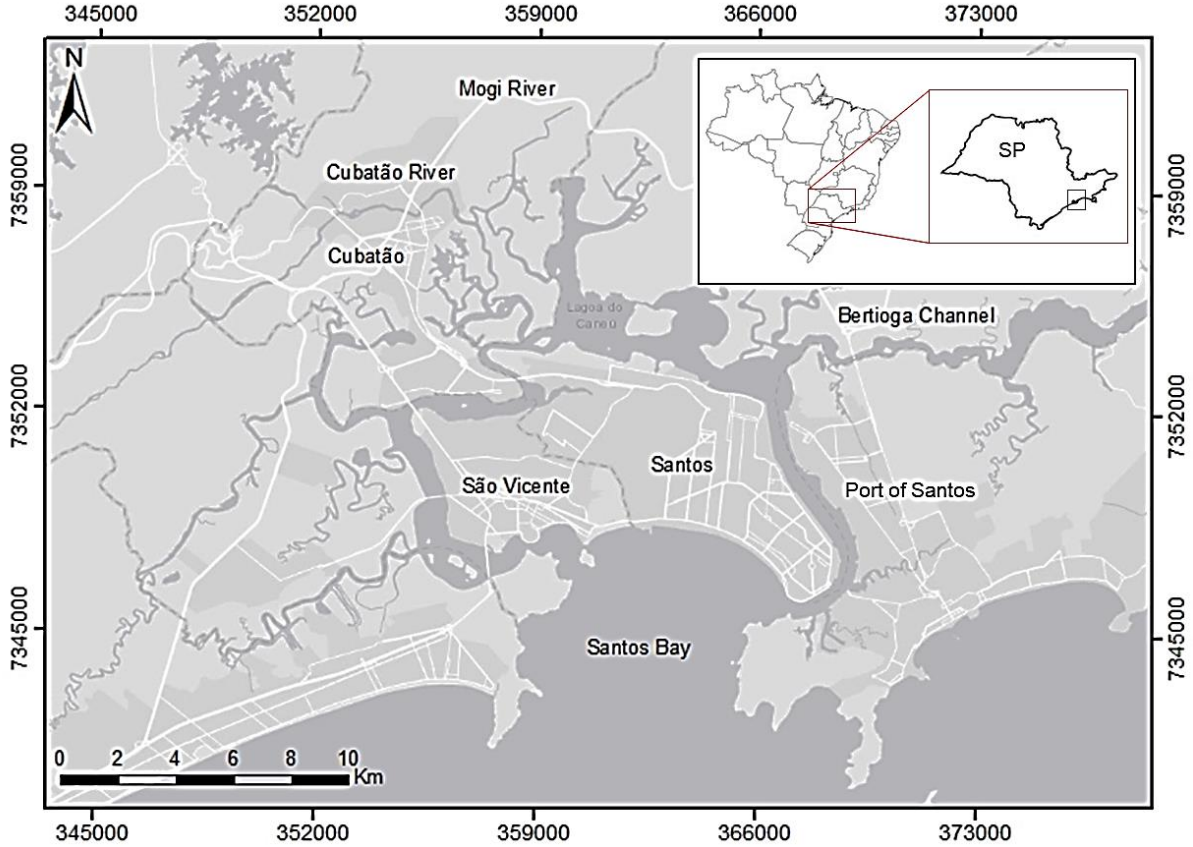

The climate in Cubatão is Tropical, with some local variations due to topographic characteristics: near Serra do Mar foothill, a coastal mountain range, there is a more intense precipitation compared to the lowlands. There are a significant rainfall during the year; even during dry periods, there are considerable rain events. The average annual rainfall is 2,541mm, with higher precipitation events

during the wet period, mainly from June to August; and less precipitation events during the dry period, mainly from January to March. Thus, this seasonal variation has a direct effect on the rivers regimes in Cubatão, in which the rivers can reach high discharges during significant precipitation events. Considering that these rivers are located in the Santos estuarine system, the tidal activity also plays a significant role in the discharge variation during the year. The principal river basins in Cubatão are: Cubatão River basin (177 km²), Mogi River basin (68 km²), and Perequê River basin (64 km²) (FCTH, 2017).

The Cubatão industrial area is one of the most important economic regions in the country, hosting industries, refining oil, steel mills and fertilizers. From 1955 to 1975, Cubatão experienced an intense industrial growth, in which many important industries started their activities. In 1955, for example, the Presidente Bernardes Petrobras Refinery was installed and the Companhia Siderúrgica Paulista (Cosipa), now called Usiminas, was installed in 1959. Eighteen from twenty four industries that belong to the industrial complex of Cubatão were inaugurated from 1955 to 1975. This industrial and population growth led to an increasing natural resources demand and, consequently, higher water consumption and higher water resources management concerns (GUTBERLET, 1996; PINTO, 2005; COUTO, 2012).

The Cubatão River is the most important river in the region because it is the source of water for several industries and for urban consumption; it is also the final destination of industrial and urban wastewater. It springs in São Bernardo do Campo, on Serra do Mar, but the main reach is practically at the sea level until it enters the Santos Bay. It is affected by Perequê River basin and after there is a confluence with Mogi River (Figure 18) (PINTO, 2005; FCTH, 2017).

Figure 18 – Rivers Cubatão, Perequê and Mogi; and important points at the upstream reach of Cubatão River.

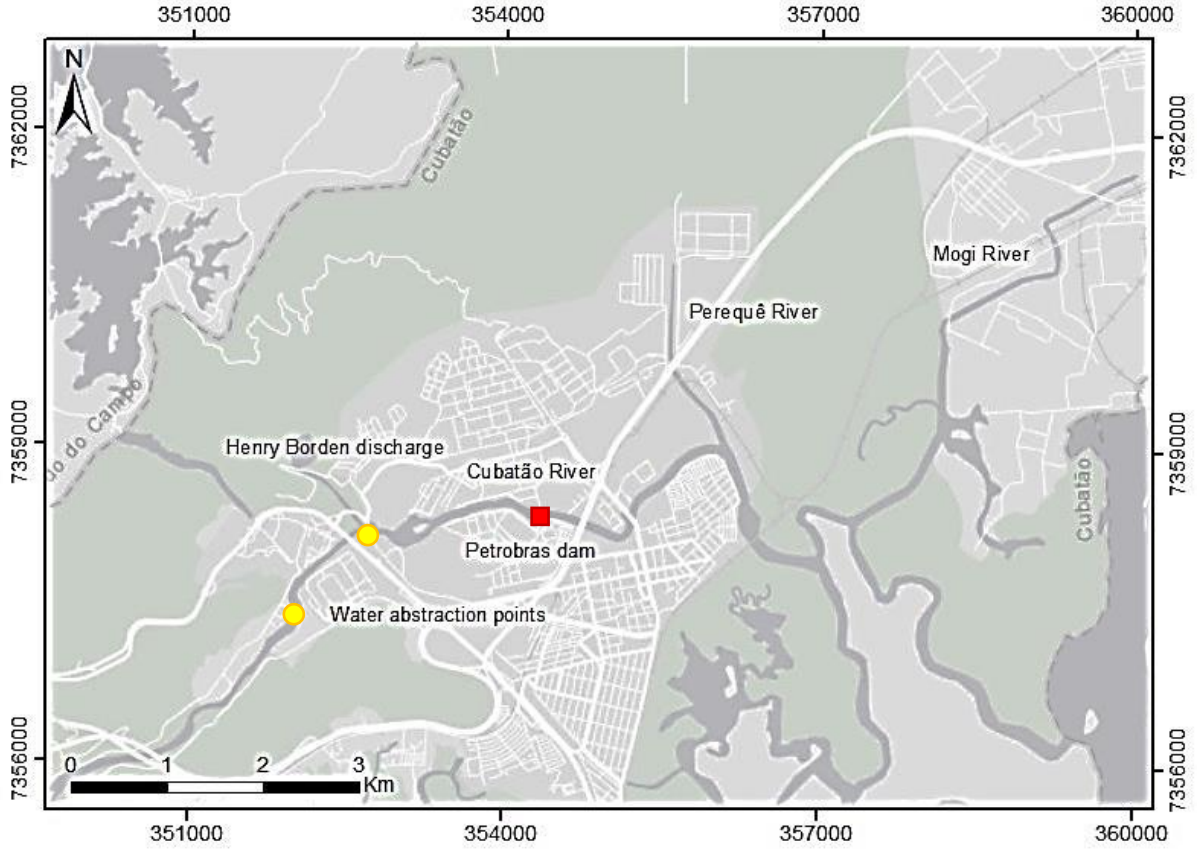

In Cubatão River, the water abstraction is for different purposes, such as urban water supply and significant industrial uses, with special consideration for the Companhia de Saneamento Básico do Estado de São Paulo (SABESP) water abstraction, for urban consumption; and the Presidente Bernardes Petrobras refinery, with a major industrial water consumption (Figure 18) (COUTO, 2012; FCTH, 2017).

An important aspect of Cubatão River water management is the Henry Borden Hydroelectric Power Plant (HB), operated by Empresa Metropolitana de Águas e Energia SA (EMAE). It is located on the foot of Serra do Mar, with two high head (720m) power plants equipped with 14 groups of generators, totaling an installed capacity of 889 MW, for a flow rate of 157.0m³/s. The water used by the power plant was actually diverted from Tietê and Pinheiros Rivers, located in the highlands, stored in intermediate reservoirs and driven to the estuary by pipelines. However, since 1992, the operation of this system is considerably reduced due to the water quality problems found in the contributing rivers mentioned. In fact the reversion can only be done during flood events. This operational limitation decreased by

approximately 75% the energy produced in the facility and, consequently, its discharge to Cubatão River. Nowadays, only 6.0m³/s are conveyed from HB to keep a minimum operational flow. HB water discharges are of major importance for water management in Cubatão River, because it has an impact on water quality parameters and salinity concentration along the urban and industrial reach of the river (COUTO, 2012; GONÇALVES, 2013). The SABESP water abstraction points for urban consumption, the HB discharge channel and the Petrobras dam are illustrated in Figure 18.

4 MATERIALS AND METHODS

This section is structured in three subsections: the description of the EC sensor assembling, calibration and validation methods (4.1); the field surveys periods and measurements procedures (4.2); and the numerical model setup, calibration and validation methods (4.3).

4.1 SALINITY SENSOR ASSEMBLING, CALIBRATION AND VALIDATION

4.1.1 Sensor design, housing and power supply

The electronic circuit for EC measurements was based on the SMX electrical interface for moisture sensors developed by EME Systems (EME SYSTEMS, 2018). An Arduino board combined with Arduino modules were used to execute the written code, read data/time, temperature and frequency measurements and record it on a microSD card.

It was used an Arduino Pro Mini (5V model), a board based on the ATmega328 microcontroller. It works in a recommended input voltage of 5V - 12V (maximum 16V), has 14 digital input/output pins, 6 analog inputs, a 16 MHz resonator and a reset button. Its six pin header can be connected to a serial converter adapter cable to provide USB communication to the board. The Arduino Pro Mini was selected for its low-cost and small size characteristics.

The Arduino Pro Mini was connected to a Real Time Clock (RTC) DS3231 module for timing purposes and to a microSD card reader module for data recording. Temperature was measured with a 1-wire interface DS18B20 digital thermometer (11 bits) with a precision of 0.125ºC. It has an accuracy of $\pm$ 0.5ºC from 10ºC to 85ºC with a measurement range from -55ºC to 125ºC. It can be powered from 3V to 5.5V and works easily with any Arduino board. Date and time, temperature, frequency signals (for further conversion into EC) and battery voltage were saved on the microSD card as comma-separated values files (.csv).

The sensor was configured to operate in the sleeping-mode function in order to reduce energy consumption and it was also used an IRF 520 transistor to shut down the system when it is not acquiring and saving monitoring data. An IFR 520 is a Metal

Oxide Semiconductor Field Effect Transistor (MOSFET), which works controlling the current flow by voltage variation, frequently used with microcontrollers like Arduino for switching current loads. When the sensor goes to sleep mode, it is also crucial to have the lowest power consumption as possible, so the MOSFET works as a switch that cuts the power from the sensor when the Arduino Pro Mini sleeps.

A 555 Timer Integrated Circuit (IC) in its 8-pin Dual in-line package (DIP) configuration was used for EC measurements. It was used the LMC555 IC version, set in astable mode as a pulse generator to create a square wave AC signal. By applying an AC voltage between metal electrodes, it results in an output pulse as a square-wave, which will be used as an input reading of the EC sensor. It is also mandatory that an AC voltage is applied between metal electrodes because DC currents form an oxide layer on the metal cathode surface and the electrode will corrode, affecting data acquisition. In this sensor, stainless steel screws were used as metal electrodes for EC measurements.

A major obstacle was to build an effective waterproof housing for the electronic devices and this issue is even more complicated for electrical conductivity (EC) sensors, which must have an external probe in direct contact with water, being necessary not only a waterproof housing, but also a seal between the probe external face and the internal electronic components (LOCKRIDGE et al., 2016).

The electronic components were enclosed in a 30 cm piece of 50mm rigid PVC pipe, with a cap in each of its ends. The components were accessed by a PVC threaded union, in the middle of the PVC pipe. This access is necessary for data acquisition from the microSD card and to change batteries. The EC probes were in contact with the external environment through two holes accurately drilled in the cap. Table 8 summarizes the materials and their functions in the sensors assembling.

Table 8 – Electronic components used in the proposed salinity sensor.

Component	Function
Arduino Pro Mini	Execute the written code, read and save the acquired data.
Real Time Clock (RTC) DS3231	Data and time
DS18B20 digital thermometer	Temperature measurement
MicroSD card reader module	Saves acquired data on the microSD
MicroSD card	Store the acquired data.
IRF 520 MOSFET	System's shutdown
LMC555 IC	Pulse generator to create a square wave AC signal for further EC measurement
Resistors	Set a minimum and maximum frequency allowed; pull-up resistors.
Capacitors	Decoupling capacitors, coupling capacitors, galvanic isolation.
Stainless steel screws	Metal electrodes for EC measurements
50mm PVC pipe and caps	Electronic circuit housing
PVC threaded union	Access to the electronic circuit

Waterproof and battery lifetime tests were conducted at the Hydraulics Laboratory at University of São Paulo, Brazil, along May, 2019.

4.1.2 Calibration and Validation methods

In order to calibrate the sensor, converting the frequency reading into EC, solutions with known EC values were used, which were correlated with the corresponding frequency. Potassium Chloride (KCl) was dissolved in deionized water to provide a solution with known EC values, which were measured by a HOBO U24-002-C Water Conductivity Data Logger with a low range from 100 to 10.000 μS/cm and a high range from 5.000 to 55.000 μS/cm, over the range of 5°C to 35°C. The salinity accuracy is 5% of the reading and the temperature accuracy is 0.1°C (ONSET, 2019). Frequency measurements were taken at an approximately constant temperature of 23°C as follows: one frequency reading per minute, during ten minutes, and the average frequency was established as the corresponding frequency

for the EC measurement at 23°C. Calibration was made by plotting the measured frequency against known EC values for the standard calibration temperature.

Eq. 2 describes the calibrated conductivity equation, a general linear equation for temperature variation effects in EC measurements. Based on temperature compensation factor A values for different water conditions, Hayashi (2004) suggested a common 0.0187 A value for a temperature range of 0°C-30°C. For the proposed EC sensor, Eq. 66 adjusts the general Eq. 2:

$$\sigma_0 = \frac{\sigma_{23°C}}{1+1.87\%(23-T_0)} \tag{66}$$

After laboratory calibration tests, validation tests were conducted during six days, from 25 April 2019 to 01 May 2019, in Cubatão River, Brazil, 12 kilometers away from Port of Santos, at P1 (Figure 20). This estuarine river is affected by salinity intrusion due to tidal activity and presents suitable salinity range for sensor application. The acquired data were compared to the temperature and salinity data from the industrial sensor HOBO U24-002-C Water Conductivity Data Logger. This temperature and salinity accuracy is in consonance with others water quality sensor applied in recent researches in estuarine environments (YU et al., 2014; HADDOUT et al., 2016, ABDULLAH et al., 2016, LOCKRIDGE et al., 2016)

Salinity is calculated using the dimensionless Practical Salinity Scale 1978 (PSS-78) (IOC; SCOR; IAPSO, 2010), which depends on temperature and pressure values (Eq. 3 to Eq. 7).

The statistical analyses were delivered in order to evaluate the performance of the sensor compared to the reference salinity value (industrial sensor). Root mean square error (RMSE) were calculated for temperature and salinity validation and the coefficient of determination (R^2) and Nash-Sutcliffe efficiency index (EF) were also taken as criteria for salinity validation.

The RMSE between the reference value and the measured value is determined by Eq. 67. It measures the size of error in percentage terms.

$$RMSE = \sqrt{\frac{1}{n}\sum (O - S)^2} \quad (67)$$

In which

n: number of observation-simulation pairs;

O: observed value;

S: simulated value.

The coefficient of determination (R^2), which illustrates how many data points fall within the results of the line formed by the regression equation, can be determined by Eq. 68.

$$R = \frac{n\left(\sum OS\right) - \left(\sum O\right)\left(\sum S\right)}{\sqrt{\left[n\sum O^2 - \left(\sum O\right)^2\right]\left[n\sum S^2 - \left(\sum S\right)^2\right]}} \quad (68)$$

In which

R: correlation coefficient.

Another statistical indicator used for evaluate the performance was the EF defined by Eq. 69.

$$EF = 1 - \left[\frac{\sum_{i=1}^{n}(O - S)^2}{\sum_{i=1}^{n}\left(O - \overline{O}\right)^2}\right] \quad (69)$$

In which

$\overline{O}$: mean observed value.

The EF can vary from $-\infty$ to 1 (inclusive). The closer the EF efficiency to 1, the more accurate is the performance. Values ≥0.75 are considered good levels of

performance; between 0.36 and 0.75 are considered acceptable, while values ≤0.36 indicate an unacceptable performance (HADDOUT, et al., 2016).

4.2 ENVIRONMENTAL MONITORING: PRIMARY AND SECONDARY DATA

Field surveys were conducted in two different periods for primary environmental data acquisitions. The first field survey was conducted for approximately four months, from 03/11/2016 to 04/03/2017 and the data acquired were salinity, water temperature, water level and precipitation; the second field survey was conducted for approximately two weeks, from 14/05/2019 to 30/05/2019 and the acquired data were salinity and water temperature.

Secondary data acquired were:

a) Tidal elevation at Port of Santos (Torre Grande);
b) Rio Cubatão upstream water level;
c) Precipitation at Cubatão;
d) Water level at COSIPA;
e) HB water discharge.

The astronomical tidal elevation was obtained from a tide table for the Port of Santos, in Torre Grande (23.949°S, 46.308°W), approximately 13km from the confluence of Cubatão and Mogi River, computed upon 45 tidal harmonic constituents (BRASIL, 2019). The tidal regime on the coast of Santos is semi-diurnal with diurnal inequity, having two high tides and two low tides at approximately 6 hours interval. The time series of the astronomical tidal level was calculated based on the 45 tidal harmonic constituents. Figure 19 illustrates the astronomical sea level time series at Torre Grande tidal station for three months and for one week during spring tide.

Figure 19 – Astronomical sea level time series from the tidal harmonic constituents. (a) Three months. (b) One week during spring tide.

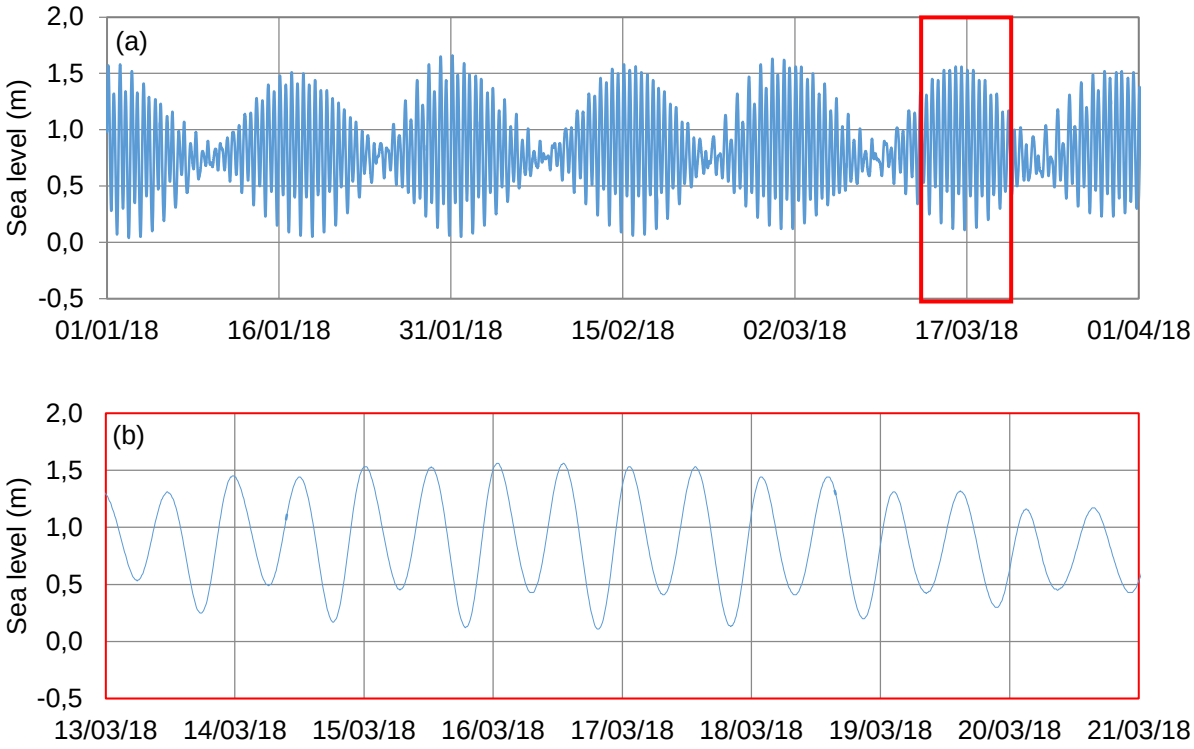

Rio Cubatão upstream water level, precipitation and water level at COSIPA were taken from Sistema de Alerta a Inundações de São Paulo (SAISP), a vast network of monitoring stations operated by the Hydraulic Laboratory (SAISP, 2019). The water level taken at COSIPA Station was used to determine the Cubatão River downstream edge water level through a linear correlation occurred along the second field survey. Table 9 summarizes the primary and secondary data and their sources, and Figure 20 illustrates their location on the map.

Table 9 – Acquired data during field surveys.

Primary data	First survey	Salinity
		Water temperature
		Rio Cubatão downstream water level
	Second survey	Salinity
		Water temperature
Secondary data		Tidal elevation (Torre Grande – Marinha do Brasil)
		Rio Cubatão upstream water level (SAISP)
		COSIPA water level (SAISP)
		Precipitation (SAISP)
		HB water discharge (EMAE)

Figure 20 – Map location of primary and secondary data.

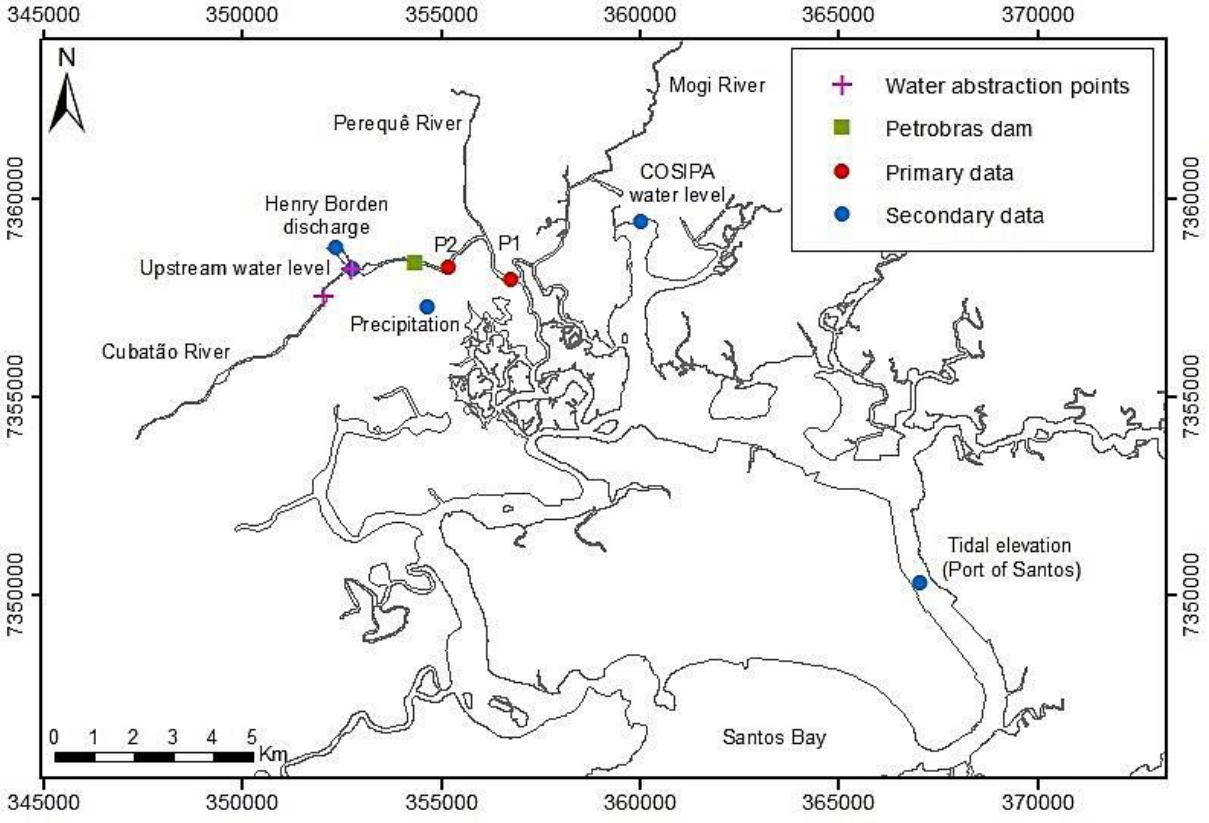

4.2.1 First Field Survey (03/11/2016-04/03/2017)

The first field survey was conducted for approximately four months, from 03/11/2016 to 04/03/2017. During this period, the primary monitoring parameters were:

a) Salinity Concentration;
b) Water temperature;
c) Water Level;

The salinity concentration, water temperature and water level were measured in one monitoring station (P1) in Cubatão River (Figure 20), located upstream the confluence of Cubatão River and Mogi River (Figure 21).

Figure 21 – Monitoring Point P1.

At P1, the monitoring parameters were measured every ten minutes using the EC meter HOBO Salt Water Salinity Data Logger - U24-002-C in three different depths in the water column:

a) Near the surface. Approximately 0.5 m below the surface;
b) In the middle. Approximately 3.0 m below the surface;

c) Near the bottom of the river. Approximately 4.5 m below the surface.

The water level was measured at P1 every 10 minutes using the HOBO Water Level Logger - U20L-01 (Operational Range 0 to 9 m of water depth at sea level. Maximum error ± 2 cm of water). Since the equipment works with the difference in pressure, it was necessary to install one equipment in the bottom of the river and one at the atmospheric pressure.

4.2.2 Second Field Survey (14/05/2019-30/05/2019)

The second field survey was conducted for approximately two weeks, from 14/05/2019 to 30/05/2019. During this period, the primary monitoring parameters were:

a) Salinity Concentration;
b) Water temperature.

Vertical profiles of salinity and temperature were measured in two monitoring stations along the Cubatão River – P1 and P2 (Figure 20). P1 is the same as the first field survey and P2 was located upstream the confluence of Cubatão River and Perequê River, approximately 2.5 km upstream P1 (Figure 22).

Figure 22 – Monitoring station P2.

At P1 and P2, salinity and water temperature were measured every minute using our purposed EC sensor in three different depths in the water column:

a) Near the surface. Approximately 0.5 m below the surface;
b) In the middle. Approximately 3.0 m below the surface;
c) Near the bottom of the river. Approximately 4.5 m below the surface.

Local water level at P1 was not measured directly during the second field survey; it was determined indirectly using the mentioned correlation built after the data taken in the first survey.

The stratification pattern of each monitoring station was studied by determining their stratification parameter (Eq. 1). The salinity stratification patterns in the water column were also associated with observed forcing mechanisms, such as the river flow, HB discharge, tides and precipitation events.

4.3 MODEL SETUP AND SIMULATED SCENARIOS

The hydrodynamic and water quality model adopted in this study to simulate seawater intrusion in Cubatão River under different forcing conditions was the 1D HEC-RAS in its version 5.0.5. The modeling domain covers the urban reach of Cubatão River, Perequê River and Mogi River.

Model topography was taken from a previous study carried out by the Hydraulic Laboratory in Cubatão River, using planimetric and altimetric data and photogrammetric survey in order to create contour lines and use them in hydrodynamic and water quality models (FCTH, 2017). The data were collected from different sources, such as bathymetric cross section survey, photogrammetric survey (1997); cartographic maps (scale 1:10.000) from Empresa Paulistana de Planejamento Metropolitano (EMPLASA); and Topographic maps from IBGE. The data were combined to compose a Digital Elevation Model (DEM) and then used to create the geometric data HEC-RAS 5.0.5 model.

4.3.1 Boundary forcing conditions

Considering that the available topography data was only for the rivers reaches, it would be challenging to perform hydrodynamic and water quality modeling in an estuarine environment with this limitation, since in most cases the downstream boundary condition is the open sea with a constant salinity concentration value. An idealized estuary was applied downstream the final reach of Cubatão River to represent the Santos Estuary, so it was possible to set the astronomical tidal elevation and the constant salinity concentration as downstream boundary conditions. The hydrodynamic model is forced by tides in the downstream boundary condition and by river inflows in the upstream boundary conditions. The hydroelectric power plant discharge was set as a lateral boundary condition in Cubatão River. In the model setup, the open boundaries conditions were (Figure 23):

a) Flow Hydrographs at the head of each river (Cubatão, Perequê and Mogi);
b) A Lateral Inflow, representing the HB water discharge in Cubatão River;
c) A Stage Hydrograph as the open sea boundary at the idealized estuary mouth, 30km downstream the confluence of Cubatão and Mogi rivers, representing the Santos Bay.

Figure 23 – Open boundary conditions.

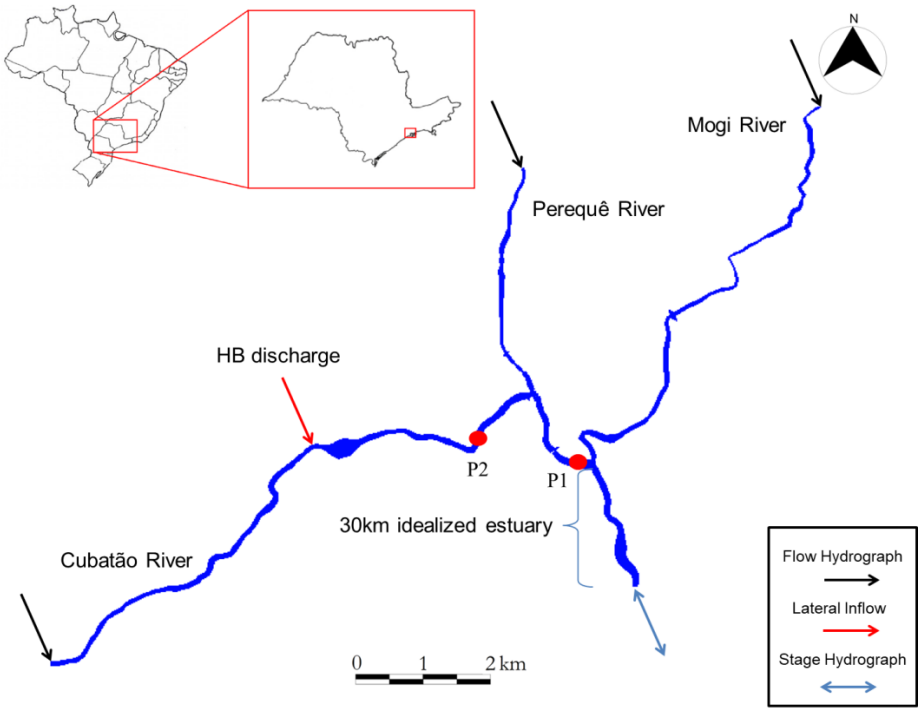

River flows and tides values were determined based on water level data acquired during the monitoring periods.

4.3.2 Model calibration and validation procedures

A set of observed data collected in May 2019 was used to calibrate the hydrodynamic and the water quality models. As the Manning Coefficient (n) strongly influences the tidal propagation, the hydrodynamic model calibration was carried out by adjusting this coefficient for each river reach. Water surface elevation data at P1 was used to calibrate the hydrodynamic model. The longitudinal dispersion coefficient (D_x) is the key calibration parameter of the water quality module, so salinity concentration data at P1 and P2 were used to calibrate the water quality model by adjusting D_x for each river reach (UNESCO, 1991; ETEMAD-SHAHIDI et al., 2015; JI, 2017; WANG et al., 2019).

For calibration procedures, a constant water discharge was applied at each river upstream boundary and the salinity concentration was null for all water quality cells. The downstream boundary was forced by astronomical tides from Torre Grande tide station (Figure 24) and a constant salinity concentration set to 32.0 g/kg, a typical value for Santos Bay, in which salinity can vary from 29g/kg to 35g/kg (ROVERSI, 2012).

Figure 24 – Astronomical tides forcing the downstream boundary during the calibration procedure.

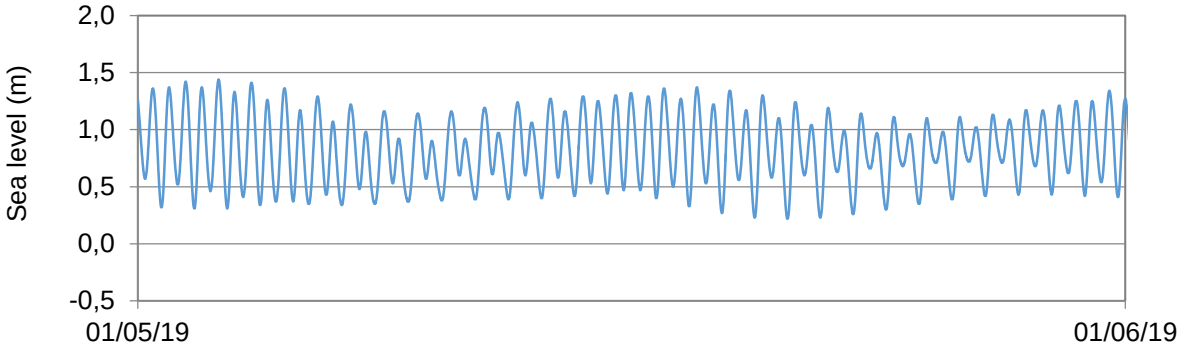

A seven days spinout time was applied to flush the initial conditions out the model. The calibration procedure was performed by comparing the simulated data

with the observed data in the same period. Table 10 shows the forcing and initial conditions at each boundary for calibration procedures.

Table 10 – Boundary forcing and initial conditions.

Boundary		Hydrodynamic model	WQ model (salinity)
Upstream boundary	Cubatão River	10 m³/s	Null
	Perequê River	4m³/s	Null
	Mogi River	6m³/s	Null
Lateral boundary	HB discharge	6m³/s	Null
Downstream boundary	Idealized estuary mouth	Predicted water surface elevation (Torre Grande tide station)	32 g/kg

A set of observed data collected in November 2016 at P1 station was used for hydrodynamic and water quality validation procedures, in which observed data was compared to simulated data. For both water quality calibration and validation procedures, it was used the mean salinity based on the observed data at P1 and P2 during the field surveys.

For both calibration and validation procedures, the model was assessed using the Skill Model:

$$skill = 1 - \frac{\sum_{i=1}^{n} |S - O|^2}{\sum_{i=1}^{n} \left(|S - \overline{O}| + |O - \overline{O}| \right)^2} \quad (70)$$

A skill value of 1.0 indicates a perfect performance of the model, excellent for skill between 0.65 and 1.0, very good for skill in a range of 0.5 to 0.65, good for skill in the range of 0.2 to 0.5 and poor for skill less than 0.2 (CHEN et al., 2016; JI, 2017; VARGAS; VAZ; DIAS, 2017; WANG et al., 2019).

4.3.3 Simulated Scenarios

After calibration and validation procedures, the model was able to simulate 1D seawater intrusion behavior under different forcing conditions for river discharge and tidal elevation. The above mentioned model is set as the reference model, and then used to examine the seawater intrusion scenarios.

The simulated scenarios were defined based on the two most important forcing factors in an estuarine river: river discharge and tides. The scenarios were investigated in two approaches:

a) The maximum seawater intrusion length in Cubatão River in the reference scenario (normal flow – 16m³/s), during dry season (low flow – 8m³/s) and wet season (high flow – 40m³/s) during spring and neap tide.
b) The SLR impacts on the maximum seawater intrusion length in Cubatão River considering different flows. The SLR considered were ΔH=0.25m, 0.5m and 1.0m and the Cubatão River flows were 8.0m³/s, 16m³/s, 20m³/s, 40m³/s, 60 m³/s, 80 m³/s and 100 m³/s.

For all scenarios the horizontal salinity pattern of the Cubatão River was considered under well mixed conditions, because the HEC-RAS is a 1D model and it does not represents the vertical salinity gradient. So, it was not considered salt-wedge stratification or significant vertical salinity stratification in the simulated scenarios. The flows of Perequê and Mogi rivers were set as constant discharges of 4.0m³/s and 6.0m³/s respectively and the HB water discharge was set of 6m³/s, its operational constant flow. In all scenarios the Petrobras dam was considered not operating during the whole simulation period and it was investigated the seawater intrusion effects in the farther water abstraction point, upstream the HB channel (Figure 20).

The SLR simulations were made by adding 0.25m, 0.5m and 1.0m to the open sea boundary. This study focused just on the SLR effects on saline intrusion in Cubatão River, without changing runoff and topography and the effect of atmospheric forcing conditions (wind and heat flux) were not considered in this study.

For all simulated scenarios, there are some simplifying hypotheses for the applied model:

a) As a 1D model, the salinity vertical gradient is not represented, so the estuarine system is always considered in well-mixed conditions;
b) The Petrobras dam (Figure 20) is considered not operating during all simulation scenarios and it does not work as a barrier for seawater intrusion;
c) The idealized estuary simplifies the estuarine geometry, in which other rivers and the real bathymetry is not represented, which may affect the tidal propagation and seawater intrusion patterns;
d) Consequently, other river discharges that may impact the water circulation at Santos estuarine system are also not represented in the model;
e) The downstream boundary represents only the astronomical tide. The meteorological influences that produce variation in sea level, called meteorological tides, are not represented in the model.

5 RESULTS AND DISCUSSION

5.1 SALINITY SENSOR DESIGN, PROTOTYPE AND TEST

The electronic circuit for salinity measurements was based on Arduino Pro Mini microcontroller platform, which executes the written code, reads and saves the acquired data. The LMC 555 IC was set in the astable mode for EC measurements by generating a square-wave output signal as it alternately charges and discharges a capacitor, which should happen in the same time through the R1-150kΩ and the R2-390Ω resistors in circuit with the water environment, producing a 50% duty cycle with variable frequency. Figure 25 illustrates the LMC 555 pin configuration for EC measurements.

Figure 25 – LMC555 IC pins configuration for EC measurements.

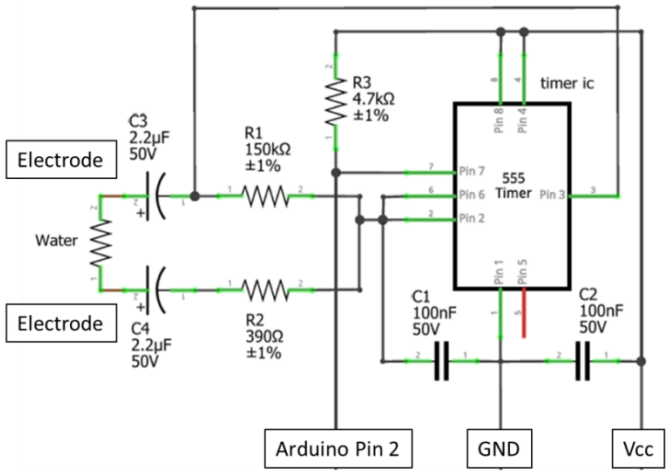

Fixed resistors (R1 and R2) serve to set a minimum frequency and to limit the maximum frequency allowed. When there is no contact with water and the resistance between the electrodes is extremely high, the R1-150kΩ resistor sets a minimum frequency of 20Hz. When the sensor is underwater and the resistance strongly decreases, the R2-390Ω resistor limits the maximum frequency to about 10,000Hz. The C3 and C4 2.2µF coupling capacitors in series with the water environment prevents even small DC do not flow through the electrodes from the LMC555 IC. They also provide galvanic isolation as the coupling effect can happen between two sensors or even between the sensor and other objects in the water, creating galvanic

currents. The C1 and C2 100nF nonpolarized decoupling capacitors in parallel to signal paths were applied to smooth the DC signal and protect the circuit from signal fluctuation. R3-4.7kΩ is a pull-up resistor used in pin 7. The key aspect is that the external environment (water) works as a variable resistor, altering the output frequency, which conductivity can be experimentally correlated (calibrated). The output frequency is transmitted through Discharge pin (pin 7) and read by Arduino pin 2 (green wire). Figure 26 illustrates the whole schematic circuit and Figure 27 the breadboard circuit.

Figure 26 – Sensor circuit (schematic).

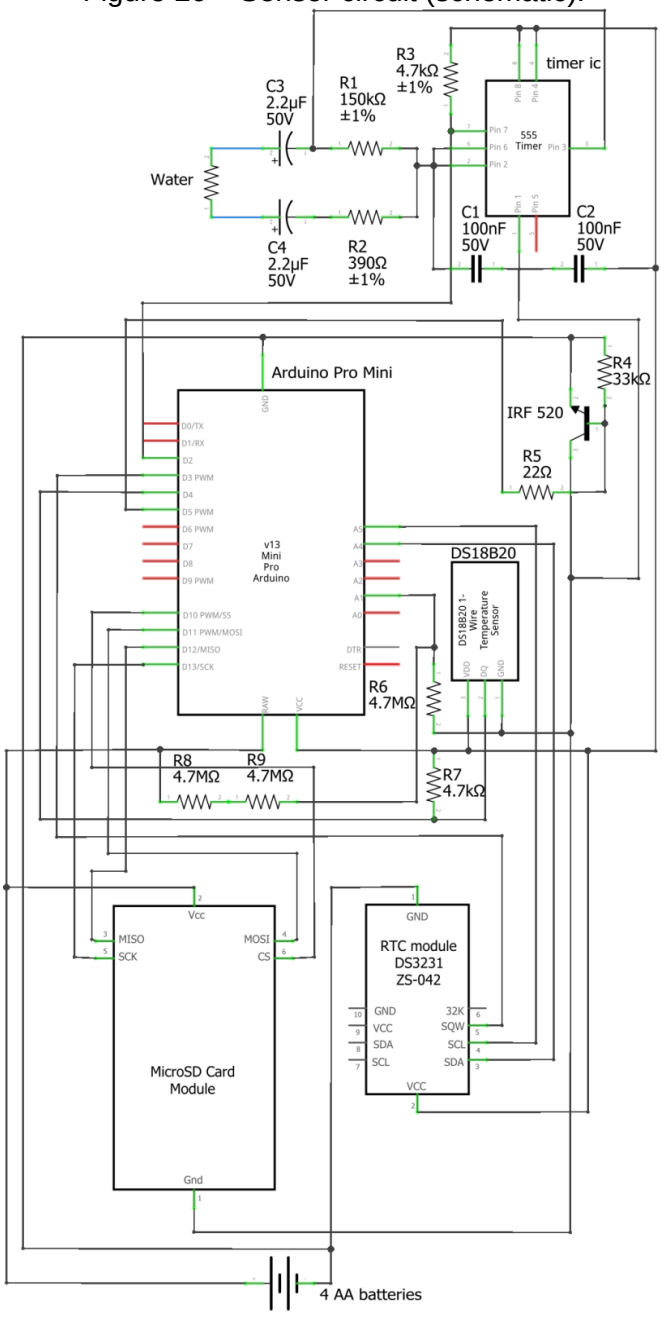

Figure 27 – Sensor circuit (breadboard).

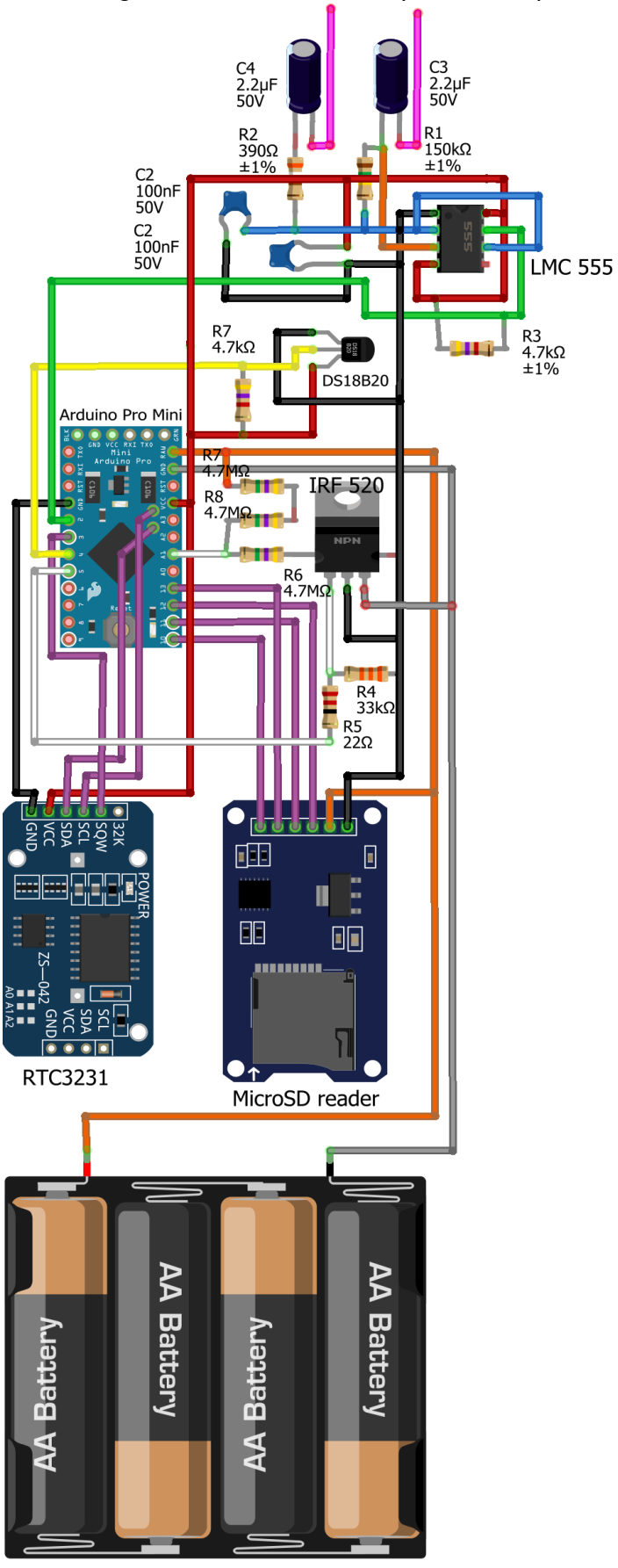

In the proposed sensor, four 1.5V AA alkaline batteries in series were used for power supply, because they provide more than the minimum 5V required by Arduino board to operate and, if water gets in the sensor, the power supply replacement price would be low. Different battery arrangement with D cells or C cells would increase the circuit power autonomy, but it would increase the sensor size, weight and price.

The Arduino Pro Mini plays an important role in the circuit, as it executes the written code for frequency and temperature measurements. Auxiliary modules were connected to the Arduino board. The RTC 3231 module was used to measure date and time with its data line (SDA) connected to Arduino pin A4 and its clock line (SCL) connected to Arduino pin A5. This module was also used as an alarm signal to bring the circuit out of the sleep mode through the square wave (SQW) pin connected to Arduino pin 3. When Arduino is set to sleep mode, it turns off all unnecessary components, reducing significantly the circuit power consumption, but it requires an external influence to wake up. As the RTC 3231 module has its own battery, it was used as this external influence to wake up the Arduino board.

The microSD reader was used to save frequency, temperature, data and time measurements on a microSD card with its chip select (CS) pin, master out slave in (MOSI) pin, master in slave out (MISO) pin and serial clock (SK) pin, connected to Arduino pins 10, 11, 12 and 13, respectively. The Ds18b20 temperature module data pin was connected to pin 4 on Arduino board for temperature measurements (yellow wire). The combination of resistors R6, R7 and R8 are connected to Arduino pin A1, which is used to read the battery voltage.

The MOSFET IRF 520 was used to reduce the circuit power consumption by cutting current to flow to LMC 555, Ds18b20 temperature sensor and microSD reader module. Its Gate pin was connected to Arduino pin 5 (white wire), Drain pin connected to the above mentioned components (black wire), and the Source pin connected to GND (grey wire). When the Arduino pin 5 is at HIGH stage, it sets a positive voltage at IRF520 Gate pin and the current flows between the Source and Drain pins, turning the electronic components on; when the Arduino pin 5 is at LOW stage, there is no voltage applied to the IRF 520 Gate pin and the components are turned off, reducing their power consumption.

The whole circuit works as follows: when it is connected to the batteries, Arduino pin 5 is set at LOW stage and the components in the black wire are turned

off and then the Arduino enters in the sleep mode. During this time, there is no data acquisition and the circuit is at its lowest power consumption. When the RTC 3231 internal clock matches a stated minute, its SQW pin sends a “wake up” signal (Alarm Interrupt) to Arduino pin 3 and the microcontroller set its pin 5 to HIGH state to allow current to flow through the electronic components for temperature and frequency measurements. The acquired data is saved on the microSD card through the microSd card reader, namely: date/time, temperature (ºC), frequency (Hz) and battery voltage (V). Then Arduino pin 5 is set to LOW state, the IRF 520 turns the components off, and Arduino enters in sleep mode again. The loop repeats ad infinitum while the circuit is powered with its minimum voltage requirements. The written code is in Appendix A.

The sensor was designed to work totally underwater with a moored application and present power autonomy of seven days, at least. Considering that the greater part of the low-cost water quality sensors are not designed to be totally submerged during their measurements, the main obstacle was to design the sensor housing considering its absolute sealing, as long as EC sensors necessarily requires probe contact with the external environment, i.e. the water. It was also pondered its weight and size to facilitate its installation and maintenance. The electronic circuit was protected by a 50mm PVC tube with a threaded union for internal maintenance as illustrated in Figure 28.

Figure 28 – Sensor housing and metal electrodes prototype.

The assembling time of one salinity sensor in approximately 6 hours and the calibration time is around 2 hours. The total construction cost, including Arduino microcontroller, Arduino modules, microSD card, electronic components, PVC tube and connections is approximately U$40.00 (Table 11).

Table 11 – Individual and total components costs.

Component	Cost (U$)
Arduino Pro Mini 16MHz 5V	7.00
RTC DS3132 module	3.00
MicroSD card reader module	3.00
MicroSD card	7.00
Ds18b20 temperature sensor	5.00
Electronic components*	6.00
50mm PVC caps	4.00
50mm PVC threaded union	4.00
Total Cost	39.00

*Wires, resistors, capacitors, LMC555, IRF520, batteries case.

5.1.1 Sensor experiments

Tightness and battery lifetime tests were conducted at Hydraulic Laboratory, at University of São Paulo and results showed that the housing design with a 50mm PVC tube and a threaded union was an adequate and an inexpensive option to protect the internal electronic circuit, as it worked normally during the tests and remained totally dry after the tests. Figure 29 illustrates the tightness tests conducted at the Hydraulics Laboratory testing channel.

Figure 29 – Tightness tests at Hydraulics Laboratory (USP).

Battery lifetime was also tested before calibration and validation tests. Generally, it is calculated based on the current rating in Milliampere (mA) and the capacity of the battery in Milliampere Hours (mAh). As in the proposed circuit the system goes to sleep mode, the current rating varies significantly on time. Based on laboratory tests, the sensor current rating and the battery capacity are:

a) Capacity rating of battery = 2300mAh;
b) Current consumption of device during sleep mode: 7mA;
c) Current consumption of device during wake: 30mA;
d) Number of wakes per hour: 60;
e) Duration of wake time: 2000ms.

The above values are an approximation; some devices presented higher or lower current consumptions, varying from 3mA to 9mA during sleep mode and from 26mA to 32mA during the full operation period. Considering the approximate values and a capacity rating of battery derated by 15% to account for some self-discharge, the estimated battery life time is ten days. This power supply arrangement assures a circuit operation of seven days, at least, which is satisfactory considering fieldwork frequency for maintenance purposes.

The sensor calibration presented a consistent correlation between Frequency readings (Hz) and EC values (mS/cm). For lower EC values, a second order polynomial expression best described the correlation between Frequency and EC,

with $R^2 = 0.9950$. For higher EC values, a linear equation fits adequately, with $R^2 = 0.9989$. Table 12 illustrates the Frequency readings for the corresponding EC at 23°C and Figure 30 illustrates the sensor calibration curve.

Table 12 – Frequency readings for each corresponding EC at 23°C.

S (g/kg) approx.	EC (mS/cm)	Frequency (Hz)
0	0.00	34
1	1.93	882
2	3.67	1281
3	5.35	1569
4	7.09	1759
5	8.61	1887
10	16.50	2235
15	23.87	2609
20	30.90	2964
25	38.21	3351

Figure 30 – Sensor calibration curve.

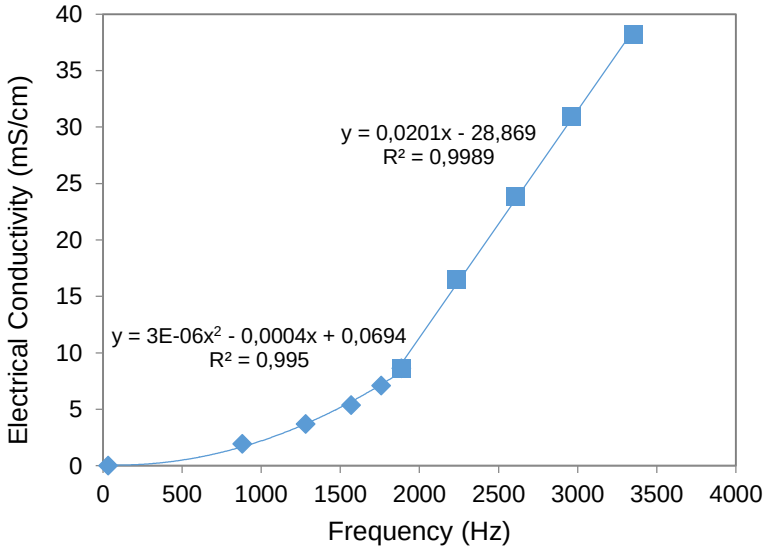

It is important to notice that this calibration curve is related to the 23°C calibration temperature which means that EC measurements must be adjusted for the measured temperature using Eq. 64. Calibration tests were developed in a maximum salinity range of approximately 25 g/kg, which is satisfactory for estuarine river applications, but as long as a linear equation describes the Frequency x EC

relation for high salinity values and the maximum frequency sensor measurement is about 10,000 Hz, it is seemingly also applied to higher salinity ranges.

Validation experiment was conducted from 25 April 2019 12:00 to 01 May 2019 00:00, in Cubatão River, in an approximately water depth of 2.5m. Both the developed sensor and the industrial reference device were set to acquire data every one minute in a moored application, with a final 7920 acquired data each.

Temperature measurements showed a RMSE of 1.192°C. Sensor temperature reading presented an inconsistent behavior compared to the reference data with unusual fluctuations and being almost always bellow the reference value. In temperature, the maximum relative error was of 14.26%, which can cause some effect on salinity readings. This variation can be partially explained by an assembling issue in the DS18B20 electronic device and its housing, since it was totally inside the PVC tube and measured the internal temperature, which can present different reading from the external environment. Figure 31 illustrates temperature measurements taken during the validation experiments. This design problem can be easily solved attaching the sensor to a heat conveyor (a metal pin) that passes through the wall of the PVC case.

Figure 31 – Temperature measurements.

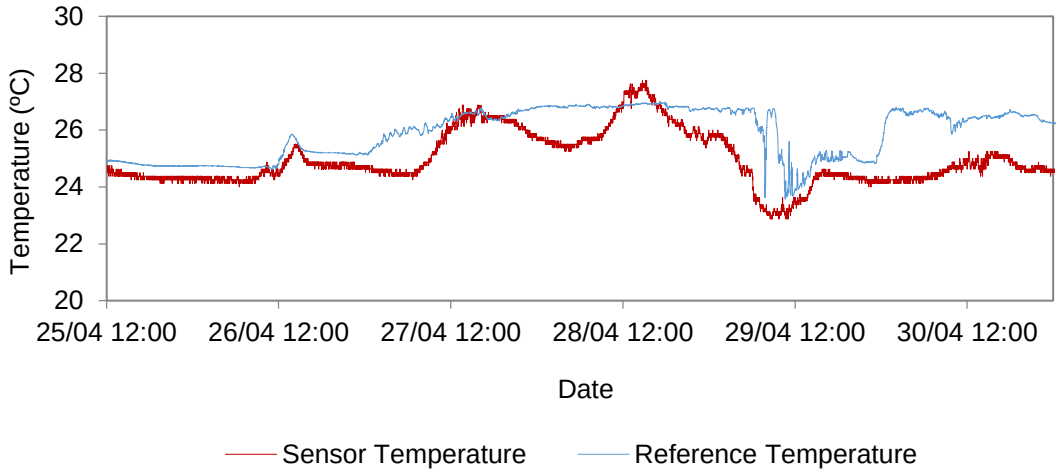

Using the sensor temperature reading for EC and salinity equations, salinity measurements presented a 1.445g/kg RMSE, a 0.9392 R^2 and a 0.9383 EF values. In this constituent, the sensor measurements presented a good general behavior, even considering the salinity fluctuation during the validation period. Just in few

moments the sensor presented an unusual behavior, which in major cases can be explained by the temperature readings, which affected the EC adjustment and salinity calculations.

In order to reduce the impacts of inadequate temperature measurements in salinity equation, it was used the reference temperature to calculate EC adjustment and salinity concentration. In this case salinity measurements presented a 1.438 g/kg RMSE, a 0.9412 R^2 and a 0.9851 EF values. There was a slight improvement on salinity readings using the reference temperature, indicating that the proposed salinity sensor, with a more accurate temperature data as mentioned can deliver acceptable salinity measurements results for estuarine environments monitoring.

In Figure 32(a) it is possible to notice that some sensor measurements presented a discrepancy from the reference value, mainly due to the high variance of salinity values and as a consequence of the sensor temperature readings. Figure 32(b) illustrates the effect of using the reference temperature in EC and salinity equations, in which the box shows the periods of evident improved salinity measurements. Figure 33 also illustrates the improvement on salinity measurements when using the reference temperature compared with the sensor temperature data.

Figure 32 – Salinity measurements with (a) sensor temperature and (b) reference temperature.

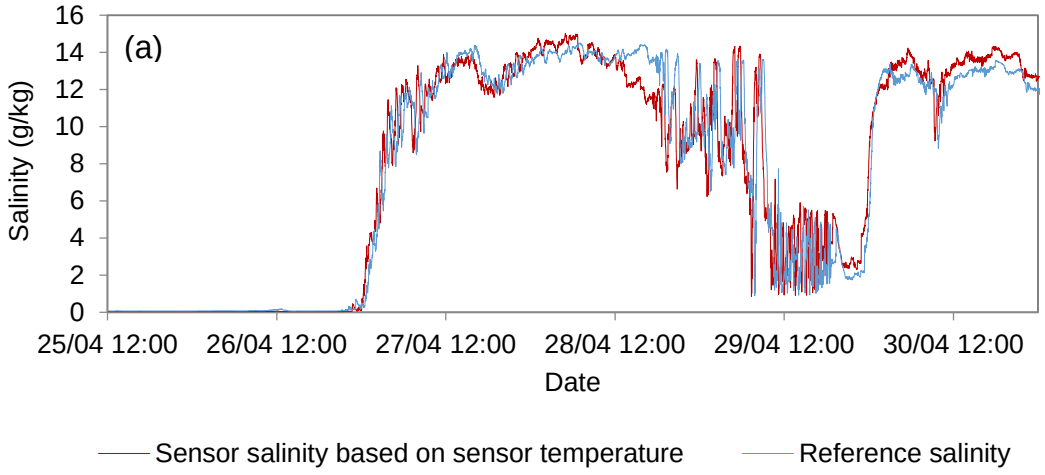

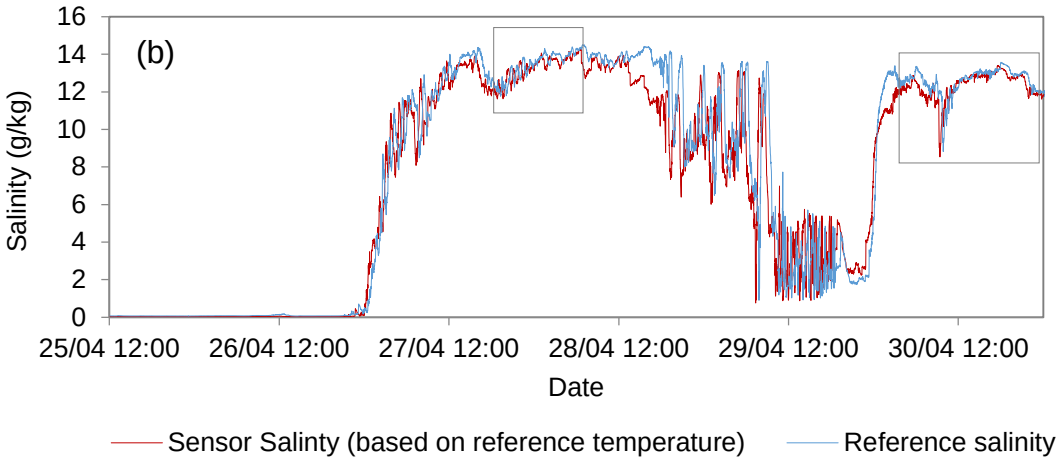

Figure 33 – Coefficient of determination between salinity values.

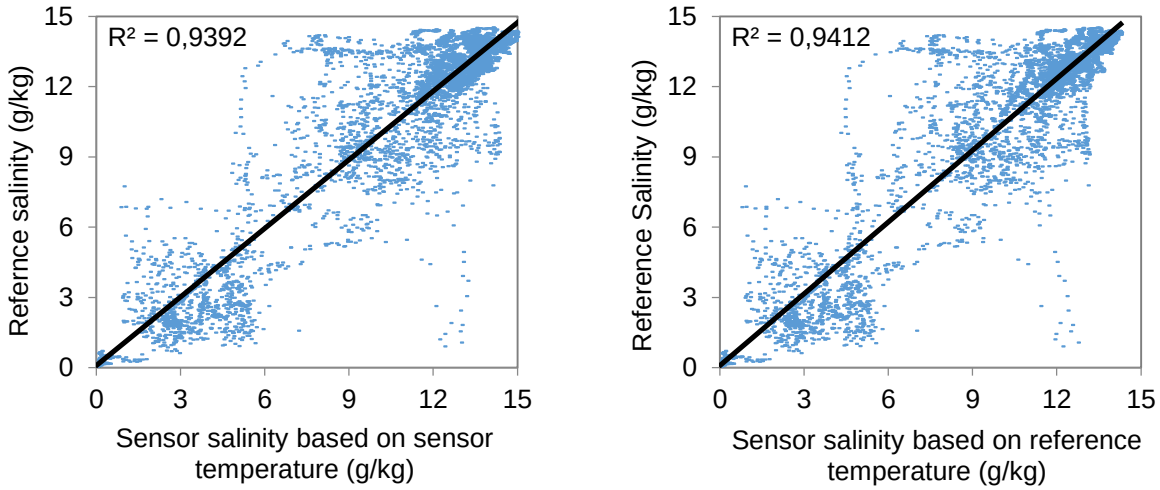

After validation tests, the internal electrical components were completely dry and the external PVC tube and connections remained intact, even facing considerable forcing events, such as freshwater discharge and tidal activity, which demonstrate that the designed housing is adequate to fully submerged applications in shallow water bodies.

The validation period did not cover the whole battery capacity, which is approximately ten days with a one minute data acquisition interval. However, during the six monitoring days, the batteries worked normally, delivering the minimum 5V power supply to the sensor. In general, the validation test demonstrated that the low-cost Arduino-based EC sensor performed well in a fully submerged application,

which is one of the greatest challenges in developing EC sensors for water quality monitoring purposes.

5.2 FIELD SURVEYS

The Cubatão River discharge was based on its rating curve (Figure 34) located at its upstream section, near HB discharge (Figure 20). All river discharge values for both field surveys and hydrodynamic models were estimated by this rating curve, which was created based on the previous Cubatão River discharge data (FCTH, 2017).

Figure 34 – Rating curve of Cubatão River.

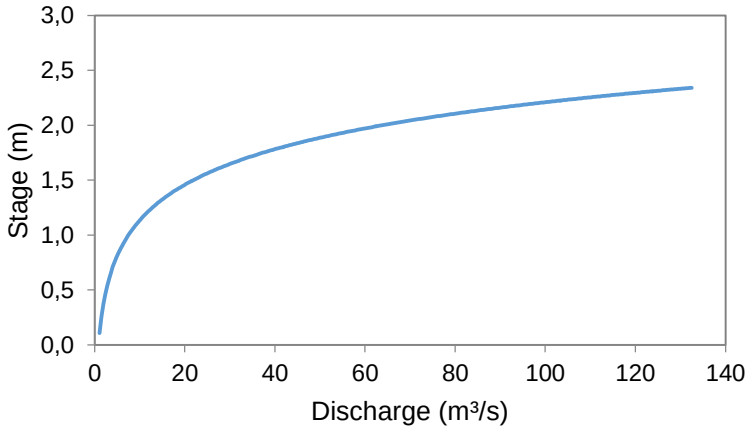

The local water level was measured at P1 during the first field survey, but during the second field survey it was estimated indirectly by applying a linear regression comparing the observed data at P1 and the water level at COSIPA. Figure 35 illustrates the stage (m) at P1 and COSIPA during the first field survey. As the stations are near each other, their behavior is very similar, even their local effects on tides.

Figure 35 – Stage at Cubatão River (P1) and COSIPA (First field survey).

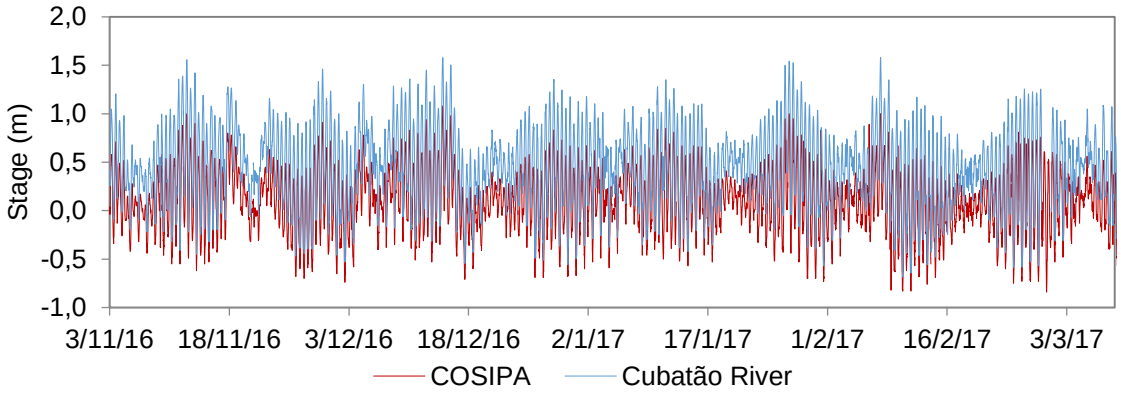

With a linear regression, it was possible to set a linear equation that correlates the stage at P1 to the stage at COSIPA (Figure 36). Then, it was possible to estimate indirectly the stage at P1 during the second field survey (Figure 37). Unfortunately, there was a lack of stage data at COSIPA exactly during the second field survey, being impossible to estimate P1 stage for some days. In any case, the estimation presented similar behavior to the observed during the first field survey.

Figure 36 – Linear regression of Cubatão River and COSIPA stages.

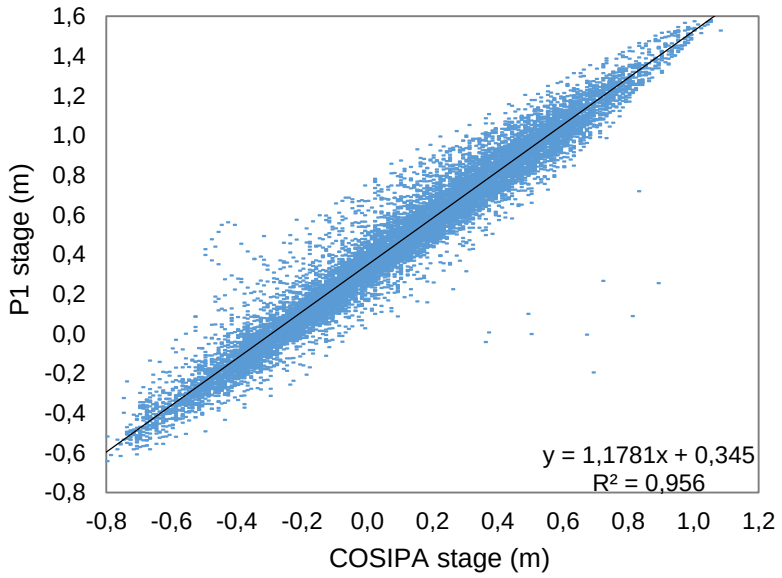

Figure 37 – Stage at Cubatão River (P1) and COSIPA (Second field survey).

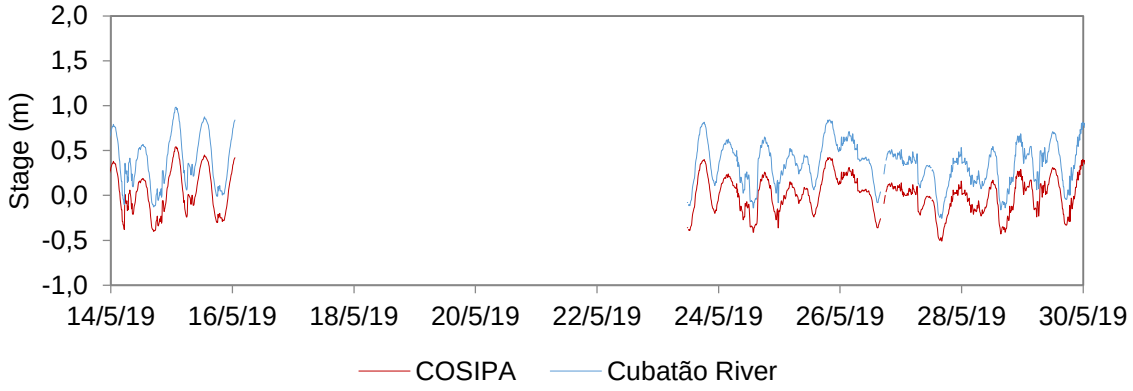

5.2.1 First Field Survey

During the first field survey, salinity stratification presented a complex behavior due to the effects of HB discharge, precipitation and tides. A particular aspect of Cubatão River is that HB discharges present an inconstant operational pattern and its discharge is much higher than the natural river discharge. So, even considering that the HB discharges occur during short periods, they are a significant forcing factor in salinity behavior on the river. The HB discharges can also present a high variation, ranging from 20m³/s to its high discharge capacity, 150m³/s, approximately. During the first weeks of the field survey, for example, HB released water in Cubatão River just a few times with an average discharge of 70m³/s. In January, 2017, on the other hand, HB discharges were much more frequent and closer to its maximum capacity.

Precipitation data also presented a significant variation. During the four months monitoring period, there were days with no precipitation events, while other days presented intense rainfall events, with almost 50mm. This variation has an impact on Cubatão River flow and, consequently, on salinity stratification pattern.

Figure 38 illustrates the combined data of precipitation (mm), water stage (m), HB discharge (m³/s), Cubatão River flow (m³/s) and salinity concentration in three different depths at P1 (g/kg).

Figure 38 – Precipitation, stage, HB and river discharge and salinity stratification during the first field survey at P1.

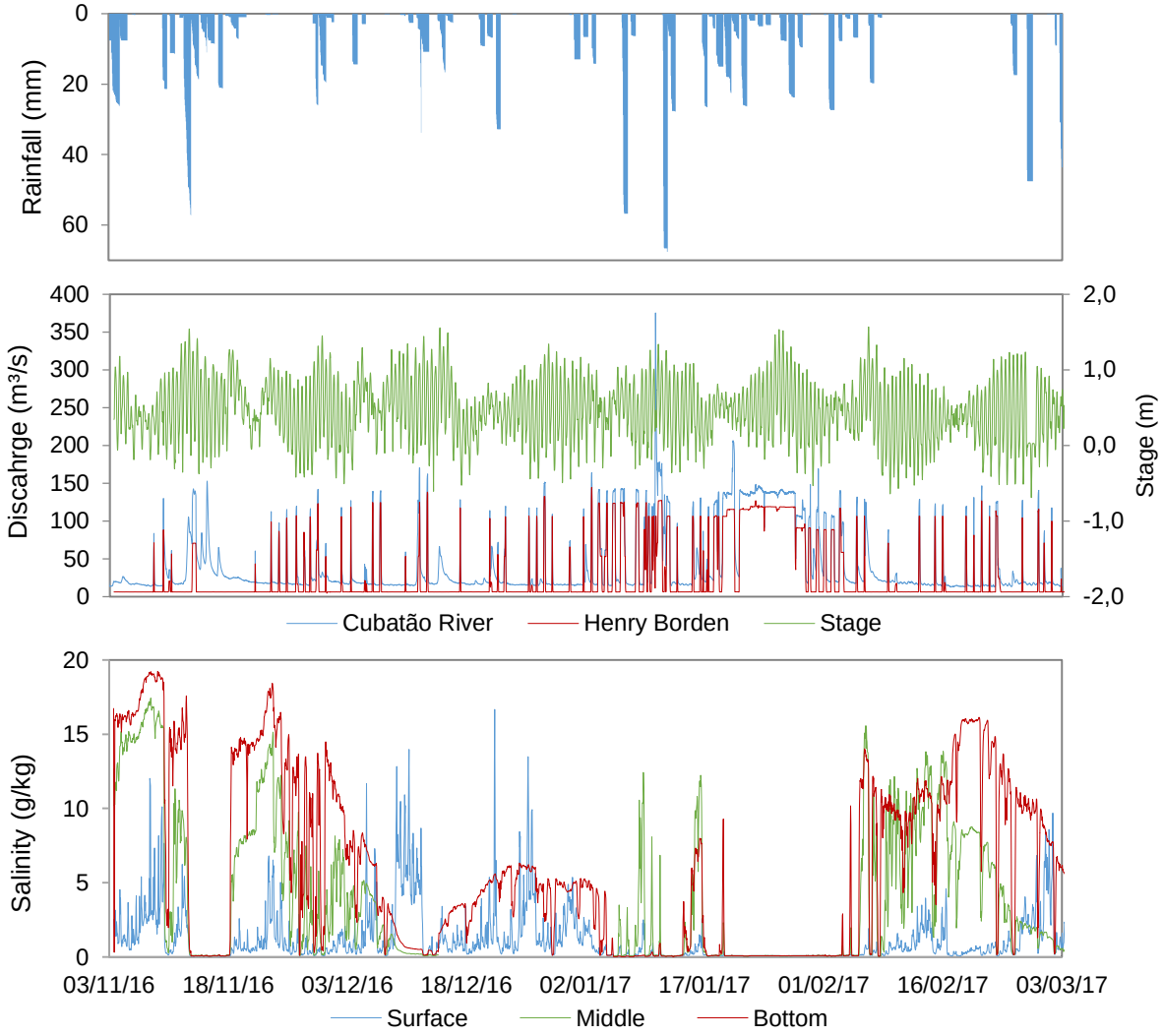

Under high precipitation events combined with HB discharges, salinity concentration results show that stronger flow pushes salinity downriver, which means that under this combination, the downstream part of the river presents salinity concentration close to zero along the water column. The combination of HB discharges and high precipitation can cause a discharge high enough to flush out seawater intrusion in this part of the river, which can make freshwater predominant during days along Cubatão River. Salinity stratification tends to be sensitive to HB discharges. However, usual HB discharges are not strong enough to flush salinity out of Cubatão River, but even short HB discharges may influence salinity stratification in the water column at P1.

From 03/11/16 to 18/11/16, there was an intense saline stratification in the water column during the first days. This stratification happened due to the reduced

HB discharge and rain event, which indicates that when tides are the dominant forcing mechanism, seawater intrusion is strong even during neap tides, and there is a remarkable salinity stratification in the water column. In the last days, the rainfall events and the ebb flow flushed out seawater from P1 and salinity concentration was totally reduced. It is evident that a single intense rainfall event may flush seawater intrusion out Cubatão River for days.

From 18/11/16 to 03/12/16, as a consequence of low rainfall and low HB discharge, salinity stratification was rapidly reestablished. It is possible to notice that some HB discharges of 100m³/s in sequence reduced the salinity concentration along the water column, but it was not enough to flush seawater out from P1. Even with reduced salinity concentration, salinity stratification was still present and salt wedge was present at the major time. Combination of HB discharges and rainfall were only able to cause a slight mixing process and salinity stratification became weaker, but it is not sufficient to cause a fully mixing process.

From 03/12/16 to 02/01/17 the salinity sensor in the middle of the water column stopped working and it was more difficult to analyze the salinity stratification behavior. However, it is possible to notice a reduced salinity concentration, probably caused by the HB discharges and higher rainfall events. There was an unusual stratification pattern, in which salinity concentration in the bottom was higher than the near surface layer. The middle sensor absence restricted a reliable investigation, but it probably happened due to the complex mixing process in this part of the estuarine river.

From 02/01/17 to 01/02/2017, there were intense precipitation events and the most intense HB discharges during this field survey. Consequently, salinity concentration was strongly affected, reaching null values for more than two weeks, which means a well-mixed condition. The combined effect of HB discharges and precipitation was again high enough to totally reduce salinity concentration, but this time for a much longer period. It shows that HB discharges play an important role in Cubatão River water management, because when it is operating at its maximum capacity, it changes significantly the river flow. During this period, P1 was under neap and spring tides, but seawater intrusion was still vanished from Cubatão River, which indicates that tides are not the most important forcing mechanism for salinity patterns

in Cubatão River, but the freshwater discharge, strongly affected by rainfall and HB discharges.

From 01/02/17 to 03/03/17, HB discharges became regular again and precipitation events were reduced, which reestablished seawater intrusion and an increase in salinity concentration along the water column. As a consequence of reduced HB discharges, it was also possible to identify salinity stratification again, with high bulk vertical salinity gradient, varying from 1.0 g/kg.m to 4.0 g/kg.m. Salinity stratification was totally evident during reduced HB discharges combined with no rainfall events during neap tide.

It is also possible to investigate salinity stratification during the monitoring period using the stratification parameter n_S. Practically half of the time during the monitoring period (55.4%) the salt wedge pattern is present (n_S>1.0). In Cubatão River, this type of salinity stratification usually happens when there are low precipitation events and low HB discharge during neap tide. This means that salinity stratification with high vertical salinity gradient occurs when there is HB discharge and rainfall events in Cubatão River. During high flows in Cubatão River, seawater is partially or totally flushed out the monitoring point, reducing salinity concentration. Precipitation events and HB discharge increase Cubatão River flow. In that case, flow is high enough to flush out the seawater from the monitoring point or change the stratification pattern.

Well mixed water (n_S<0.1) occurred in 27.2% of the monitoring period. It occurs when there are high precipitation events combined with high HB discharges during spring tide, in which there is only freshwater influence in the monitoring point and seawater goes downstream the river.

Partially mixed stratification type (0.1<n_S <1.0) occurred in 17.5% of the monitoring period, but it is more complex to determine the conditions in which it occurs. In that case, it can be considered a transitional stratification pattern between the salt wedge type, in which HB discharges and rainfall events are negligible, and the well mixed type, when Cubatão River flow is high enough to flush out the seawater from the monitoring point.

The stratification parameter variations confirmed that Cubatão River salinity stratification pattern is sensitive to different forcing conditions, namely the HB discharge, rainfall events and tides. The field survey was necessary to demonstrate

that salinity stratification not only occurs, but the salt wedge is the predominant type of stratification in the monitoring point. Considering that HB discharge affects its salinity intrusion and stratification, it is a crucial forcing factor that must be examined in future water resources and management projects in Cubatão River.

5.2.2 Second Field Survey

The second field survey was conducted from 14/05/2019 to 30/05/2019 in two monitoring points: P1, the same point of the first field survey, and P2, a new point located 2.3km upstream P1. Figure 39 and Figure 40 illustrate the installation and maintenance of the three salinity sensors at each monitoring point.

Figure 39 – Maintenance of salinity sensors at P1.

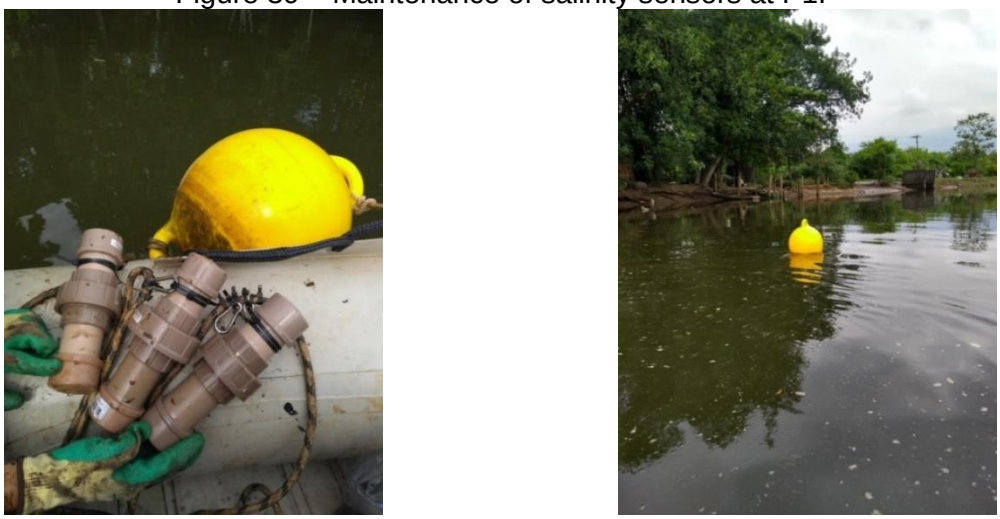

Figure 40 – Maintenance of salinity sensors at P2.

The sensors were installed with a moored application using an anchor buoy. The sensors were attached to a rope with a weight on its end to keep it straight in the water column. A second rope was attached to the buoy with a heavier weight to anchor it on the river bed.

This field survey showed analogous results with the first field survey, in which salinity stratification presents similar behavior when exposed to the forcing mechanisms. Figure 41 illustrates the combined data of precipitation (mm), stage (m), Cubatão River discharge (m³/s) and salinity concentration in three different depths at P1 (g/kg).

Figure 41 – Precipitation, stage, river discharge and salinity stratification during the second field survey at P1.

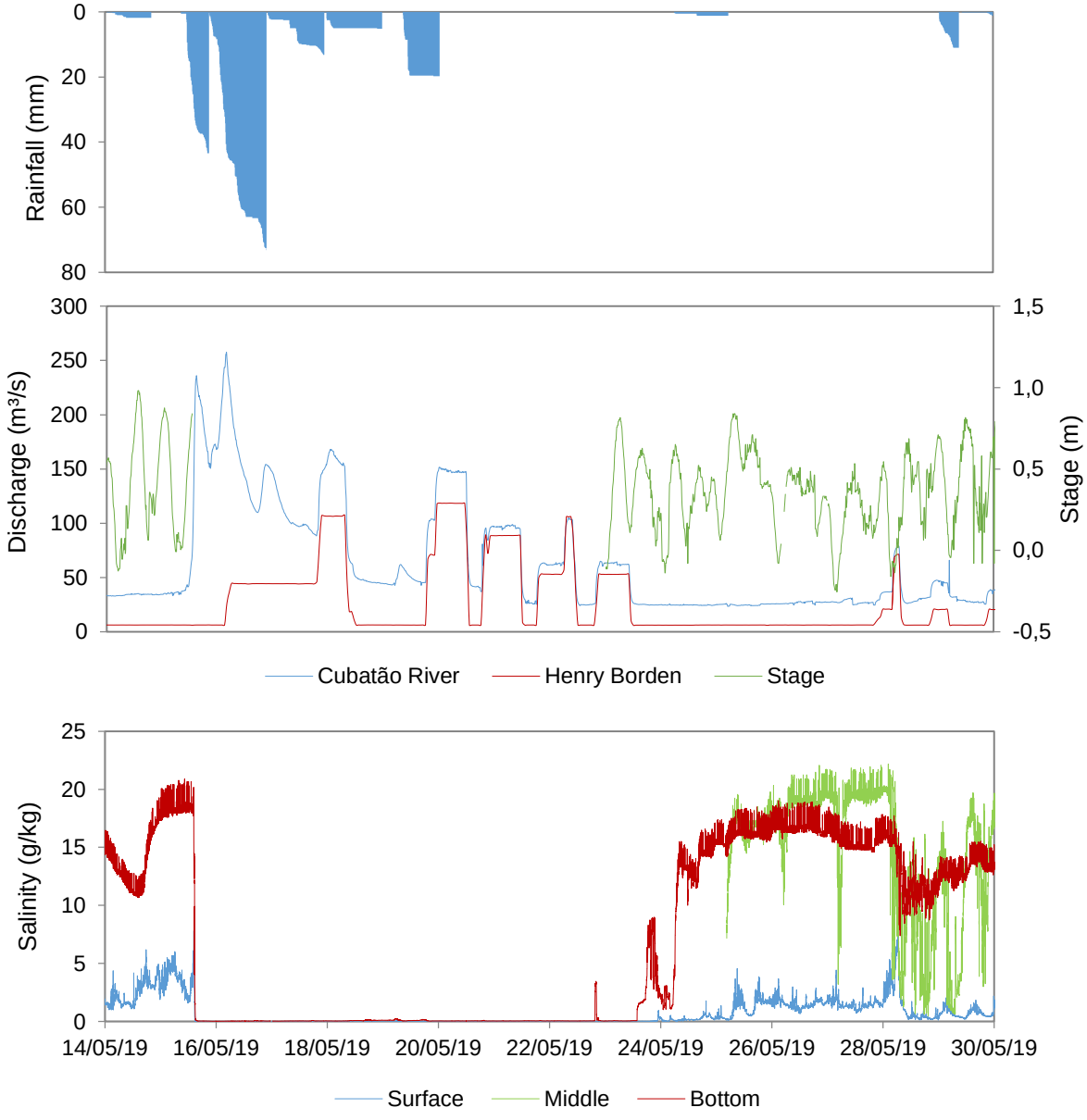

Unfortunately, the sensor in the middle of the water column did not work during amajor time of the field survey, it was replaced just in the last five days; and the COSIPA water stage data presented a lack specifically during the monitoring period, so it was impossible to estimate the water stage at P1. Besides that, the field survey was conducted properly and it was possible to evaluate the salinity behavior during this period.

During the first hours, there was a distinct salinity stratification in the water column as a result of low rainfall and HB discharge. In that case, tides are the most important mechanism and salinity intrusion is strong in Cubatão River. This salinity behavior matches with the first survey, even the salinity concentration range near the bottom and near the surface.

In the dawn of 16/05/2019, there was a long and intense rainfall, with a maximum precipitation of 70mm, which increased significantly the river discharge, reaching more than 250m³/s, 16 times its normal discharge. This rainfall combined with HB discharges flushed seawater intrusion out Cubatão River for more than eight days, making freshwater predominant during this period. It is important to notice that for both field surveys, when a high discharge occurs, the salinity rapidly vanishes, independently of the tide and salinity concentration.

In both cases, the salinity reestablishment also occurs rapidly, mainly when tides are the evident forcing mechanism. However, this process happens in different times along the water column, because the seawater intrusion is not homogeneous and salinity concentration tends to be higher near the bottom of the river and lower near the surface, that is why near bottom salinity appears first than near surface. After 24/05/2019, the salinity stratification was totally present again, which happened because the rainfall was almost null and there was no HB discharge as well. In the last days, low HB discharges affected the stratification and slightly reduced the salinity concentration near the bottom, but the stratification was still evident.

Considering the monitoring points P1 and P2 individually during the field survey, it is possible to notice the effect of the high river discharge on salinity concentration and temperature. At P1, during the first hours, water temperature presented values higher than 24ºC in the water column, with surface water showing some variation due to solar radiation, while bottom water presented almost constant temperature, as solar radiation reaches it with less intensity. During the flood event, there was a

sudden drop in water temperature, followed by a gradual reestablishment during the next days. In the last days, there was a small drop in temperature caused by HB discharges, but less intense compared to the flood event. The temperature behavior was similar to the salinity concentration, which indicates that both are sensitive to the river discharge (Figure 42).

Figure 42 – Temperature and salinity at P1.

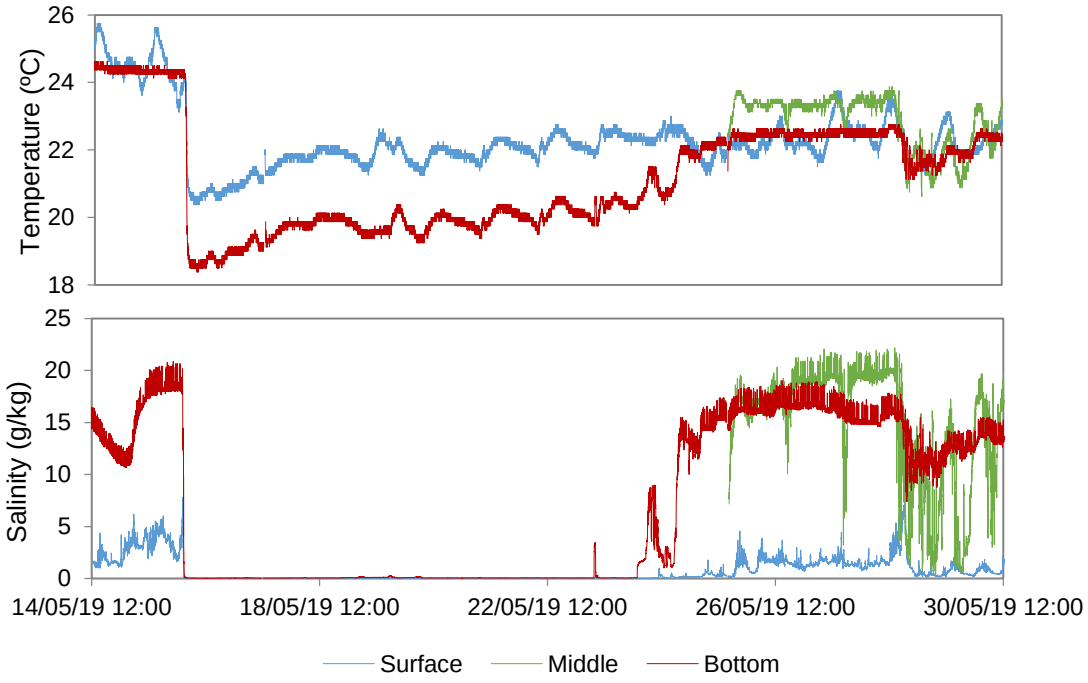

At P2, water temperature also presented a different behavior during the first hours, with bottom temperature higher than surface temperature. As discussed previously, the temperature sensor of the electronic circuit may present lower accuracy than required, which can explain this temperature discrepancy. In any case, water temperature at P2 also presented a sudden drop during the flood event and a gradual increase with time, following the same pattern of P1 temperature.

The salinity concentration was also vanished as a result of the flood event, similarly to P1 pattern. During this flood event, the sensors and the buoy were dredged 100m downstream the original position of the monitoring point and anchored under the bridge. When the equipment was recovered after days, the batteries were totally consumed and there was a lack of data of the temperature and salinity reestablishment. It was decided to fix the sensors near the river bank for safety reasons, but it was not a representative point in the river cross section and the

acquired data were below the expected, as shown in the last days of the field survey (Figure 43).

Figure 43 – Temperature and salinity at P2.

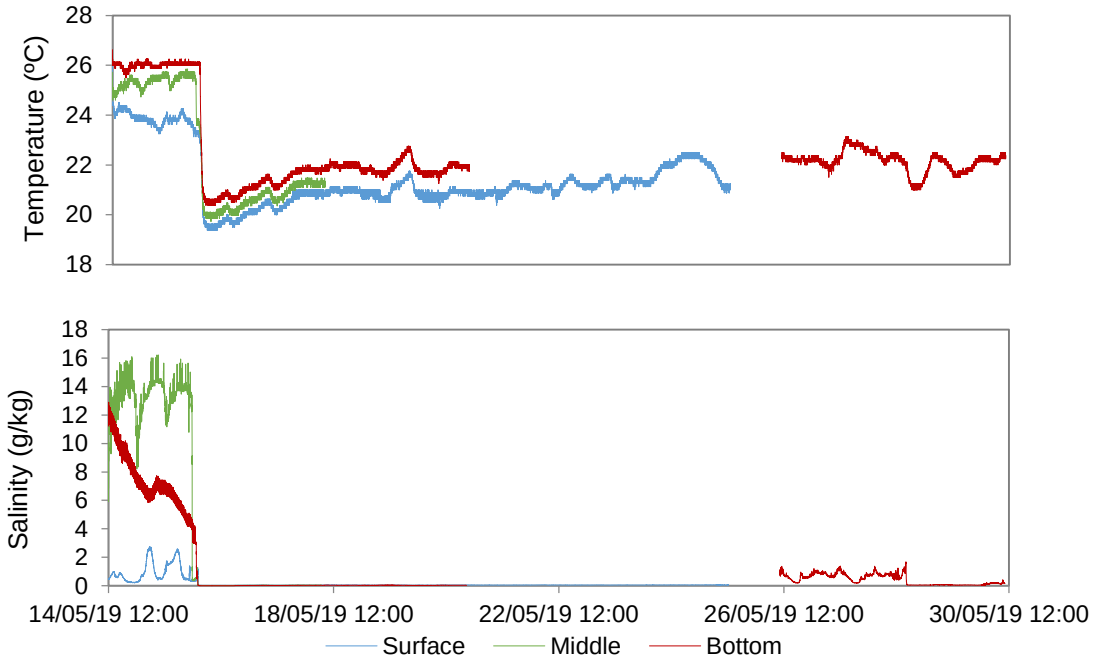

In terms of stratification parameter (n_S) the salinity behavior during the second field survey presented analogous results compared to the first survey. During 54.6% of the time (55.4% during the first survey), the stratification type was the salt wedge pattern (n_S>1.0), in which there is a large difference of salinity between the surface layer and the bottom layer.

Well mixed water (n_S<0.1) occurred during 44.7% of the time (27.2% during the first survey), predominantly as a result of the flood event that flushed the seawater out P1; and partially mixed stratification type (0.1<n_S <1.0) occurred only in 0.7% of the time, against 17.2% during the first survey. The above results reinforce the sensitivity of the Cubatão River stratification to HB discharges and flood events, as it changes abruptly from salt wedge type, when there are no significant forcing mechanisms, to fully mixed type.

Fieldwork results showed that when the Cubatão River conveys its natural flow and the operational discharge from HB, with values between 15-25 m³/s, the salt stratification is present in both monitoring stations, P1 and P2. Even in case of small precipitation events or under short HB high water discharges, the stratification is still

present, but with some disturbance. On the other hand, when the Cubatão River discharge increases significantly, with values higher than 50m³/s, the freshwater extends its influence downstream and it may flush the salinity out from the river and leads the salinity concentration to zero during days.

The salinity concentration results for both first and second field surveys are in consonance with a precursor study at Santos estuarine system, in which salinity measurements were developed in the 1970s (SONDOTECNICA, 1977). Even after 50 years, with significant modification on Santos estuarine hydrodynamics, such as dredging procedures; installation of port facilities; adjustments on HB operational discharges; and natural changes on river morphodynamics, the salinity concentration range still presents a similar behavior. According to Sondotécnica (1977), the salinity concentration at Santos estuarine is affected by freshwater discharges, mainly during the neap tide, in which the tidal range is reduced. The field survey results are in accordance with it, because the monitoring points are in a region very affected by river and HB discharges.

5.3 SEAWATER INTRUSION MODELING

5.3.1 Calibration and validation model performance

The model calibration procedure was performed by comparing the simulated data with the observed data in the same period for both hydrodynamic and water quality models. It was used the observed data from the second field survey, conducted in May, 2019. The best adjustment between computed and observed data was achieved for Manning coefficients of 0.06 $s/m^{1/3}$ in the idealized estuary and 0.03 $s/m^{1/3}$ in Cubatão River reach. This last value was also adopted in Mogi and Perequê tributaries. Figure 44 illustrates the comparison between simulated and observed stage data at P1.

Figure 44 – Hydrodynamic calibration at P1.

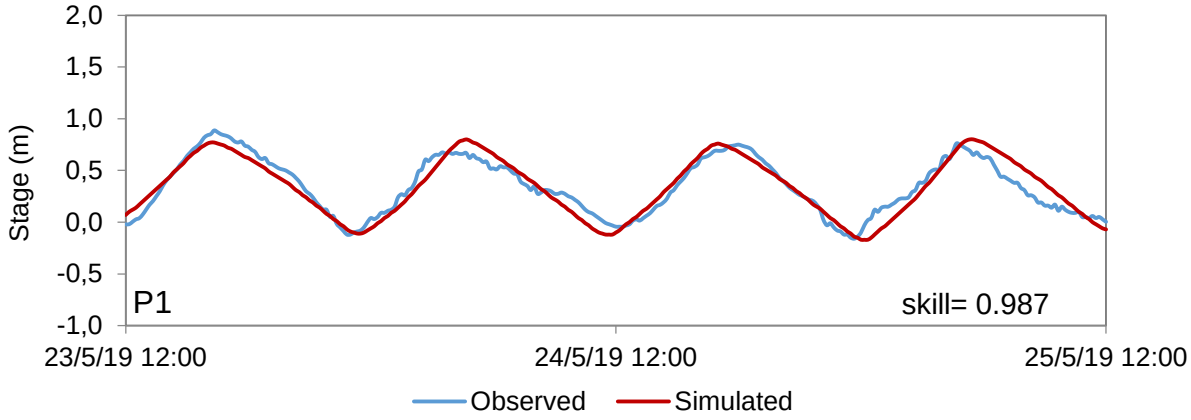

For the water quality model, the D_x coefficients varied from 370 m²/s to 580 m²/s along the idealized estuary and the river sections. Figure 45 illustrates the comparison between simulated and observed salinity at P1 and P2 in the same period and Figure 46 illustrates the simulated salinity spatial variation and the observed salinity at P1 and P2 at Cubatão River in a specific moment. The initial distance (00km) is the confluence of Cubatão and Mogi rivers.

Figure 45 – Water quality calibration at P1 and P2.

Figure 46 – Salinity spatial variation (calibration).

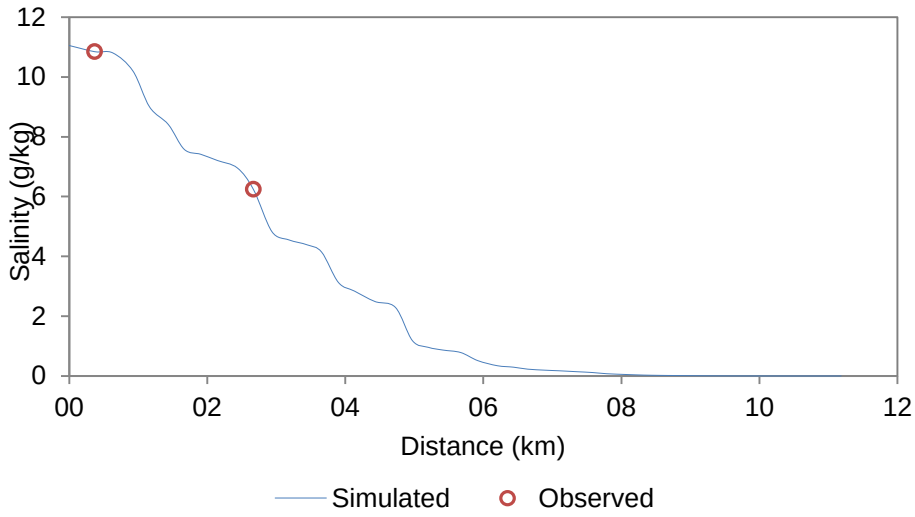

The model validation was performed by comparing the simulated data with the observed data in a different period to certify the calibrated n and D_x coefficients. It was used the observed data from the first field survey, conducted in 2016/2017. Figure 47 illustrates the hydrodynamic model validation, Figure 48 the water quality model validation and Figure 49 the simulated salinity spatial variation and the observed salinity at P1 in Cubatão River in a specific moment. The initial distance (00km) is the confluence of Cubatão and Mogi rivers.

Figure 47 – Hydrodynamic validation at P1.

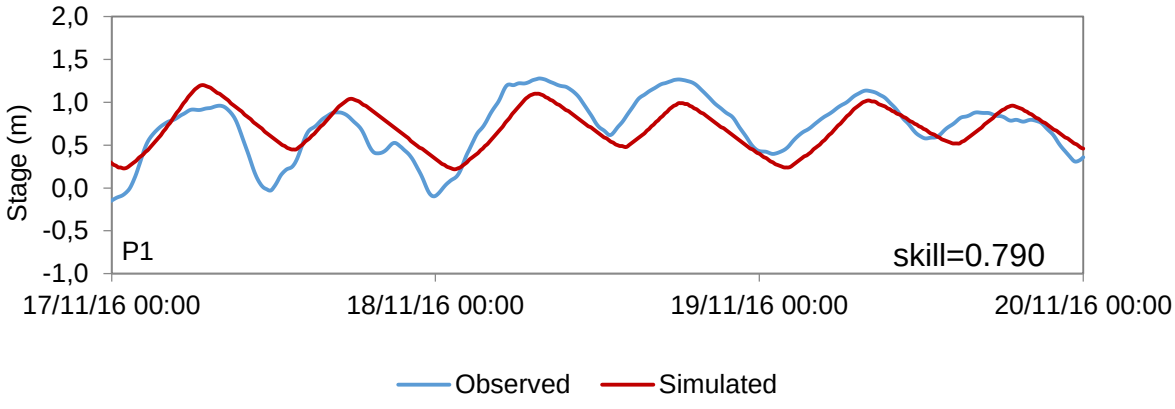

Figure 48 – Water quality validation at P1.

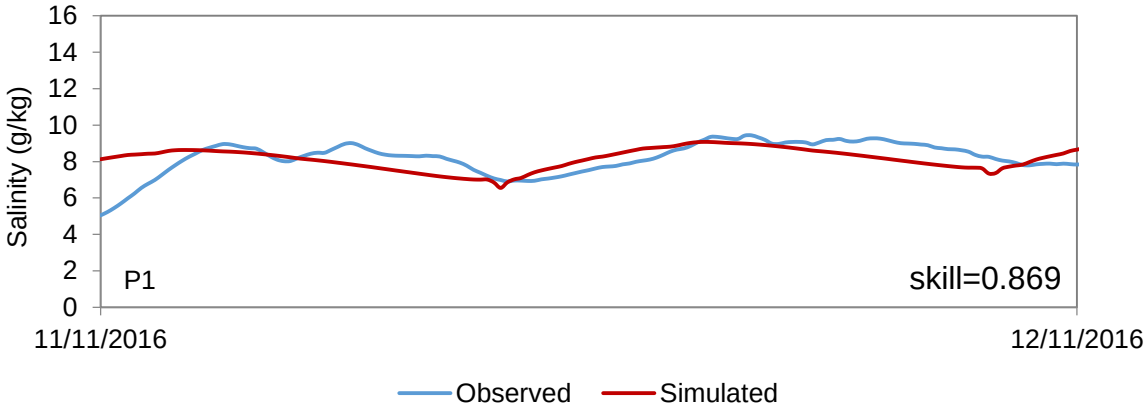

Figure 49 – Salinity spatial variation (validation).

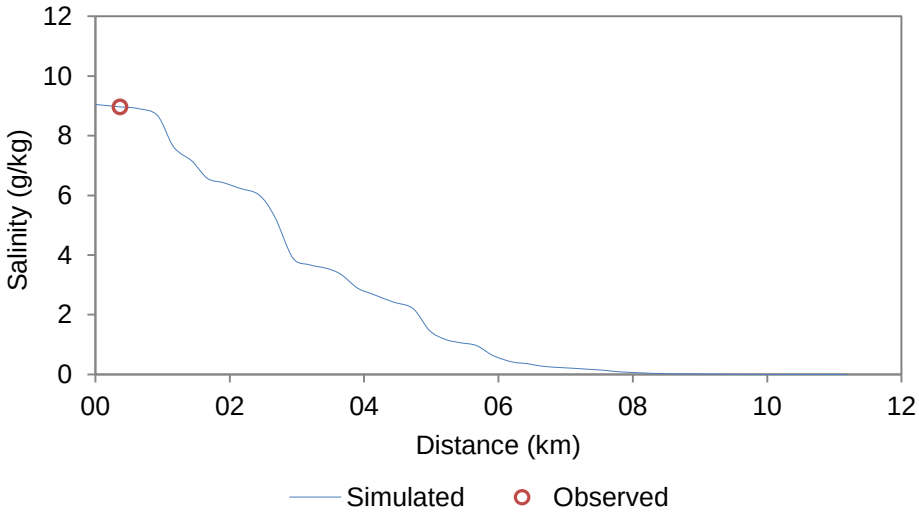

The hydrodynamic and water quality models performed simulations in agreement with the observed data, with skill values for both calibration and validation procedures higher than 0.75, which indicates an excellent model performance. So, the model is capable of performing simulations under different forcing conditions and be used as a tool to predict seawater intrusion behavior in Cubatão River. Table 13 shows the skill value and model performance for calibration and validation procedures.

Table 13 – Skill values (calibration and validation).

Parameter	Station	Skill	Performance
Calibration			
Water stage (m)	P1	0.987	Excellent
Salinity (g/kg)	P1	0.897	Excellent
	P2	0.813	Excellent
Validation			
Water stage (m)	P1	0.790	Excellent
Salinity (g/kg)	P1	0.869	Excellent

It was also performed a sensitivity test of seawater intrusion response to high Cubatão River discharge. The observed Cubatão River and HB discharges were imposed as upstream forcing conditions and the observed tides as downstream forcing conditions during a high river discharge event. As there were no observed data for Perequê and Mogi Rivers discharges, it was imposed the same constant 4m³/s and 6m³/s, respectively, and the discharges were multiplied by ten during the flood event.

The model presented a consonant performance under an extreme event that push seawater intrusion from Cubatão River: the model was able to simulate the abrupt salinity decrease almost at the same time of the observed data; salinity concentration remained practically null during the whole flood event; and salinity concentration reestablished its concentration values similarly to the observed data. Some discrepancies may be explained by the absence of observed discharge values of Mogi and Perequê Rivers, but in general the model presented similar behavior when compared to the observed data (Figure 50).

Figure 50 – Salinity response to high river discharge.

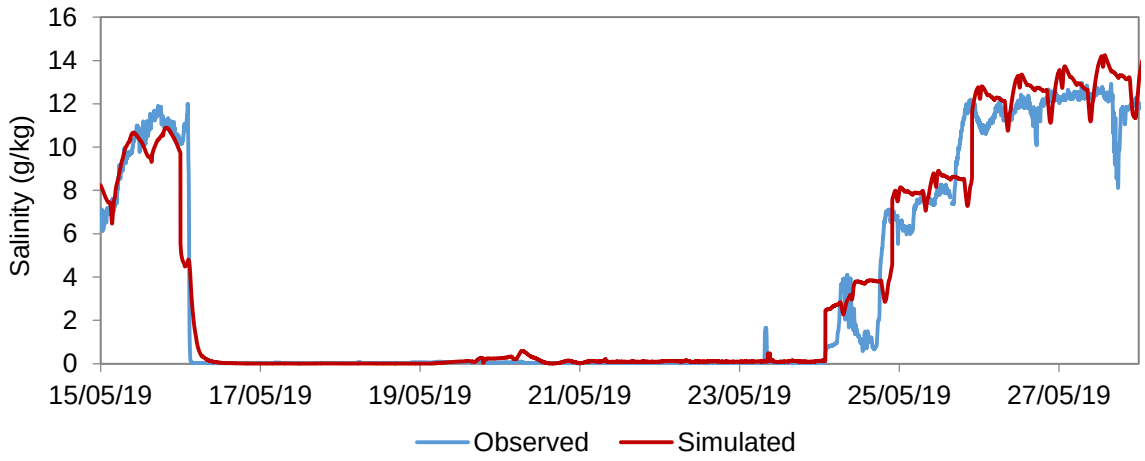

5.3.2 Seawater intrusion response to seasonal river discharge variation

With the calibrated model, it was possible to investigate seawater intrusion behavior and its maximum length during spring and neap tides under different upstream forcing conditions. In this study, the maximum seawater intrusion length was established as a salinity concentration of 1.0 g/kg. The model was forced with different discharges at Cubatão River upstream boundary to represent its seasonal variation. The normal discharge was imposed as a constant value of 16m³/s and it was used as the reference scenario; the low discharge was set as 8m³/s to present the dry season; and the high discharge was set as 40m³/s to represent the wet season.

For all simulated scenarios, the Cubatão River discharge was imposed as a constant discharge during the whole simulated period. As the study refers to the influence of Cubatão River on seawater intrusion behavior, HB, Mogi River and Perequê River discharges were kept unaltered in all scenarios, with the following values: 6.0m³/s, 6.0m³/s and 4.0m³/s, respectively. Figure 51 illustrates the salinity profile of the maximum seawater intrusion for each simulated scenario during spring and neap tide. The initial distance (00km) is the confluence of Cubatão and Mogi rivers.

Figure 51 – Salinity distribution in Cubatão River during spring tide (ST) and neap tide (NT) for different river discharge scenarios.

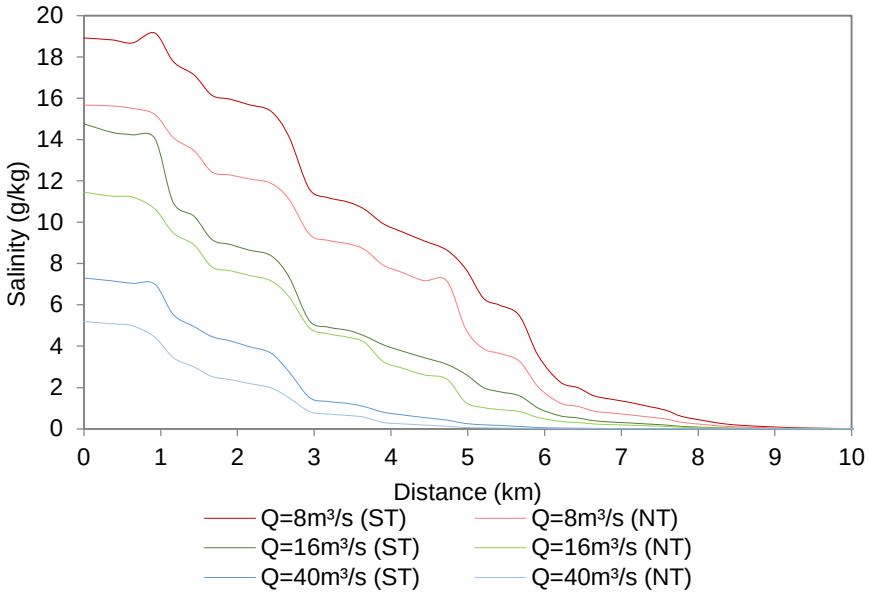

The seawater intrusion dynamics have shown significant variations in Cubatão River considering spring and neap tides and different river discharges. All seawater intrusion lengths were considered form the confluence of Cubatão and Mogi rivers. For the reference scenario (16m³/s), seawater intrusion presented similar behavior during spring and neap tide, only with a significant difference in the first three kilometers, in which spring tide provoked a stronger intrusion, because the tidal amplitude and the volume of seawater entering the estuarine system are higher. During neap tide, the maximum seawater intrusion is 5.2km and during spring tide it is 5.9km upstream Cubatão River.

Figure 52 illustrates the maximum seawater intrusion length in both spring and neap tide in Cubatão River obtained by the model. In terms of estuarine classification, the dark blue segment can be characterized as fluvial-tidal transition zone, which is affected by tides, but salinity concentration varies from 0.1g/kg to 1.0g/kg. The segments from light blue to red indicate the tidal zone or mixing zone of Cubatão River, in which salinity concentration is higher than 1.0g/kg. So, Cubatão River may be classified in the fluvial-transition zone or in the mixing zone of Santos estuarine system, depending on the forcing mechanisms at the moment.

Figure 52 – Maximum seawater intrusion during (a) spring and (b) neap tides (Q=16m³/s).

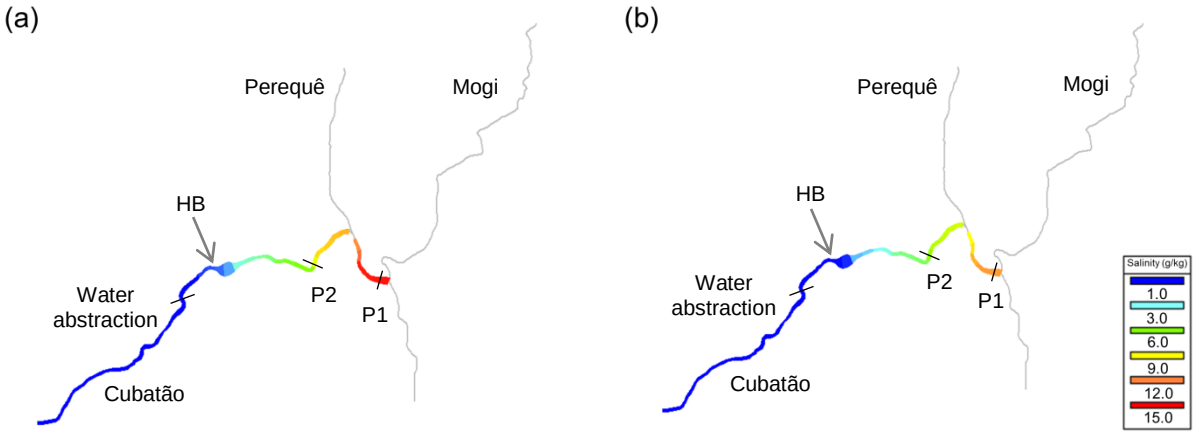

Regarding water abstraction for urban consumption, if we consider the seawater intrusion length limit of 1.0g/kg, it did not reach the water abstraction location, but for water quality purposes, it is recommended a salinity concentration bellow 0.5g/kg (EPA, 2018). In that case, salinity concentration during spring tide may impact the water abstraction and increase water treatment requirements, which is a worrying phenomenon for water management, because the simulated scenario is not reproducing an extreme event, but a typical one. A simple flood tide during spring tide combined with a common river discharge may impact water quality at the abstraction location, making it dependent on HB discharge or rainfall to increase river discharge and push seawater intrusion downstream.

For the simulated scenario considering the wet period (40m³/s), seawater intrusion is strongly reduced, with its maximum length of 3.7km during spring tide and only 2.8km during neap tide. In this scenario, seawater intrusion is not a concern for water abstraction purposes, as it presents almost null salinity values at the abstraction point. During wet period, Cubatão River is predominately classified in the fluvial-tidal transition estuarine zone, with river discharge as the governing mechanism. This classification is supported by the observed data from field surveys, in which high discharges flush the salinity out Cubatão River, making freshwater predominant during flood events (Figure 53).

Figure 53 – Maximum seawater intrusion during (a) spring and (b) neap tides (Q=40m³/s).

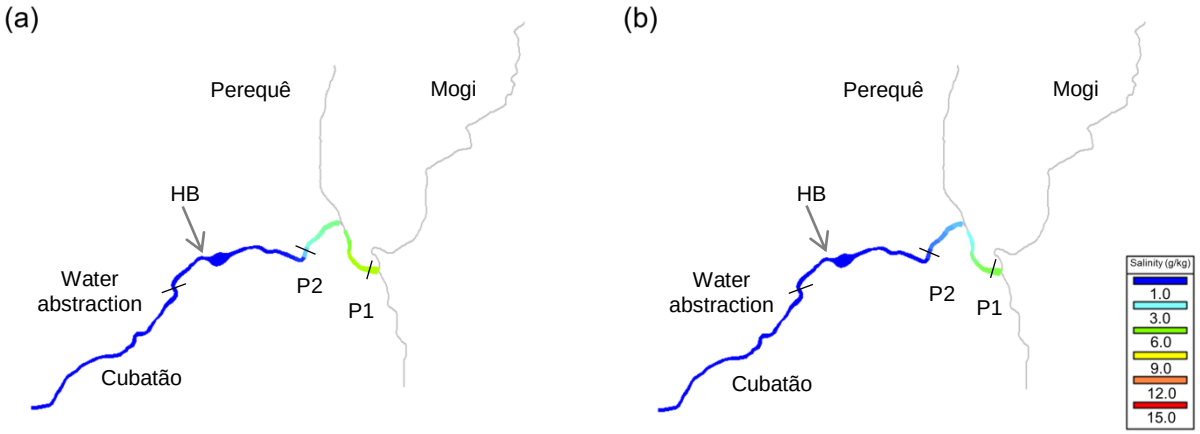

Finally, for the simulated scenario considering the dry period (8m³/s), it presented the most unfavorable seawater intrusion length, with a maximum seawater intrusion length of 7.4km during spring tide and 6.5km during neap tide. For both scenarios seawater intrusion may threaten water quality for urban consumption, because salinity concentration exceeds 1.0g/kg at the abstraction point in Cubatão River. Differently from the reference and wet scenarios, during dry season the urban reach of Cubatão River is predominantly classified in the mixing zone of the estuary, in which salinity values are higher than 1.0g/kg (Figure 54).

The dry season scenario is the most complex in terms of water management, because it may lead to water abstraction restriction during certain periods, principally during flood current on spring tides. The presence of salt in natural water for urban consumption may affect its quality and impact treatment plant components, pipelines and impair water and sanitation facilities. Management solutions could comprise HB discharges at during strong seawater intrusion. Table 14 summarizes the maximum seawater intrusion length for each simulated scenario considering the 1D model limitation of vertical homogeneity, which means a well-mixed estuary condition.

Figure 54 – Maximum seawater intrusion during (a) spring and (b) neap tides (Q=8m³/s).

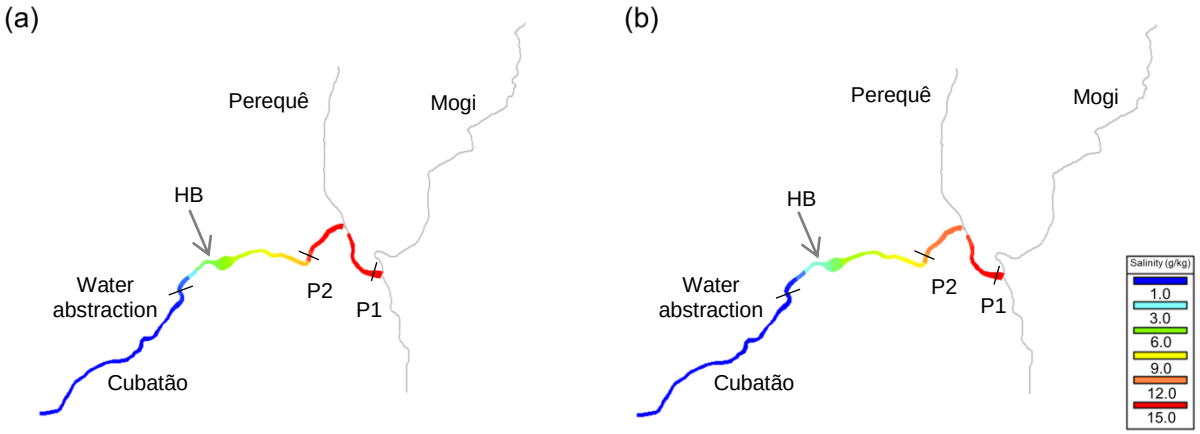

Table 14 – Maximum seawater intrusion length for each simulated scenario.

Flow condition	Seawater intrusion length (km)	
	Spring tide	Neap tide
Dry season (8m³/s)	7.4	6.5
Reference scenario (16m³/s)	5.9	5.2
Wet season (40m³/s)	3.7	2.8

5.3.3 Seawater intrusion response to sea level rise

The numerical results revel that typical dry seasons combined with higher sea surface height caused by SLR leads to grave concerns on seawater intrusion at the upstream parts of the Santos estuarine system, mainly at strategic locations with water abstraction for urban purposes. As Cubatão River is located is an estuarine system and seawater intrusion reaches its urban reach, SLR may enhance this phenomenon and affect local water abstraction which may lead to severe economic and social impacts in the future.

In this study, the results showed that the seawater intrusion increases significantly as a consequence of SLR in São Paulo coastal region. In the reference scenario (Cubatão River discharge = 10m³/s and HB discharge = 6m³/s), the maximum seawater intrusion length is 5.9 km, but under SLR conditions the seawater intrusion goes further the Cubatão River, reaching the farther water abstraction location with higher values of salinity concentration.

For the reference discharge, the maximum seawater intrusion profile for a SLR of 0.25m presented similar behavior to the ΔH=0.0m, but both SLR of 0.50m and 1.0m caused prominent changes in seawater intrusion profile. Due to 0.5m SLR the salinity concentration at the downstream end of Cubatão River was 21.0g/kg and the seawater intrusion length moved 600m upstream, from 7.4km to 8.0km. For the 1.0m SLR, the maximum salinity at the end of the river would reach almost 27.0g/kg, a very saline environment and the seawater intrusion length would increase 2.6km, from 7.4km to 10.0km

In Cubatão River, seawater intrusion length increased significantly in SLR scenarios. For the reference discharge (16m³/s), the maximum seawater intrusion profile for a SLR of 0.25m presented similar behavior to the reference scenario, but both SLR of 0.50m and 1.0m caused prominent changes in seawater intrusion profile. For example, due to 0.5m SLR the salinity concentration at the end of Cubatão River was 21.0g/kg the seawater intrusion length moved 600m upstream, from 7.4km to 8.0km. For the 1.0m SLR, the maximum salinity at the end of the river would reach almost 30.0g/kg, a very saline environment, and the seawater intrusion length increased 2.6km, from 7.4km to 10.0km (Figure 55). The initial distance (00km) is the confluence of Cubatão and Mogi rivers.

Figure 55 – Maximum seawater intrusion profile for each SLR scenario (16m³/s).

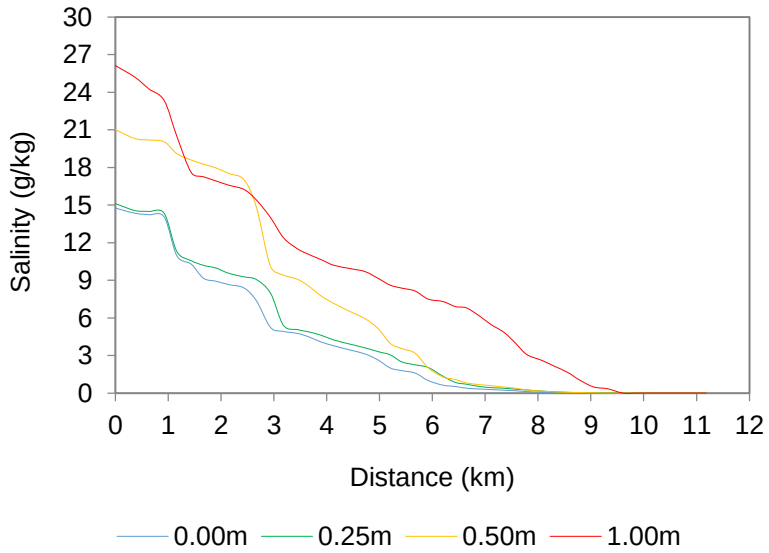

The water abstraction location is 6.5km upstream the end of Cubatão River, which would be strongly affected by a 1m SLR scenario, considering the current

mean river discharge. During the maximum seawater intrusion length in spring tides the salinity concentration would reach almost 7.0g/kg. This high salinity value strongly impacts water treatment for urban distribution, requiring specific treatment processes, otherwise it would harm the treatment plant facilities or the water distribution pipelines.

For the dry scenario (8m³/s) (Figure 56), the maximum seawater intrusion profile without considering SLR is already significant. While in the reference scenario the maximum seawater intrusion length is 5.9km, in the dry scenario it increases 1.5km, reaching 7.4km, beyond the water abstraction location. In Cubatão River, seawater intrusion in very sensitive to freshwater discharge variation, which indicates that, differently from the Santos estuary itself, this estuarine river dynamics depends on meteorological forcing conditions for efficient water management decision making processes.

Considering a SLR of 0.25m, the maximum sweater intrusion profile presented similar behavior to the ΔH=0.0m scenario, with a slight increase in salinity concentration at the end of the river. However, SLR of 0.5m and 1.0m would impact substantially seawater intrusion patterns in Cubatão River. Due to 0.5m SLR the salinity concentration at the end of Cubatão River would be 26.0g/kg and the seawater intrusion length would reach 7.9km and, at the water abstraction location, the salinity concentration reaches almost 5.0g/kg.

For the 1.0m SLR, the worst scenario, the maximum salinity at the end of the river reached more than 29.0g/kg and the seawater intrusion length increased to 10km, which means that almost the whole urban reach of Cubatão River would be with salinity higher than 1.0g/kg. During the maximum seawater intrusion length, the salinity concentration at the water abstraction would reach 12.0g/kg, a value that makes conventional water treatment unfeasible for urban consumption (Figure 56). The initial distance (00km) is the confluence of Cubatão and Mogi rivers.

Figure 56 – Maximum seawater intrusion profile for each SLR scenario (8m³/s).

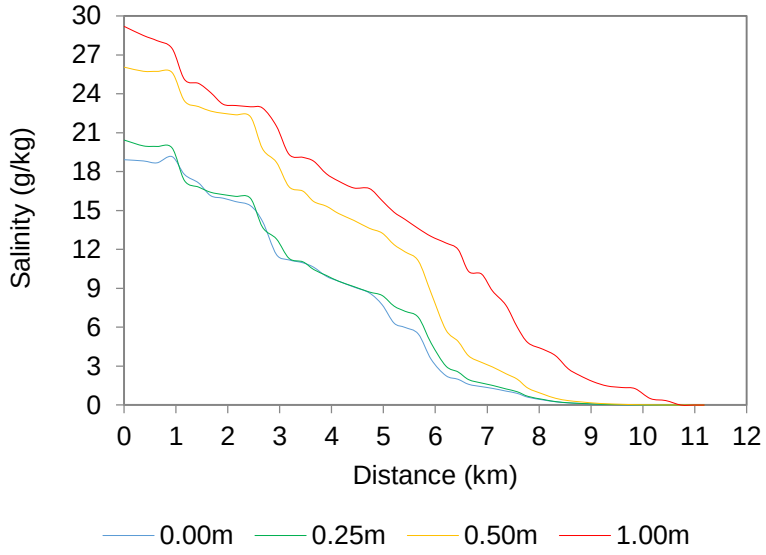

It was also investigated SLR impacts on seawater intrusion for higher river discharges: 20m³/s, 40m³/s, 60m³/s, 80m³/s and 100m³/s. In such way it was possible to estimate the maximum seawater intrusion versus the river discharge for each SLR scenario (Figure 57). The initial distance (00km) is the confluence of Cubatão and Mogi rivers.

Figure 57 – Variation of the seawater intrusion length versus fresh water discharge under SLR scenarios (ΔH=0.00m, 0.25m, 0.50m and 1.00m).

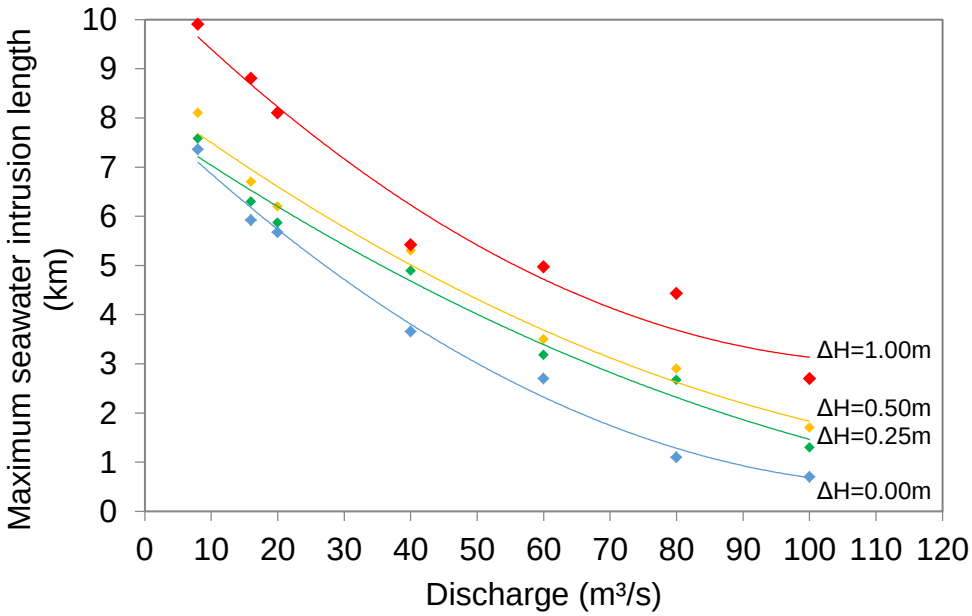

From the investigated scenarios, there are some relevant findings. With the increasing SLR, it would be necessary higher river discharge to maintain the

maximum seawater intrusion length compared to the ΔH=0.0m scenario, in which the maximum seawater intrusion length for a 40m³/s discharge is approximately 3.8km; in the 1.0m SLR scenario, the required discharge to maintain this seawater intrusion is 77.0m³/s.

Increased freshwater discharge pushes the limits of salt intrusion toward the river mouth. On the other hand, when the river discharge is decreased because of hydrological patterns, e.g. dry periods, the salinity intrusion length increases.

A serious outcome of more freshwater required to keep seawater intrusion length in acceptable values under SLR scenarios is that, in future scenarios of climate changes, there will be a considerable variation of precipitation patterns and, consequently, river flows may present unexpected behavior. In Cubatão, in which the city and industries concur for water abstraction from Cubatão River, this water abstraction restriction may pose a major water management concern.

Similarly, the increasing SLR would increase the discharge requirements to keep low salinity values at the water abstraction location in Cubatão River. For the reference scenario, the minimum discharge to keep salinity concentration bellow 0.5g/kg is 18m³/s; it increases to 20m³/s for a 0.25m SLR; to 30m³/s for a 0.50m SLR; and to 40m³/s for 1.0m SLR. Thus, a 1.0m SLR scenario would increase the discharge requirements in more than 2 times (Figure 58). It is important to observe that the minimum freshwater discharge to maintain salinity at low concentration at the water abstraction location refers to the mean sea level scenarios, considering only the astronomical tide; and tidal extreme weather effects are not considered.

Figure 58 – Minimum freshwater discharge to maintain S>0.5g/kg at the water abstraction location.

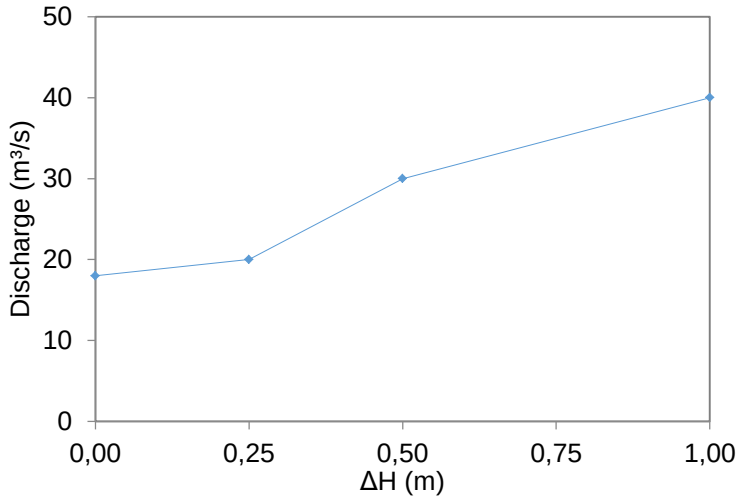

Stronger discharges are required to maintain seawater intrusion length at the water abstraction location. SLR increases the longitudinal salinity gradient, which causes higher seawater intrusion in the estuarine system. The increase in Cubatão River discharge required to keep salinity concentration values lower than 0.5g/kg at the abstraction location due to 0.25m, 0.5m and 1.0m SLR is $2m^3/s$, $12m^3/s$ and $22m^3/s$, respectively.

It is important to notice that all simulated scenarios consider that the Petrobras dam, located upstream the monitoring points, P1 and P2 (Figure 20), is not operating, which means that the seawater intrusion may reach further points, such as the water abstraction point. However, when the dam is operating, it works as a barrier for seawater intrusion and salinity concentration remains at negligible values at the water abstraction points in Cubatão River (FCTH, 2017).

In a future climate change scenarios, in which river discharge patterns may be strongly affected, water management at Cubatão River may require different strategies and actions to minimize the effects of sweater intrusion enhanced by SLR. Those strategies can be (1) the water abstraction during high discharge events, when the salinity concentration at the water abstraction location is reduced; (2) the higher freshwater reservation for eventual dry periods when the abstraction can be impracticable due to high salinity; (3) the selection of future water abstraction locations where the salinity intrusion is negligible even during low freshwater discharges; (4) higher HB discharges in Cubatão River, which can provoke water resources management conflicts, because the hydroelectric power plant and the water treatment facilities are operated by different companies.

6 CONCLUSIONS

This study was proposed to apply modeling tools to evaluate the salinity behavior of an estuarine river reach under different forcing conditions as hydrological, climate and anthropogenic changes. For this purpose monitoring and modeling techniques were applied to allow field data acquisition and processing.

To enlarge the observed salinity data, a low-cost Arduino-based EC sensor was developed for environmental applications which works fully submerged, with a power capacity of approximately eleven days in an acquisition frequency of one data per minute. Calibration was made up to 25g/kg salinity concentration, but considering the frequency upper limit of the LMC555 circuit, it can also be applied in higher salinity water bodies.

Based on validation tests, the sensor presented satisfactory correlation with a reference industrial salinity sensor. Its test in an estuarine river environment, with a salinity concentration range from almost 0g/kg (freshwater) to more than 15g/kg, showed that the sensor is adequate for water quality monitoring applications in shallow estuarine systems.

The sensor presented some benefits such as the final cost, making its assembling feasible to researches with a low budget; the electronic components are accessible, being unnecessary to depend on patented and costly devices; the housing and sealing were resistant and efficient, as the sensor worked the whole six days totally dry inside and without measurement interruption.

Despite its inadequate initial temperature reading, the sensor presented a 1.445g/kg RMSE, a 0.9392 R^2 and a 0.9383 EF values using its own temperature measurements and a 1.438g/kg RMSE, a 0.9412 R^2 and a 0.9851 EF values when using the reference temperature, which indicates an adequate performance for a low-cost sensor, as accurate as industrial ones. Improving its temperature measurements it would upgrade its salinity measurements.

Salinity stratification investigation provided a framework for characterizing and understanding spatial patterns in estuaries and their variability over time. Field surveys provided a singular observation of the hydroelectric power plant discharge and flood events effects on saline stratification in an estuarine river and the results are valuable for further water uses in Cubatão River particularly.

Salt wedge type is the most common stratification pattern in the monitoring points in Cubatão River. However, it presented all types of stratification patterns during the monitoring period. This complex behavior can be studied in future water quality modeling researches, in order to provide information for different water management scenarios.

The most important finding of this monitoring period is that the salinity stratification pattern in Cubatão River varies considerably under different forcing events and freshwater flow is the primary environmental factor controlling the stratification pattern in Cubatão River, but it is also strongly affected by hydroelectric power plant discharge and rainfall events.

The first finding related to the seawater intrusion modeling refers to the applied method, in which the estuary was simplified to an idealized one. A 30km idealized reach with an artificial $n=0.06 s/m^{1/3}$ worked adequately and the calibration and validation procedures delivered excellent results. It showed that this adaptation may be tested on different studies in which there is a lack of observed water quality or bathymetric data.

It is important to highlight that, as observed in the field surveys, the seawater intrusion in Cubatão River presents salt wedge stratification type during major time. However, as long as the HEC-RAS is a 1D model, there is no vertical salinity gradient, which means that the model always considers the estuary in well-mixed conditions. This limitation may cause significant differences between the real and the simulated seawater intrusion lengths.

Additionally, the idealized estuarine reach changed the geometry of the estuary and may have suppressed the effects of other river at Santos estuarine system. As a complex estuary, there are many other rivers that were not represented in the model that may affect the tidal propagation.

Considering the model response to seasonal river discharge and tide variation, it presented a clear sensitivity to those changes and seawater intrusion profiles in accordance with the expected result, i.e. reduced seawater intrusion under high river discharge and increased seawater intrusion under low river discharge. In the dry scenario ($Q=8.0 m^3/s$), seawater intrusion threatens water abstraction for urban consumption, even during neap tides, which already imposes a management challenge when the Petrobras dam is not operating.

The model also presented a satisfactory response to SLR scenarios, in which seawater intrusion length increases with the increasing mean sea level. As many coastal regions, Cubatão River water management may face severe restrictions due to increased seawater intrusion length. In some scenarios, for example, seawater intrusion length may duplicate for the same river discharge as a response to SLR. In the 1.0m SLR scenario, the fresh water discharge requirement to maintain the current salinity concentration at the water abstraction point may more than duplicate.

In further studies, it may be suggested to validate and apply the monitoring method in different estuarine systems. The application of low-cost salinity sensors may allow covering a wider study area with higher spatial resolution. Additionally, it reduces the dependency on expensive salinity sensors. The sensor design, battery autonomy, data precision, EC measurement method and written code may also be improved, absolutely. A specific study on improving this prototype may consolidate its application in different areas.

Other studies may make progress on investigating seawater intrusion scenarios in a numerical model with higher spatial resolution (2D or 3D). It may find significant results on salt wedge dynamics in Cubatão River and establish more precisely the seawater intrusion length under different forcing conditions. Downstream boundary condition may be enhanced by considering the effects of meteorological tides (meteorological influences with longer periodicities) and the occurrence of coastal extreme events.

Expanded scenarios may be explored, such as the seawater intrusion and salinity stratification response under different HB operational scenarios, as it has a complex discharge water behavior in Cubatão River. It may also be relevant to investigate the seawater intrusion response considering operational scenarios of Petrobras dam and how it impacts the salinity behavior.

REFERENCES

ALFREDINI, P.; ARASAKI, E. **Engenharia Portuária**. 2nd. ed. São Paulo: Edgard Blucher, 2013.

ALFREDINI, P.; ARASAKI, E. Estimation and Impacts of Sea Level Rise in Santos Port and Adjacent Areas (Brazil). **TransNav, the International Journal on Marine Navigation and Safety of Sea Transportation**, v. 12, n. 4, p. 739–744, 2019.

ANDREI, A.; ROBERT, B.; ERIKA, B. Numerical Limitations of 1D Hydraulic Models Using MIKE11 or HEC-RAS software - Case study of Baraolt River, Romania. **IOP Conference Series: Materials Science and Engineering**, v. 245, n. 7, 2017.

BHUIYAN, M. J. A. N.; DUTTA, D. Assessing impacts of sea level rise on river salinity in the Gorai river network, Bangladesh. **Estuarine, Coastal and Shelf Science**, v. 96, n. 1, p. 219–227, 2012.

BODDULA, V.; RAMASWAMY, L.; MISHRA, D. CyanoSense: A Wireless Remote Sensor System Using Raspberry-Pi and Arduino with Application to Algal Bloom. **Proceedings - 2017 IEEE 6th International Conference on AI and Mobile Services, AIMS 2017**, p. 85–88, 2017.

BRASIL. **Porto de Santos - Torre Grande (Estado de São Paulo) - 2019**, 2019. . Disponível em: <https://www.marinha.mil.br/chm/sites/www.marinha.mil.br.chm/files/dados_de_mare/santos_torre_grande_2019.pdf>.

BRUNNER, G. W. **HEC-RAS River Analysis System User's Manual**. 2016.

BRUNNER, G. W. **HEC-RAS River Analysis System Hydraulic Reference Manual**.2016a.

CAMERON, W. M.; PRITCHARD, D. W. Estuaries. In: HILL, M. N. (Ed.). **The Sea**. 2 nd ed. New York: John Wiley and Sons, 1963. p. 306–324.

CARMINATI, M.; LUZZATTO-FEGIZ, P. Conduino: Affordable and high-resolution multichannel water conductivity sensor using micro USB connectors. **Sensors and Actuators, B: Chemical**, v. 251, p. 1034–1041, 2017. Disponível em: <http://dx.doi.org/10.1016/j.snb.2017.05.184>.

CHAPRA, S. **Surface Water-Quality Modeling**. 2nd. ed. [s.l.] McGraw-Hill, 1997.

CHEN, W.; CHEN, K.; KUANG, C.; ZHU, D. Z.; HE, L.; MAO, X.; LIANG, H.; SONG, H. Influence of sea level rise on saline water intrusion in the Yangtze River Estuary, China. **Applied Ocean Research**, v. 54, p. 12–25, 2016.

CHUA, V. P.; XU, M. Impacts of sea-level rise on estuarine circulation: An idealized estuary and San Francisco Bay. **Journal of Marine Systems**, v. 139, p. 58–67, 2014. Disponível em: <http://dx.doi.org/10.1016/j.jmarsys.2014.05.012>.

COUTO, J. M. **Industrialização, Meio Ambiente e Pobreza. O Caso do Município de Cubatão/SP**. Maringá: Editora da Universidade Estadual de Maringá, 2012.

DAGGUPATI, P.; PAI, N.; ALE, S.; ZECKOSKI, R. W.; JEONG, J.; PARAJULI, P. B.; SARASWAT, D.; YOUSSEF, M. A. A Recommended Calibration and Validation Strategy for Hydrologic and Water Quality Models. **Transactions of the American Society of Agricultural and Biological Engineers**, v. 58, n. 6, p. 1705–1719, 2015. Disponível em: <http://elibrary.asabe.org/abstract.asp?aid=46545&t=3&dabs=Y&redir=&redirType=> .

DIONNE, J. C. Towards a more adequate definition of the St. Lawrence estuary. **Zeitschrift für Geomorphologie**, v. 7, n. 1, p. 36–44, 1963.

EME SYSTEMS. **SMX: Electrical Interface for moisture sensors.** 2018. Disponível em: <http://www.emesystems.com/smx/documents/SMX_2018.pdf>.

EPA. **Salinity**. 2018. Disponível em: <https://www.epa.sa.gov.au/environmental_info/water_quality/threats/salinity>.

ESTEVES, L. S. **Managed Realignment: A Viable Long-Term Coastal Management Strategy?** New York: Springer, 2014.

ETEMAD-SHAHIDI, A.; ROHANI, M. S.; PARSA, J.; LEMCKERT, C. Effects of sea level rise on the salinity of Bahmanshir estuary. **International Journal of Environmental Science and Technology**, v. 12, n. 10, p. 3329–3340, 17 out. 2015. Disponível em: <http://link.springer.com/10.1007/s13762-015-0761-x>.

FAUSTINE, A.; MVUMA, A. N.; MONGI, H. J.; GABRIEL, M. C.; TENGE, A. J.; KUCEL, S. B. Wireless Sensor Networks for Water Quality Monitoring and Control within Lake Victoria Basin: Prototype Development. **Wireless Sensor Network**, v. 06, n. 12, p. 281–290, 2014.

FCTH. **Controle de inundações das áreas urbanas e industriais situadas nas bacias dos Rios Cubatão , Perequê e Mogi**. 2017.

FERREIRA, D. M.; FERNANDES, C. V. S.; GOMES, J. Verification of Saint-Venant equations solution based on the lax diffusive method for flow routing in natural channels. **Brazilian Journal of Water Resources**, v. 22, n. 25, 2017.
GERTZ, E.; JUSTO, P. Di. **Environmental Monitoring with Arduino**. Sebastopol: O'Reilly, 2012.

GONÇALVES, G. R. Henry Borden: urbanização e industrialização. In: II Simpósio Internacional Eletrificação e Modernização Social, São Paulo. **Anais**... São Paulo: 2013.

GUTBERLET, J. **Cubatão. Desenvolvimento, Exclusão Social, Degradação Ambiental.** São Paulo: Edusp, 1996.
HADDOUT, S.; IGOUZAL, M.; MASLOUHI, A. Analytical and numerical study of the salinity intrusion in the Sebou river estuary (Morocco) - effect of the "Super Blood

Moon” (total lunar eclipse) of 2015. **Hydrology and Earth System Sciences**, v. 20, n. 9, p. 3923–3945, 26 set. 2016. Disponível em: <https://www.hydrol-earth-syst-sci.net/20/3923/2016/>.

HADDOUT, S.; IGOUZAL, M.; MASLOUHI, A. Modeling the effect of salt water intrusion in the Sebou River estuary (Morocco). **Russian Meteorology and Hydrology**, v. 42, n. 12, p. 803–811, 25 dez. 2017. Disponível em: <http://link.springer.com/10.3103/S1068373917120081>.

HANKS, S. **One dimensional hydraulic analysis of the effect of sea level rise on estuarine salinity**. 2011.

HARALAMBIDOU, K.; SYLAIOS, G.; TSIHRINTZIS, V. A. Salt-wedge propagation in a Mediterranean micro-tidal river mouth. **Estuarine, Coastal and Shelf Science**, v. 90, n. 4, p. 174–184, 2010. Disponível em: <http://dx.doi.org/10.1016/j.ecss.2010.08.010>.

HARARI, J.; CAMARGO, R. Tides and mean sea level variabilities in Santos (SP), 1944 to 1989. **Relatório Interno do Instituto Oceanográfico**, v. 36, n. February, p. 1–15, 1995.

HAYASHI, M. Temperature-electrical conductivity relation of water environmental monitoring and geophysical data inversion. **Environmental Monitoring and Assessment**, v. 96, p. 119–128, 2014. Disponível em: <https://doi.org/10.1016/j.physleta.2017.10.039%0Ahttp://dx.doi.org/10.1016/j.epsl.2015.04.028%0Ahttp://dx.doi.org/10.1016/j.desal.2012.06.001%0Ahttps://www.omicsonline.com/open-access/temperature-effects-on-conductivity-of-seawater-and-physiologic-salinem>.

HORSBURGH, J. S.; CARABALLO, J.; RAMÍREZ, M.; AUFDENKAMPE, A. K.; ARSCOTT, D. B.; DAMIANO, S. G. Low-Cost, Open-Source, and Low-Power: But What to Do With the Data? **Frontiers in Earth Science**, v. 7, n. April, p. 1–14, 2019. Disponível em: <https://www.frontiersin.org/article/10.3389/feart.2019.00067/full>.

IBGE. **Cubatão**. 2017. Disponível em: <https://cidades.ibge.gov.br/brasil/sp/cubatao/panorama>.

IOC; SCOR; IAPSO. The international thermodynamic equation of seawater – 2010: Calculation and use of thermodynamic properties. **Intergovernmental Oceanographic Commission, Manuals and Guides No. 56**, n. June, p. 196, 2010.
IPCC. **Climate change 2014. Synthesis report. Contribution of Working Groups I, II and III to the Fifth Assessment Report of the Intergovernmental Panel on Climate Change**. Geneva: IPCC, 2014.

JAMES, A. **An Introduction to Water Quality Modelling**. 2nd. ed. Chichester, West Sussex, England: John Wiley and Sons, 1993.

JEONG, S.; YEON, K.; HUR, Y.; OH, K. Salinity intrusion characteristics analysis using EFDC model in the downstream of Geum River. **Journal of Environmental Sciences**, v. 22, n. 6, p. 934–939, 2010. Disponível em:

<http://dx.doi.org/10.1016/S1001-0742(09)60201-1>.

JEPPESEN, E.; BRUCET, S.; NASELLI-FLORES, L.; PAPASTERGIADOU, E.; STEFANIDIS, K.; NÕGES, T.; NÕGES, P.; ATTAYDE, J. L.; ZOHARY, T.; COPPENS, J.; BUCAK, T.; MENEZES, R. F.; FREITAS, F. R. S.; KERNAN, M.; SØNDERGAARD, M.; BEKLIOĞLU, M. Ecological impacts of global warming and water abstraction on lakes and reservoirs due to changes in water level and related changes in salinity. **Hydrobiologia**, v. 750, n. 1, p. 201–227, 2015.

JI, Z.-G. **Hydrodynamics and Water Quality. Modeling Rivers, Lakes and Estuaries**. 2nd. ed. [s.l.] John Wiley and Sons, 2017.

JUGHES, J. M. **Arduino : A Technical Reference**. Sebastopol: O'Reilly, 2016.

JURANDIR, D. **Chove nos Campos de Cachoeira**. 8. ed. Belém: Pará.grafo Editora, 1941.

KIRK COCHRAN, J. Estuaries. In: **Reference Module in Earth Systems and Environmental Sciences**. New York: Elsevier Inc., 2014. p. 1–4.

KUANG, C.; CHEN, W.; GU, J.; SU, T. C.; SONG, H.; MA, Y.; DONG, Z. River discharge contribution to sea-level rise in the Yangtze River Estuary, China. **Continental Shelf Research**, v. 134, n. December 2016, p. 63–75, 2017. Disponível em: <http://dx.doi.org/10.1016/j.csr.2017.01.004>.

LAMBROU, T. P.; ANASTASIOU, C. C.; PANAYIOTOU, C. G.; POLYCARPOU, M. M. A Low-Cost Sensor Network for Real-Time Monitoring and Contamination Detection in Drinking Water Distribution Systems. **IEEE Sensors Journal**, v. 14, n. 8, p. 2765–2772, 2014.

LEONARD, B. P. The ULTIMATE conservative difference scheme applied to unsteady one-dimensional advection. **Computer Methods in Applied Mechanics and Engineering**, v. 88, n. 1, p. 17–74, 1991.

LEWIS, E. L.; PERKIN, R. G. The practical salinity scale 1978: conversion of existing data. **Deep Sea Research Part A. Oceanographic Research Papers**, v. 28, n. 4, p. 307–328, abr. 1981. Disponível em: <http://linkinghub.elsevier.com/retrieve/pii/0198014981900029>.

LI, D.; LIU, S. **Water Quality Monitoring and Management: Basis, Technology and Case Studies**. London: Elservier, 2019.

LIU, B.; PENG, S.; LIAO, Y.; WANG, H. The characteristics and causes of increasingly severe saltwater intrusion in Pearl River Estuary. **Estuarine, Coastal and Shelf Science**, v. 220, p. 54–63, 2019. Disponível em: <https://doi.org/10.1016/j.ecss.2019.02.041>.

LIU, W. C.; LIU, H. M. Assessing the impacts of sea level rise on salinity intrusion and transport time scales in a Tidal Estuary, Taiwan. **Water (Switzerland)**, v. 6, n. 2, p. 324–344, 2014.

LOCKRIDGE, G.; DZWONKOWSKI, B.; NELSON, R.; POWERS, S. Development of a low-cost arduino-based sonde for coastal applications. **Sensors (Switzerland)**, v. 16, n. 4, p. 1–16, 2016.

MALONE, R. W.; DAGGUPATI, P.; GUZMAN, J. A.; SARASWAT, D.; YUAN, Y.; WILSON, B. W.; SHIRMOHAMMADI, A.; DOUGLAS-MANKIN, K. R. Hydrologic and Water Quality Models: Key Calibration and Validation Topics. **Transactions of the American Society of Agricultural and Biological Engineers**, v. 58, n. 6, p. 1609–1618, 2015. Disponível em: <http://elibrary.asabe.org/abstract.asp?aid=46553&t=3&dabs=Y&redir=&redirType=>

MARGOLIS, M. **Arduino Cookbook**. Sebastopol: O'Reilly, 2011.

MARTIN, J. L.; MCCUTCHEON, S. C. **Hydrodynamics and Transport for Water Quality Modeling**. [s.l.] Lewis Publishers, 1999.

MATTE, P.; SECRETAN, Y.; MORIN, J. Hydrodynamic Modeling of the St. Lawrence Fluvial Estuary. I: Model Setup, Calibration and Validation. **Journal of Waterway, Port, Coastal, and Ocean Engineering**, v. 143, n. 5, p. 1–15, 2017. Disponível em: <https://ascelibrary.org/doi/pdf/10.1061/%28ASCE%29WW.1943-5460.0000397>.

MCDOUGALL, T. J.; FEISTEL, R.; PAWLOWICZ, R. Thermodynamics of seawater. In: SIEDLER, G.; GRIFFIES, S. M.; GOULD, J.; CHURCH, J. A. (Ed.). **Ocean Circulation and Climate**. 2. ed. OXford: Elsevier Ltd., 2013. p. 141–158.

MIRANDA, L. B. de; ANDUTTA, F. P.; KJERFVE, B.; CASTRO, B. M. de. **Fundamentals of Estuarine Physical Oceanography**. [s.l.] Springer, 2017.

MIRANDA, L. B. de; CASTRO, B. M. de; KJERFVE, B. **Princípios de Oceanografia Física de Estuários**. 2nd. ed. São Paulo: Edusp, 2012.

NASA. First Map Of Thawed Areas Under Greenland Ice Sheet. 7 ago. 2017. Disponível em: <https://www.nasa.gov/feature/goddard/2016/nasa-first-map-of-thawed-areas-under-greenland-ice-sheet>.

NELSON, J. **Introduction to Oceanography: Coastal Waters**. 2008. Disponível em: <http://www.iupui.edu/~g115/mod14/lecture03.html>.

NETO, J. C. de M. **Morte e Vida Severina e Outros Poemas para Vozes**. 4th. ed. Rio de Janeiro: Editora Nova Fronteira S.A., 1953.

NEUKOM, R.; STEIGER, N.; GÓMEZ-NAVARRO, J. J.; WANG, J.; WERNER, J. P. No evidence for globally coherent warm and cold periods over the preindustrial Common Era. **Nature**, v. 571, n. 7766, p. 550–554, 2019. Disponível em: <http://www.nature.com/articles/s41586-019-1401-2>.

NICHOLLS, R. J.; HANSON, S.; HERWEIJER, C.; PATMORE, N.; HALLEGATTE, S.; CORFEE-MORLOT, J.; CHÂTEAU, J.; MUIR-WOOD, R. **Ranking Port Cities with High Exposure and Vulnerability to Climate Extremes: Exposure**

Estimates. [s.l: s.n.].

ONSET. **HOBO ® U24-002-C Data Logger.** United States, 2019. Disponível em: <https://www.onsetcomp.com/products/data-loggers/u24-002-c>.

PALMER, K.; WATSON, C.; FISCHER, A. Non-linear interactions between sea-level rise, tides, and geomorphic change in the Tamar estuary, Australia. **Estuarine, Coastal and Shelf Science**, v. 225, n. June, p. 106247, 2019. Disponível em: <https://linkinghub.elsevier.com/retrieve/pii/S0272771419300149>.

PAWLOWICZ, R. Calculating the conductivity of natural waters. **Limnology and Oceanography: Methods**, v. 6, p. 489–501, 2008.

PERALES-VALDIVIA, H.; SANAY-GONZÁLEZ, R.; VALLE-LEVINSON, A. Effects of tides, wind and river discharge on the salt intrusion in a microtidal tropical estuary. **Regional Studies in Marine Science**, v. 24, p. 400–410, 2018. Disponível em: <https://doi.org/10.1016/j.rsma.2018.10.001>.

PINHO, J. L. S.; VIEIRA, J. M. P. Mathematical modelling of salt water intrusion in a northern Portuguese estuary. **IAHS-AISH Publication**, p. 1–14, 2007. Disponível em: <http://www.scopus.com/inward/record.url?eid=2-s2.0-33947172147&partnerID=MN8TOARS>.

PINTO, C. de S. **Cubatão. História de uma cidade industrial**. 2005.

PRANDLE, D. **Estuaries: Dynamics, Mixing, Sedimentation and Morphology**. New York: Cambridge University Press, 2009.

RAHMAN, A.; ZOBEYER, H. Modeling Salinity of the Passur River Using HEC-RAS. **International Conference on Recent Innovation in Civil Engineering for Sustainable Development (IICSD-2015)**, 2015.

RANJBAR, M. R.; ABDALLA, A. H. Low-cost, Real-Time, Autonomous Water Quality Testing and Notification System. **IJCSNS International Journal of Computer Science and Network Security**, v. 17, n. 5, p. 277–282, 2017. Disponível em: <http://paper.ijcsns.org/07_book/201705/20170537.pdf>.

RICH, V. I.; MAIER, R. M. Aquatic Environments. In: PEPPER, I. L.; GERBA, C. P.; GENTRY, T. J. (Ed.). **Environmental Microbiology**. 3rd. ed. London: Elsevier Inc., 2015. p. 111–138.

ROBINS, P. E.; SKOV, M. W.; LEWIS, M. J.; GIMÉNEZ, L.; DAVIES, A. G.; MALHAM, S. K.; NEILL, S. P.; MCDONALD, J. E.; WHITTON, T. A.; JACKSON, S. E.; JAGO, C. F. Impact of climate change on UK estuaries: A review of past trends and potential projections. **Estuarine, Coastal and Shelf Science**, v. 169, p. 119–135, 2016.

RODRÍGUEZ RODRIGUEZ, A.; VENTO ÁLVAREZ, J. R.; GARRIDO GONZÁLEZ, J.; RODRÍGUEZ BENITEZ, V. Monitoring tool for water quality and quick alert of flooding. **Sistemas y Telemática**, v. 16, n. 44, p. 25–34, 2018.

ROSA, J. G. A terceira margem do rio. In: **Primeiras Estórias**. 16th. ed. Rio de Janeiro: Editora Nova Fronteira Participações, 1962. p. 194.

ROVERSI, F. **Estudo Hidrodinâmico e de Renovação das Águas do Sistema Estuarino de Santos**. Dissertação (Mestrado em Engenharia Oceânica). UFRJ: Rio de Janeiro. 141p. 2012.

SAISP. **Sistema de Alerta a Inundações de São Paulo**São Paulo, 2019. . Disponível em: <https://www.saisp.br/estaticos/sitenovo/home.xmlt>.

SAVENIJE, H. H. G. **Salinity and Tide in alluvial estuaries**. 2nd. ed. Delft, The Netherlands: Delft University of Technology, 2012.

SIMAS, T.; NUNES, J. P.; FERREIRA, J. G. Effects of global climate change on coastal salt marshes. **Ecological Modelling**, v. 139, n. 1, p. 1–15, 2001.

SONDOTÉCNICA ENGENHARIA DE SOLOS S.A. 1977. **Comportamento hidráulico e sedimentológico do estuário santista (relatório final)**. M.T., Portobrás, I.N.P.H. 180p.

TALLEY, L. D.; PICKARD, G. L.; EMERY, W. J.; SWIFT, J. W. **Descriptive Physical Oceanography: An Introduction**. 6th. ed. San Diego: Elsevier, 2011.

TEXASINSTRUMENTS. **LMC555 CMOS Timer.** Dallas, 2019. . Disponível em: <http://www.ti.com/lit/ds/symlink/lmc555.pdf>.

TITUS, J. G.; PARK, R. A.; LEATHERMAN, S. P.; PARK, C.; MAUSEL, P. W. Greenhouse Effect and Sea Level Rise : The Cost of Holding Back the Sea. **Coastal Management**, v. 19, n. 2, p. 3–7, 2004.

UNESCO. **Guidelines on the study of seawater intrusion into rivers**. Paris: United Nations Educational, Scientific and Cultural Organization, 1991.

VARGAS, C. I. C.; VAZ, N.; DIAS, J. M. An evaluation of climate change effects in estuarine salinity patterns: Application to Ria de Aveiro shallow water system. **Estuarine, Coastal and Shelf Science**, v. 189, p. 33–45, 2017.

VISHAY. **IRF520, SiHF520**, 2011. Disponível em: <www.vishay.com/doc?91000>.

WANG, J.; LI, L.; HE, Z.; KALHORO, N. A.; XU, D. Numerical modelling study of seawater intrusion in Indus River Estuary, Pakistan. **Ocean Engineering**, v. 184, n. November 2018, p. 74–84, 2019. Disponível em: <https://linkinghub.elsevier.com/retrieve/pii/S0029801819302574>.

WOLANSKI, E.; DAY, J. W.; ELLIOTT, M.; RAMACHANDRAN, R. **Coasts and Estuaries: The Future**. Orxford: Elsevier, 2019.

YANG, Z.; WANG, T.; VOISIN, N.; COPPING, A. Estuarine response to river flow and sea-level rise under future climate change and human development. **Estuarine,**

Coastal and Shelf Science, v. 156, n. 1, p. 19–30, 2015. Disponível em: <http://dx.doi.org/10.1016/j.ecss.2014.08.015>.

YOON, B. Il; WOO, S.-B. The Along-channel Salinity Distribution and its Response to River Discharge in Tidally-dominated Han River Estuary, South Korea. **Procedia Engineering**, v. 116, n. 1, p. 763–770, 2015. Disponível em: <http://dx.doi.org/10.1016/j.proeng.2015.08.362>.

ZHANG, Z.; JOHNSON, B. E. Application and Evaluation of the HEC-RAS-Nutrient Simulation Module (NSM I). **Ecosystem Management and Restoration Research Program**, n. June, p. 19, 2014.

ZHU, X.; LI, D.; HE, D.; WANG, J.; MA, D.; LI, F. A remote wireless system for water quality online monitoring in intensive fish culture. **Computers and Electronics in Agriculture**, v. 71, n. SUPPL. 1, p. S3, 2010.

APPENDIX A

```
#include <SPI.h>
#include <SdFat.h>
#include <DS3232RTC.h>
#include <OneWire.h>
#include <DallasTemperature.h>
#include <LowPower.h>
#define ONE_WIRE_BUS 4

SdFat SD;
const int cS=10;
String dataString = "";
String(arq) = "";
String(dh) = "";
const uint8_t alarmInput(3);
OneWire oneWire(ONE_WIRE_BUS);
DallasTemperature sensors(&oneWire);
DeviceAddress insideThermometer;
String(sensor_id);
uint32_t celcius;


void setup() {
Serial.begin(9600);


pinMode(3, INPUT_PULLUP);
pinMode(4, INPUT);
digitalWrite(4, LOW);
pinMode(5, OUTPUT);
digitalWrite(5,HIGH);
pinMode(6, INPUT);
digitalWrite(6, HIGH);
pinMode(7, OUTPUT);
digitalWrite(7, LOW);
pinMode(8, OUTPUT);
digitalWrite(8, HIGH);
pinMode(9, OUTPUT);
digitalWrite(9, HIGH);
delay(125);
pinMode(cS, OUTPUT);
digitalWrite(cS, HIGH);
pinMode(11, OUTPUT)
digitalWrite(11, HIGH);
pinMode(12, INPUT);
digitalWrite(12, HIGH);
pinMode(13, OUTPUT);
digitalWrite(13, LOW);
delay(125);
```

```
digitalWrite(5,LOW);


//*******RTC Alarm***********

RTC.setAlarm(ALM1_MATCH_DATE, 0, 0, 0, 1);
RTC.setAlarm(ALM2_MATCH_DATE, 0, 0, 0, 1);
RTC.alarm(ALARM_1);
RTC.alarm(ALARM_2);
RTC.alarmInterrupt(ALARM_1, false);
RTC.alarmInterrupt(ALARM_2, false);
RTC.squareWave(SQWAVE_NONE);

RTC.setAlarm(ALM1_MATCH_SECONDS, 30, 0, 0, 0);
RTC.setAlarm(ALM2_EVERY_MINUTE, 0, 0, 0, 0);
RTC.alarm(ALARM_2);
RTC.alarmInterrupt(ALARM_1, false);
RTC.alarmInterrupt(ALARM_2, true);
pinMode(2, INPUT_PULLUP);

//*****************************************

void loop() {
digitalWrite(10, HIGH);
digitalWrite(11, HIGH);
digitalWrite(12, HIGH);
digitalWrite(13, LOW);
digitalWrite(5, LOW);
delay(3);
attachInterrupt(1, wakeUp, LOW);
delay(15);
LowPower.powerDown(SLEEP_FOREVER, ADC_OFF, BOD_OFF);
delay(15);
detachInterrupt(1);
digitalWrite(5, HIGH);
delay(15);
SPI.begin();
sensors.begin();
sensors.getAddress(insideThermometer, 0);

sensors.setResolution(insideThermometer, 11);
arq = "";
if ( RTC.alarm(ALARM_2) ) {
setSyncProvider(RTC.get);
Data_Hora();
mede();
}
}

//***********************************************
```

```
void Data_Hora() {
dh = "";
zero_data(day());
zero_data(month());
zero_data(year()-2000);
zero_hora(day());
zero_hora(month());
zero_hora(year()-2000);
zero_hora(hour());
zero_hora(minute());
zero_hora(second());
}
void zero_data(unsigned int digits) {
if(digits < 10) {
arq += "0";
}
arq += String (digits);
}
void zero_hora(unsigned int digits) {
if(digits < 10) {
dh += "0";
}
dh += String (digits);
}

//*************************************************

void wakeUp() {

//****************read temperature*******************

void printTemperature(DeviceAddress deviceAddress) {
    float tempC = sensors.getTempC(deviceAddress);
    celcius = (word)(tempC * 1000);
}

//**************temperature sensor's ID*****************

void printAddress(DeviceAddress deviceAddress) {
sensor_id = "";
for (uint8_t i = 0; i < 8; i++)
{
if (deviceAddress[i] < 16) Serial.print("0");
sensor_id += String(deviceAddress[i], HEX);
}
}

//*************************************************

void grava_cartao() {
```

```
if (!SD.begin(cS,SPI_QUARTER_SPEED)) {

}
else {

}

arq += ".csv";

delay(3);
File dataFile = SD.open(arq, O_CREAT |  O_WRITE | O_APPEND);
if (dataFile) {
dataFile.println(dataString);
delay(3);
dataFile.close();
delay(3);
}

Serial.println(dataString);

delay(121);
}
//*************************************************

void mede() {
dataString = "";
sensors.requestTemperatures();
delay(15);
uint32_t ligado;
uint32_t deslig;
uint32_t ps= 0;

TCCR1A = 0; TCCR1B = 0;
TCCR2A = 0; TCCR2B = 0;
TCNT1 = 0;  TCNT2 = 0;
ligado = pulseIn(2,HIGH);
deslig = pulseIn(2,LOW);
ps = 500000/(ligado + deslig);

printTemperature(insideThermometer);
printAddress(insideThermometer);
delay(3);

//*******Battery voltage*********

uint16_t bat = 0;
uint8_t n = 4;
for ( uint8_t k = 0 ; k < n; k++ ){
delay(k + n);

bat = bat + analogRead(A1);
```

```
}
bat = ((bat*(5029*3.05))/(1023*n));
dataString = "," + String(dh) + "," + String(ps) + "," +
String(celcius) + "," + sensor_id + "," + String(bat) + ",";
grava_cartao}1
```